# Imprinting in P(VDF-TrFE) - Interplay between ferroelectric polarization and relaxational polarization

*Dissertation*
*zur Erlangung des Grades*
*des Doktors der Ingenieurwissenschaften*

*der Naturwissenschaftlich-Technischen Fakultät*
*der Universität des Saarlandes*

von
Christian PETER

Saarbrücken
2023

| | |
|---|---|
| **Tag des Kolloquiums:** | 8. November 2023 |
| **Dekan:** | Prof. Dr. Ludger Santen |
| **Berichterstatter:** | Prof. Dr.-Ing. Herbert Kliem<br>Prof. Dr. Walter Arnold |
| **Akad. Mitglied:** | Dr. Haibin Gao |
| **Vorsitz:** | Prof. Dr. Ralf Seemann |

# *Zusammenfassung*

Diese Arbeit beschäftigt sich mit imprinting im ferroelektrischen Polymer P(VDF-TrFE) 70/30 mol %. Experimentell untersucht werden Dünnschichtfilme (50 nm bis 2 µm) . Für Imprinteffekte (Zunahme des Koerzitivfeldes und der ferroelektrischen Umschaltzeit sowie Abnahme der remanenten Polarisation und der Permittivität) wird eine charakteristische Abhängigkeit($\sim \log(t_w)$) von der Verweildauer ($t_w$) in einem ferroelektrischen Polarisationszustand beobachtet. Es wird gezeigt, dass Imprinteffekte unabhängig von der Schichtdicke ($> 100$ nm) sind und imprint durch eine Erhöhung der Polymer-Kristallinität weitgehend verhindert werden kann. Ein Imprintmodell (New Imprint Model) wird entwickelt. Auf dessen Grundlage werden mit einem "Weiss-Mean-Field" Ansatz die Imprinteffekte berechnet. Es werden Temperatur-Polarisationshysteresen für gepolte und ungepolte Proben aufgenommen. Es wird gezeigt, dass der beim Aufheizen fließende Kurzschlussstrom aus Imprintstrom und pyroelektischem Strom zusammengesetzt ist. Eine Berechnung des Imprintstroms gelingt durch die Annahme einer Verteilung von temperaturabhängigen Dipolrelaxationszeiten. Im letzten Kapitel wird eine experimentelle Methode vorgestellt um simultan elektrische und IR spektroskopische Messungen in Dünnschichtfilmen durchzuführen.

# *Abstract*

This thesis deals with imprinting in ferroelectric P(VDF-TrFE)70/30 mol % thin films (50 nm to 2 µm). Material properties that change due to imprinting are explored: the ferroelectric polarization switching time and the coercive field increase, as well as the permittivity and the remanent polarization to decrease. These effects of imprinting evolve on a logarithmic time scale. It is shown that imprinting evolves independent of the film thickness. An increase in the polymers crystallinity decelerates imprinting. A model (New Imprint Model) is proposed to explain the effects of imprinting. By introducing an extended Weiss Mean Field approximation the effects of imprinting are calculated. The spontaneous or field induced build-up of the spontaneous or remanent ferroelectric polarization across the Curie transition range are monitored. The imprinting current while heating is separated from the pyroelectric current and calculated based on a distribution of temperature dependent dipole relaxation times. In the last chapter an experimental method is presented, which allows simultaneous in-situ infrared (IR) and electrical characterization.

# *Acknowledgements*

I want to thank my parents for everlasting love and support, my partner Alexandra Léon for making my life sweet and many others including family, friends and co-workers just for being there.
Special thanks go to my adviser Prof. Kliem. Also I want to thank Prof. Arnold for being the second examiner. I want to thank Andreas Leschhorn for being a fine coworker, a great source of knowledge and wit and for proof reading, Omar Elshedy for conducting some numerical calculations with the Weiss model, Prof. Guodong Zhu from the Department of Materials Science, Fudan University, Shanghai, for providing epitaxial samples and the XRD data. Prof. Jan K. Krüger for ideas and material support for conducting pyroelectric measurements. Last but not least, I want to thank Christophe Nies for good co-workership in all stages of infrared investigations and Prof. Wulff Possart for providing a measurement environment for IR spectroscopic studies, participating the discussions regarding the IR spectroscopic results and contributing to my approval as PhD candidate. I want to thank Prof. Rolf Pelster for the support along the the way to the PhD title.

# Contents

# List of Figures

# List of Tables

# List of Abbreviations

| | |
|---|---|
| **Al** | **A**luminum |
| **bc** | **b**ottom **c**onnection |
| **bg** | **b**ack **g**round (current) |
| **DFE** | **D**efect **F**erro**e**lectric (phase) |
| **DSC** | **D**ifferential **S**canning **C**alorimetry |
| **dw** | **d**ouble **w**ell (potential) |
| **fd** | **f**erroelectric **d**ipoles |
| **FE** | **F**erro**E**lectric (phase) |
| **rd** | **r**elaxational **d**ipoles |
| **PE** | **P**ara**E**lectric (phase) |
| **SAXS** | **S**mall **A**ngle **X**-rays **S**cattering |
| **tc** | **t**op **c**onnection |
| **WAXS** | **W**ide **A**ngle **X**-rays **S**cattering |

# Physical Constants

| | |
|---|---|
| Boltzmann constant | $k_B = 1.380\,645\,2 \times 10^{-23}\,\mathrm{A\,s\,V^{-1}\,m^{-1}}$ |
| | $= 8.617\,330\,3 \times 10^{-5}\,\mathrm{eV\,K^{-1}}$ |
| Permittivity of free space | $\varepsilon_0 = 8.854\,187\,817\,62 \times 10^{-12}\,\mathrm{A\,s\,V^{-1}\,m^{-1}}$ |

# List of Symbols

| | | |
|---|---|---|
| $\alpha_3$ | thermal expansion coefficient along the 3-axis | $\mathrm{K^{-1}}$ |
| $A$ | proportionality factor | $\mathrm{A\,s\,m^{-2}}$ |
| $A_{el}$ | electrode area | $\mathrm{m^2}$ |
| $a_i$ | material property at zero imprint | depends on i |
| $\beta$ | coupling constant | $\mathrm{V\,m\,A^{-1}\,s^{-1}}$ |
| $b_i$ | "speed" of which an imprint effects evolves | depends on i |
| $\delta$ | stretching factor | |
| $d$ | total polymer film thickness | m |
| $d_{dl}$ | thickness of the dead layer | m |
| $d_{bu}$ | thickness of the bulk layer | m |

| | | |
|---|---|---|
| $D$ | dielectric displacement | $\mathrm{A\,s\,m^{-2}}$ |
| $\varepsilon$ | permittivity | $\mathrm{A\,s\,V^{-1}\,m^{-1}}$ |
| $\varepsilon_0$ | vacuum permittivity | $\mathrm{A\,s\,V^{-1}\,m^{-1}}$ |
| $\varepsilon_{dl}$ | permittivity of the dead layer | $\mathrm{A\,s\,V^{-1}\,m^{-1}}$ |
| $\varepsilon_{bu}$ | permittivity of the bulk layer | $\mathrm{A\,s\,V^{-1}\,m^{-1}}$ |
| $\varepsilon_r$ | relative permittivity | $\mathrm{A\,s\,V^{-1}\,m^{-1}}$ |
| $E$ | electric field | $\mathrm{V\,m^{-1}}$ |
| $E_a$ | activation field in the Merz law | $\mathrm{V\,m^{-1}}$ |
| $E_c$ | electric coercive field | $\mathrm{V\,m^{-1}}$ |
| $E_c'$ | electric coercive field determined from the current | $\mathrm{V\,m^{-1}}$ |
| $E_{depol}$ | electric depolarization field | $\mathrm{V\,m^{-1}}$ |
| $E_{dl}$ | electric field in the dead layer | $\mathrm{V\,m^{-1}}$ |
| $E_{ext}$ | externally applied electric field | $\mathrm{V\,m^{-1}}$ |
| $E_{imprint}$ | imprint electric field | $\mathrm{V\,m^{-1}}$ |
| $f(\nu)$ | distribution density of $\nu$ | |
| $g(W)$ | distribution density of $W$ | |
| $I$ | current | A |
| $j$ | current density | $\mathrm{A\,m^{-2}}$ |
| $j_{depol}$ | depolarization current density | $\mathrm{A\,m^{-2}}$ |
| $j_{heating}$ | short circuit current density while heating | $\mathrm{A\,m^{-2}}$ |
| $j_{pyro}$ | pyroelectric current density | $\mathrm{A\,m^{-2}}$ |
| $j_{irrev}$ | irreversible part of $j_{heating}$ | $\mathrm{A\,m^{-2}}$ |
| $j_{rel}$ | imprinting current density | $\mathrm{A\,m^{-2}}$ |
| $m_{fe}$ | ferroelectric dipole moment | $\mathrm{A\,s\,m}$ |
| $n$ | dipole density | $\mathrm{m^{-3}}$ |
| $p_{pyro}$ | pyroelectric coefficient | $\mathrm{A\,s\,m^{-2}\,K^{-1}}$ |
| $p_{pyro,3}$ | pyroelectric coefficient along the 3-axis | $\mathrm{A\,s\,m^{-2}\,K^{-1}}$ |
| $p_{primPyro,3}$ | $p_{pyro,3}$ due to primary pyroelectricity | $\mathrm{A\,s\,m^{-2}\,K^{-1}}$ |
| $p_{secPyro,3}$ | $p_{pyro,3}$ due to secondary pyroelectricity | $\mathrm{A\,s\,m^{-2}\,K^{-1}}$ |
| $p_i$ | individual polarization processes | $\mathrm{A\,s\,m^{-2}}$ |
| $P$ | macroscopic polarization | $\mathrm{A\,s\,m^{-2}}$ |
| $P_{fe}$ | ferroelectric polarization | $\mathrm{A\,s\,m^{-2}}$ |
| $P_{rem}$ | remanent polarization | $\mathrm{A\,s\,m^{-2}}$ |
| $P_{rel}$ | relaxational polarization | $\mathrm{A\,s\,m^{-2}}$ |
| $P_{rel,eq}$ | equilibrium relaxational polarization | $\mathrm{A\,s\,m^{-2}}$ |
| $P_{sat}$ | ferroelectric saturation polarization | $\mathrm{A\,s\,m^{-2}}$ |
| $P_{switch}$ | switchable ferroelectric polarization | $\mathrm{A\,s\,m^{-2}}$ |
| $Q$ | charge | $\mathrm{A\,s}$ |
| $R$ | distance between double well minima | m |
| $\sigma$ | conductivity | $\mathrm{A\,V^{-1}\,m^{-1}}$ |
| $\theta$ | angle between ferroelectric dipoles and 3-axis | |
| $\tau$ | ferroelectric polarization switching time | s |
| $\tau_{0,Arrh}$ | time constant in the Arrhenius law | s |
| $\tau_{0,exp}$ | time constant in the Merz law | s |
| $\tau_{0,power}$ | time constant in the Merz law | s |
| $\tau_{0,VTF}$ | time constant in the Vogel-Tammann-Fulcher law | s |
| $\tau_c$ | time constant in the compensation law | s |
| $\tau_i$ | individual relaxation time of relaxational dipoles | s |
| $\tau_{rd}$ | relaxation time of relaxational dipoles | s |
| $t$ | time | s |
| $t_w$ | waiting time | s |

| | | |
|---|---|---|
| $T$ | temperature | K |
| $T_C$ | Curie Temperature | K |
| $T'_C$ | Curie Temperature in the compensation law | K |
| $T_m$ | melting temperature (of the co-polymer) | K |
| $T_{VTF}$ | Vogel-Tammann-Fulcher Temperature | K |
| $\nu$ | relaxation frequency | $s^{-1}$ |
| $v$ | velocity | $m\,s^{-1}$ |
| $V$ | sample volume | $m^3$ |
| $W$ | energy barrier | eV |
| $W_0$ | intrinsic energy barrier | eV |
| $W_i$ | individual energy barrier | eV |
| $W_{imprint}$ | imprint potential barrier | eV |
| $W_a$ | activation energy | eV |

*Science, no fake*

# सत्

# Chapter 1

# Introduction

## 1.1 Motivation

Many ferroelectric materials are affected by imprinting. Often it is referred to imprinting as a degradation mechanism which summarizes some time dependent effects related to ferroelectric polarization. Exemplary imprint effects are the slowing down of the ferroelectric polarization switching process and the decay of the remanent polarization. In the view of using ferroelectrics as functional materials e.g. in non-volatile ferroelectric memory devices, these effects mean a reduction of writing speed and shortening of data retention time. Besides, for many applications predictable material properties are required. Regarding P(VDF-TrFE), imprinting constitutes a major obstacle why this otherwise excellent material isn't used on a wider scale in industry.
The imprinting mechanism differs from one ferroelectric material to another. The first attempt to give an explanation for imprinting in P(VDF-TrFE) was presented by Ikeda et al. in 1988 [41]. Since then several other models have been proposed to understand the imprinting mechanism. Still, up to date (before the data presented in this work was published) no procedure nor treatment is known to manipulate imprinting and/or its effects.
The aim of this work is primarily to investigate effects of ferroelectric imprinting in P(VDF-TrFE) and understand its mechanism.

## 1.2 Overview and highlights

The thesis is structured as listed below. Major achievements of this work, described in the respective chapters, are stated.

- Chapter 2 provides some general definitions regarding ferroelectricity and pyroelectricity. Literature based information on P(VDF-TrFE) is presented, including its history, its application as functional material, its chemical composition, inherent crystalline phases, thermal and electric field induced phase transformations, its micro- and meso-scale structures and its ferroelectric and pyroelectric properties.
- Chapter 3 gives the theoretical basis regarding ferroelectric imprinting. Imprinting in various ferroelectrics is briefly reviewed. Imprint models for P(VDF-TrFE) are discussed. The New Imprint Model, which was designed in the course of this work is presented. The current response of a system of independently relaxing dipoles is discussed.

- Chapter 4 deals with the sample preparation procedure and the electric measurement setup. The presented P(VDF-TrFE) polymer film preparation method, allows to produce large area ($cm^2$ range) thin films by spin-coating. The films are characterized by low film-thickness variation, absence of pin-holes, high breakdown electric field strength, and a reduced "background" current in pyroelectric measurements.

- Chapter 5 deals with results regarding imprint effects. Material properties affected by imprint are explored. A common characteristic time-dependence of imprint effects is found. Existing models are reviewed in the light of some insightful experimental findings. The existence of an imprint field is postulated. The imprint field is introduced as local field contribution in an extended Weiss field approach and the effects of imprinting are calculated.
  The New Imprint Model is found suitable to interpret the presented experimental results. Noteworthy is the experimental observation that imprinting can be reduced by increasing the co-polymers crystallinity. The results of the calculation support the validity of the model.

- Chapter 6 is the second results chapter dealing with imprinting. Here, the focus is on the temperature dependence of imprinting. The results are always interpreted in the light of the New Imprint Model. Un-poled and poled samples are investigated. After taking measures to eliminate the background (bg) current, ferroelectric polarization versus temperature hysteresis are recorded for un-poled and poled samples. Additionally, the impact of using samples produced with different annealing temperatures, using different cooling rates and applying an electric field while cooling is investigated. The short circuit current across the Curie transition temperature range is investigated using poled samples. The imprinting related current and the pyroelectric current are identified and separated at temperatures below the onset temperature of the ferroelectric to paraelectric phase transition, thus at temperatures between $-20\,^{\circ}C$ to $80\,^{\circ}C$. The imprinting current while heating is calculated based on assumptions made in the New Imprint Model.
  Highlights in this chapter are the ferroelectric polarization versus temperature hysteresis loops using un-poled and poled samples, showing that the spontaneous ferroelectric polarization is very different from the remanent polarization. Another highlight is the observation that the imprint field affects the paraelectric to ferroelectric phase transition temperature. A particular highlight is the calculation of the imprinting current. The calculation assumes the Tammann-Vogel-Fulcher- (or the Arrhenius-) law and compensation law to describe the temperature dependence of imprinting in different temperature regimes. Finally, its hypothesized that imprinting related dipole reorientation processes aren't restricted to the amorphous phase but rather also take place in the crystalline-amorphous interphase, especially at high temperatures ($T \geq 50\,^{\circ}C$).

- Chapter 7 deals with a method for in-situ infrared (IR) investigation of thin polymer films. The developed method allows simultaneous IR investigation while electrical fields can be applied and polarization and current measurements can be conducted. Thus, the method allows simultaneous monitoring of poling processes by electrical and structure resolving means.

- Chapter 8: Summary and Outlook

# Chapter 2

# Theoretical basis I: Ferro- and Pyroelectricity in P(VDF-TrFE)

## 2.1 Ferroelectricity

Ferroelectricity was first discovered in Rochelle Salt in 1920 [115]. Ferroelectrics get their name by analogy with ferromagnetic materials, the prefix *ferro*, meaning iron. Like ferromagnetic materials, ferroelectric materials exhibit a hysteresis, as was first observed by C.B.Sawyer and C.H. Tower for Rochelle Salt in the polarization $P$ versus electric field $E$ dependence [99]. Later on several hundreds other ferroelectric materials were discovered and new ferroelectrics are often added to the list.

Out of 32 crystal point groups with dielectric properties, 20 are piezoelectric. 10 out of these 20 non-centrosymmetric point groups, belong to polar crystals, which are pyroelectric. Pyroelectric materials possess a temperature dependent spontaneous polarization. Those pyroelectrics in which the polarization can be switched back and forth by application of an external electric field are called ferroelectrics [16].

The ferroelectric polarization $\mathbf{P}_{fe}$ originates from the alignment of material inherent dipoles and can be written as the vector sum of dipole moments $\mathbf{m}$ per volume $V$:

$$\mathbf{P_{fe}} = \frac{\sum_i \mathbf{m_i}}{V} \tag{2.1}$$

The polarization is often only considered along one axis as it is appropriate, when the material is packed into a plate capacitor structure, then the vector has only one vector entry, the scalar $P_{fe}$. The measured polarization at zero applied field is the remanent polarization $P_{rem}$. The direction of the ferroelectric polarization vector can be reversed by application of an external electric field of sufficient field strength. The minimum electric field strength necessary to reverse the ferroelectric polarization is the coercive field $E_c$. Next to $P_{rem}$ and $E_c$ also $E_{sat}$ and $P_{sat}$ are the characteristic properties of the ferroelectric polarization ($P_{fe}$) hysteresis presented in FIG. 2.1 a). $E_{sat}$ and $P_{sat}$ are the minimum field strength and the corresponding polarization value, respectively, at which $P_{fe}$ can unambiguously be related to the applied electric field. Thus, above $E_{sat}$ the hysteresis behavior disappears. The experimentally accessible value is the dielectric displacement $D$ as the charge density in the electrode plates (see equation (2.2)), which includes other electric field induced polarization contributions.

$$D = P_{fe} + \varepsilon_0 \varepsilon_r E_{ext} \tag{2.2}$$

$\varepsilon_0$ and $\varepsilon_r$ in equation (2.2) are the permittivity of free space and the relative permittivity of the ferroelectric material, respectively. FIG. 2.1 a) depicts the ferroelectric

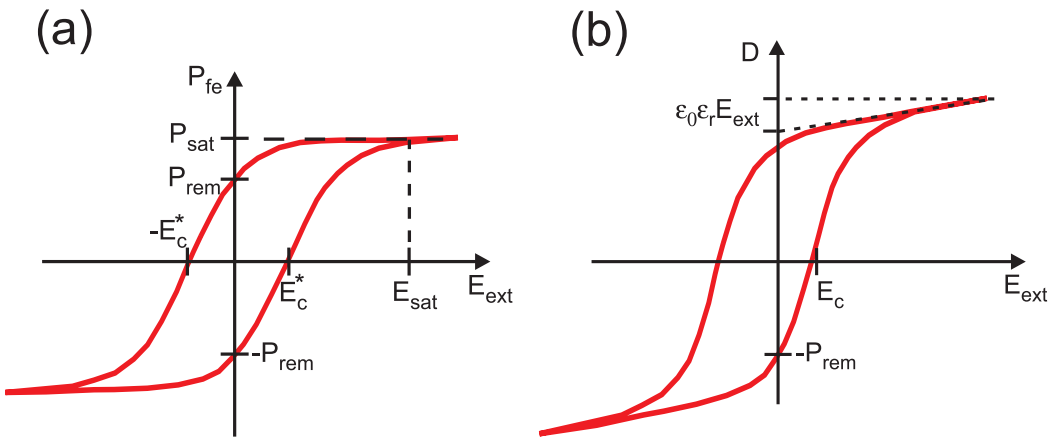


FIGURE 2.1: Ferroelectric polarization hysteresis. a) The ferroelectric part without $\varepsilon E_{ext}$. b) Ferroelectric material hysteresis.

material hysteresis [1].

A description of a stable non zero net polarization $P_{fe}$ at zero electric field can be given on the one hand by a thermodynamic view in which the free energy of the system minimizes for $P_{fe} \neq 0$ (e.g. Landau-Ginzburg-Devonshire theory) and on the other hand by a microscopic view where dipoles align due to the ordering power of dipole-dipole interaction. An approximation for the latter is given by the Weiss mean field [12]. In the Weiss mean field approximation, the ferroelectric polarization stabilizes itself by the Weiss field contribution to the local field at a site of a ferroelectric dipole. The Weiss field $E_{Weiss}$ equals the ferroelectric polarization times a coupling constant $\beta$.

$$E_{Weiss} = \beta P_{fe} \tag{2.3}$$

Ferroelectricity is in analogy to ferromagnetism only found below a certain temperature, denoted as the Curie Temperature $T_C$. Materials that are ferroelectric below $T_C$, are paraelectric above $T_C$. To clear up misunderstandings, in this work the Curie Temperature $T_C$ is defined as the lowest temperature above which all ferroelectric properties have vanished. This definition facilitates the experimental determination of $T_C$, since $T_C$ is influenced by preparational material parameters [79].

A distinction is made between order-disorder ferroelectrics, in which permanent dipoles are randomly oriented above the transition temperature and displacive ferroelectrics, like many perovskites, in which reorientable dipoles in the paraelectric phase are not clearly recognizable [22]. At the ferroelectric to paraelectric (and vice versa) transition the polarization exhibits a characteristic non-analytical functional behavior, which can be used to classify the transition, known as Ehrenfest classification.

At the phase transition, close to it or far from it, ferroelectric materials are of interest not only for physicists but also for the industry. Ferroelectric materials have numerous applications of linear and non-linear dielectric properties. "The possibility of presenting the ferroelectric material in various forms: mono and polycrystalline, meso and nano structured, massive and thin film, allows the use of ferroelectrics in

[1] In this work the ferroelectric hysteresis refers always to the ferroelectric material hysteresis.

the most divers technology applications, from devices to transform high power energy to integration in silicon electronic devices in the new technologies." [22] Details on the ferroelectric properties of P(VDF-TrFE) are given in section 2.3.5 and following sections.

## 2.2 Pyroelectricity

"Pyroelectricity is a linear reversible change in polarization brought about by a change in temperature when the electric field is held constant [47]." All ferroelectrics are also pyroelectric. The pyroelectric coefficients are generally given by [110]

$$p_{pyro,i} = \frac{dP_i}{dT} \tag{2.4}$$

where $P_i$ is the macroscopic polarization of the vector component $i$. If there is no net dipole moment along the 1 and 2 directions, which are in the plane of the electrode area, only one coefficient describes the pyroelectricity of the material. The experimental pyroelectric coefficient is then given by:

$$p_{pyro,3} = \frac{1}{A}\frac{dQ}{dT} = \frac{I_{pyro}(T)}{A} \cdot \left(\frac{dT}{dt}\right)^{-1} = j_{pyro} \cdot \left(\frac{dT}{dt}\right)^{-1} \tag{2.5}$$

where $A$, $Q$, $I_{pyro}$, $j_{pyro}$ and $(dT/dt)$ are the sample area, the charge on the electrode plates, the pyroelectric current, the pyroelectric current density and the heating/cooling rate, respectively. In contrast to the experimental definition of the pyroelectric coefficient, the thermodynamic definition of the pyroelectric coefficient takes sample area variations into account:

$$p'_{pyro,3} = \frac{Q/A}{dT} = p_{pyro,3} - \frac{Q}{A} \cdot (\alpha_1 + \alpha_2) \tag{2.6}$$

$\alpha_1$ and $\alpha_2$ are the in plane thermal expansion coefficients.

### 2.2.1 Primary and secondary pyroelectricity

The contribution to $p_{pyro,3}$ due to coupling between piezoelectricity and thermal expansion is called secondary pyroelectricity [110]. In contrast, primary pyroelectricity is associated with the change of the ferroelectric polarization with temperature. The pyroelectric coefficient due to primary pyroelectricity is given by $\frac{dP_{fe}}{dT}$ at constant strain, where $P_{fe}$ and $T$ are the ferroelectric polarization and the temperature, respectively [110]. The pyroelectric coefficient $p_{pyro,3}$ is the sum of primary and secondary pyroelectric coefficient. To observe the two parts to pyroelectricity experimentally, the sample dimensions are first clamped while the temperature is changed (primary pyroelectricity: $\frac{dP_{fe}}{dT}|_{clamped}$), subsequently the sample is allowed to relax to its equilibrium dimensions (secondary pyroelectricity) [47]. Care has to be taken not to confuse the experimental contribution to the pyroelectric signal which arises from a change in the electrode dimensions (see equation 2.6) to secondary pyroelectricity [47]. This confusion happens partially in this work, since on the top-side thin metal electrodes adhere directly to the co-polymer film and the temperature dependent lateral expansion of the metal electrode equals approximately the expansion of the co-polymer. At the bottom side the film is clamped on a rather rigid substrate, since thermal expansion coefficient of the substrate is at least one order of magnitude less

than the thermal expansion coefficient of the polymer [10, 35, 112]. So, the conditions are not truly stress free. Details on the pyroelectric properties of P(VDF-TrFE) are given in section 2.3.11.

## 2.3 The ferroelectric co-polymer P(VDF-TrFE)

P(VDF-TrFE) is a composition of polyvinylidene fluoride (PVDF) and polytrifluoroethylene (PTrFE). In this work P(VDF-TrFE) is synthesized by Piezotech® in form of randomly distributed of VDF- and TrFE units in a composition of 70/30 mol %. The monomer units of VDF and TrFE are illustrated in FIG. 2.2.

### 2.3.1 History of PVDF

The story of PVDF being a ferroelectric begins in 1969, when Kawai [45] discovered the very high piezoelectric coefficient of PVDF, after heating PVDF sheets to $\approx 100\,^{\circ}\mathrm{C}$ and subsequent cooling in presence of an electric field ($30\,\mathrm{MV\,m^{-1}}$). Shortly thereafter, it was found that PVDF is pyroelectric [6]. After some controversy of PVDF being an electret, Kepler and Anderson [46] showed by X-ray diffraction, that the polar $\beta$ phase of a poled PVDF film differs from the unpoled film, which might have been the first evidence of PVDF being a ferroelectric.

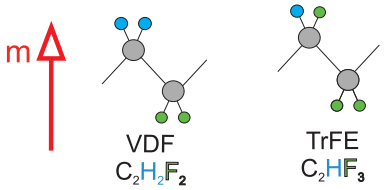


FIGURE 2.2: Monomer units of VDF and TrFE. The arrow points in direction of the strongest permanent dipole moment.

### 2.3.2 Applications of P(VDF-TrFE)

Due to excellent piezo-, pyro- and ferroelectric properties including the ease of thin film, large area and low cost production, P(VDF-TrFE) at compositions around 70/30 mol % has drawn much attention for commercial applications. Examples are:

- mechanical resonators [38], actuators [18]
- energy harvesters [85]
- refrigerators [64]
- pyroelectric image sensors [100]
- organic memory devices [9, 19, 27, 73]
- organic photovoltaic devices [118]

### 2.3.3 Crystalline structures in PVDF

In the solid state, both, PVDF and PTrFE are semi-crystalline with little exception [84]. PVDF has besides the amorphous phase at least four crystalline polymorphous referred to as the $\alpha$-, $\beta$-, $\gamma$- and $\delta$ phase previously called in order of their discovery form II, I, III and IV respectively [47, 66, 108]. In PVDF the $\alpha$ phase with a trans-gauche-trans-gauche' (TGTG') conformation (see FIG. 2.3 b)) is thermodynamically the most stable phase, but there is no net dipole moment in the pseudo hexagonal crystal structure. The $\alpha$ phase exhibits no piezo-, pyro- nor ferroelectricty. The $\alpha$ phase is obtained by cooling PVDF from the melt or from solvent casting. All other crystalline phases ($\beta$, $\gamma$ and $\delta$- phase) of PVDF are to a different content ferroelectric, whereas the $\beta$-phase is probably the most easily accessible [63]. The $\beta$-phase is usually obtained by drawing and/or poling [46, 108]. The $\beta$ crystal cell is orthorhombic and is formed by parallel and planar chains (charbon backbone) in all-trans conformation (TTTT) (see FIG. 2.3 a)).

### 2.3.4 Chemical defects: HH and TT

Depending on the synthesis conditions, the generation of defects can be favored: A certain fraction of monomer units are reversed, creating what are called head-to-head (HH) or tail-to-tail (TT) defects along the co-polymer chain. These chemical defects usually lie next to each other (HH-TT). The defect concentration impacts on the material behaviour [46, 47].

### 2.3.5 Origin of ferroelectricity in PVDF

The strongest permanent dipole moment **m** in PVDF points from the fluorine to the hydrogen atoms as depicted in FIG. 2.2 on the left. It is a consequence of the difference in electronegativity of fluorine (F) and hydrogen (H). The difference in electronegativity betweeen fluorine and carbon (C) is however often taken as reference. The dipole moment of each monomer unit equals $7.0 \times 10^{-30}$ C m [46].

### 2.3.6 TTTT- and TGTG' conformation

PVDF and P(VDF-TrFE) at a composition of 70/30 mol % exhibit similar structural conformations. P(VDF-TrFE) exhibits corresponding to the polar $\beta$ phase and the unpolar $\alpha$ phase in PVDF, the polar all-trans (TTTT) phase and unpolar trans-gauche-trans-gauche' (TGTG') phase, respectively. The TTTT- and TGTG' conformation are illustrated in FIG. 2.3. In P(VDF-TrFE) the all-trans conformation is favored due to the introduction of TrFE units (at random crystal sites), whereas for high VDF contents trans-gauche(') conformations are more stable [54]. TrFE units by themself favor the all-trans conformation [7]. Additionally, TrFE units increase locally the distance between molecules [4, 47, 120], resulting in an increased content of VDF in all-trans conformation. As a consequence $P_{rem}$ is at maximum for VDF contents in a range of 70 mol % to 80 mol % [54], at room temperature, even if the dipol moment per monomer VDF is higher than per monomer TrFE. A similar impact as by introducting TrFE units is observed by an increase of the defect concentration: The PVDF polymer favors at low defect concentrations the $\alpha$ phase, at intermediate concentrations the $\beta$ phase and for very high defect concentrations even the disordered paraelectric phase can exist at ambient temperature [47]. Besides, a real Curie transition can only be observed for VDF contents in a range of 50 mol % to 80 mol % [26].

A certain crystalline phase coexists at ambient temperature often with other crystalline phases. Altering the defect concentration by stretching, application of a high electric field or thermal annealing one phase can convert to another [47]. Consequently, the material properties of P(VDF-TrFE) depend not only on the conditions of chemical synthesis but also on the electrical, mechanical and thermal history.

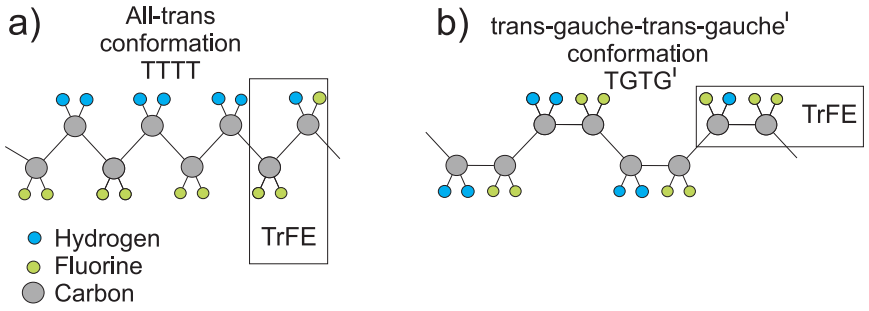


FIGURE 2.3: a) The TTTT conformation which resembles the $\beta$ phase of pure PVDF. b) The TGTG' conformation resembles the $\alpha$ phase of pure PVDF.

### 2.3.7 FE, DFE and PE phase in P(VDF-TrFE) 70/30

For the particular case of solvent cast P(VDF-TrFE) films at a composition around 70 mol % VDF the effect of thermal annealing and poling were detailed studied by Bargain et al. [3]. Their P(VDF-TrFE) film preparation method resembles the one used in this work, including the solvent cast technique (spin coating), the used solvent (2-Butanone), the annealing procedure and a similar P(VDF-TrFE) composition of 72/28 mol % to the one used in this work which is 70/30 mol %.

Bargain et al. identify three crystalline phases, namely the ferroelectric (FE), the paraelectric (PE) and the defective ferroelectric (DFE) phase. It is stated that these phases might correspond to the priorly found LT (Low Temperature), HT (High Temperature) and the CL (Cooled) phase [107], respectively. The FE phase resembles the $\beta$ phase of pure PVDF with chains in all-trans conformation and an orthorhombic crystal cell. The PE phase is similar to the $\alpha$ phase of pure PVDF with chains in trans-gauche-trans-gauche' conformation and a hexagonal crystal cell. Finally, the DFE phase consists of (all-)trans and gauche conformations in variable (i.e. temperature and electrical history dependent) ratios. The FE phase and the DFE phase subsist below the Curie Temperature [2] and the PE phase above, whereas the transition ferroelectric to paraelectric proceeds over a broad temperature range.
If not stated differently the results of Bargain et al. [3] are discussed in the following sections 2.3.7.1 and 2.3.8.2.

#### 2.3.7.1 The formation of the DFE phase by thermal annealing

The "as cast" - sample (see section 4.1) consists of amorphous material and FE phase with a degree in crystallinity of around 25 %, at room temperature. During the thermal annealing process (see section 4.1.3.2) the co-polymer film is heated above the Curie Temperature $T_C$ [3]. At the Curie transition, the FE phase disappears to the

[2] Note the definition of the Curie Temperature in section 2.1
[3] see the definition of the $T_C$ in section 2.1

benefit of the formation of the PE phase. A FE crystal transforms into a core of a PE crystal. While the FE crystal consists of P(VDF-TrFE) in all-trans conformation, in the PE crystal trans- and gauche conformations coexist. The PE crystal can incorporate gauche conformations at the borders of crystal and amorphous phase. Additionally above $T_C$ (i.e. in the PE phase) the chain molecules are inferred to be rather mobile along the chain axis: The elastic modulus along chain axis decreases at the Curie transition while cooling by one or two order(s) of magnitude and a one-dimensional diffusion motion of conformational defects along the molecular chain is suggested [83]. Besides, in the PE phase the molecular orientation can be modified via AFM-tip friction force [50]. That implies that chains can easily rearrange in the paraelectric phase and the former PE crystal core can extent. The long period [4], which is the sum of the average thickness of a crystalline region and the average thickness of an amorphous inter-crystalline region evolves from 15 nm at 30 °C to 25 nm at 115 °C to 38 nm at 130 °C.
Upon cooling the long period remains at a high value and reaches around 30 nm at room temperature, indicating a change in the co-polymers morphology takes place by thermal annealing. The FE phase appears at 80 °C while cooling from the paraelectric phase. The Curie transition while cooling occurs at lower temperature than while heating [5]. At temperatures between 80 °C to 60 °C the DFE phase appears, along with a Bragg peak which is assigned to an orthorhombic crystal cell. It is believed that the DFE phase is located at the boundary between FE crystal and amorphous material: At the Curie transition while cooling the core of a PE crystal crystallizes into a core of a FE crystal. The borders of the PE crystal crystallize into the DFE phase with chains containing conformational chemical defects, initially located in the amorphous phase at the interface with the as-cast FE crystal. While the interplanar distance [6] of the FE phase remains almost constant under further cooling from 80 °C to room temperature, the interplanar distance of the DFE phase decreases steadily towards that of the FE phase. The crystallinity steady at 25 % between 130 °C to 80 °C increases and reaches around 45 % at 50 °C and remains almost constant during further cooling to room temperature. At room temperature the FE and DFE phase contribute 2/3 and 1/3 to the overall crystallinity, respectively.
In conclusion, while thermal annealing the DFE phase is formed. DFE- and FE phase evolve differently while cooling. Thermal annealing results in a change of the polymer-morphology. Repeating the annealing process results in no further change in morphology at room temperature.

### 2.3.8 Properties of the FE- and DFE phase

#### 2.3.8.1 Structrual changes induced by poling

A poling step performed at room temperature by application of an external electric field of sufficient strength, induces reorientation of dipolar moments allowing local modification of conformations [49], healing of imperfections [54] and leads to a transformation of DFE crystals to FE crystals [3]. A slight increase in crystallinity of around 2 % and size of crystals is observed [3]. The effects of poling are erased by a heating sweep to a temperature which exceeds $T_C$ [3, 49].

[4] mostly determined in diffraction measurements

[5] The temperature hysteresis is characteristic for a 1st order Curie transition.

[6] The interplanar distance is determined from the diffraction of (110) planes. The corresponding Bragg peak is at $2\Theta = 19.9°$ and it is characteristic for the interchain order, perpendicular to the chain axis (for details see [3]).

#### 2.3.8.2 Temperature evolution of the FE and the DFE phase

As mentioned in section 2.3.7 the results of Bargain et al. [3] are discussed in this section if not stated differently. The FE and the DFE phase evolve differently in a subsequent heating sweep after thermal annealing. The interplanar distance [7] in the FE crystal remains almost constant with increasing temperature and at the Curie transition the FE phase transforms rather discontinuously to the PE phase by a rather abrupt transformation of all-trans conformations to trans-gauche-trans-gauche' conformations. This transition occurs at around 100 °C to 112 °C in PVDF-TrFE 72/28 [8]. The evolution of the FE phase while heating resembles the one while annealing (see section 2.3.7.1). In contrast, the interplanar distance in the DFE crystal, which remains almost constant in the temperature range 30 °C to 50 °C, increases substantially and steadily in the temperature range of 50 °C to 100 °C. At temperatures between 80 °C to 100 °C the DFE phase transforms into the PE phase by continuously transforming trans- to gauche/ gauche' conformations. At around 100 °C the structural transformation from orthorhombic to hexagonal occurs. The transition from DFE to PE phase occurs rather at a cricital cell expansion than at a specific temperature. In this context, it's worth mentioning that the Curie endotherm can be altered by a specific annealing procedure below the Curie Temperature, known as consecutive annealing. After consecutive annealing, the DFE to PE phase transition occurs at a different temperature but for the same critical cell parameters as observed for standard annealed samples. At temperatures above $T_C$ only the PE phase in PE crystals and the amorphous phase subsist and the previous history (poling [49], thermal history [49]) is erased. Subsequent cooling repeats the pattern observed while thermal annealing stated in section 2.3.7.1.

### 2.3.9 Mesoscopic structures in the co-polymer

The P(VDF-TrFE) film is after sample preparation packed in between two metallic electrode plates. FIG. 2.4 illustrates the mesoscopic structures in the P(VDF-TrFE) film. This picture is drawn by compiling literature based information. The co-polymer film consists basically of ferroelectric crystallites, which are embedded in an amorphous matrix. A ferroelectric crystallite consists of a core of FE phase, which is enveloped by the DFE phase. The ferroelectric crystallites stand on-edge [51, 58]. Not drawn in FIG. 2.4 are grain boundaries.

#### 2.3.9.1 Orientation of chains and crystallites / lamellae

Molecular chains of P(VDF-TrFE) order periodically and form crystalline regions so called lamellae, which are embedded in an amorphous matrix. In this work the term ferroelectric crystallite and lamellae are used as synonyms. The polymer chain length of a PVDF polymer exceeds usually 10000 monomers [46]. One single chain might start in the amorphous, enter a lamella, leaving the lamella into the amorphous and fold back to reenter the lamella and so forth. According to their spatial arrangement one distinguishes tie molecules, loops, free ends and floating chains. In spin-cast thermally annealed polymer films, as used in this work, the chains are predominantly oriented parallel to the substrate so that the crystallites stand on edge (see FIG. 2.4), so called edge-on (lamellar) crystallites, with preferential (200) and (110) contacts to the substrate surface [51, 58].

[7] specified in section 2.3.7.1

[8] In this work a slightly different composition of 70/30 mol% is used, see section 4.1.3. The ferroelectric to paraelectric transition temperatures depend on the composition [67].

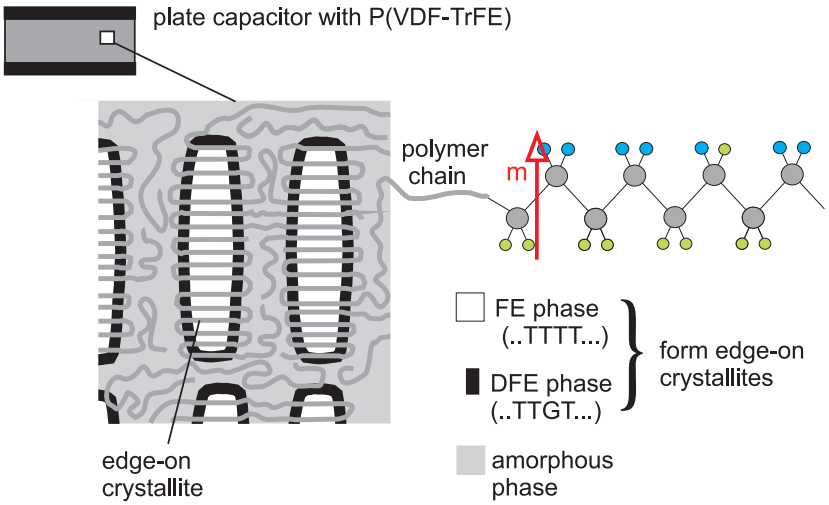


FIGURE 2.4: Macro-, meso- and microscopic structure(s) of/within the sample. The P(VDF-TrFE) film is spin-cast and thermally annealed.

#### 2.3.9.2 Degree in crystallinity

At room temperature and for the sample preparation process used in this work the co-polymer is semi-crystalline. The degree of crystallinity increases by thermal annealing between $T_C$ and $T_m$ (melting temperature) [48, 74], as was discussed in section 2.3.7.1. By variation of the maximum annealing temperature $T_{anneal}$, where usually $T_C < T_{anneal} < T_m$, the degree in crystallinity can be altered, whereas the achieveable remanent polarization remains almost constant for annealing in this temperature range [74]. The crystallinity reaches a maximum at $T_{anneal} \approx 144\,^{\circ}\mathrm{C}$ [74]. $T_m$ equals approximately 146 °C [74].

#### 2.3.9.3 Grains and surface roughness

The co-polymer film exhibits randomly oriented grains, which can be detected with atomic force microscopes (AFM), scanning electron microscopes (SEM) and lateral-modulation friction force microscopes (LM-FFM) [50, 74, 77, 117]. By increasing the maximum annealing temperature $T_{anneal}$, the grain size increases (60 nm at $T_{anneal}$ = 120 °C, 130 nm at $T_{anneal}$ = 135 °C ) and the shape of grains changes from ellipsoid-like ($T_{anneal} \approx 120\,^{\circ}\mathrm{C}$) to rod-like ($T_{anneal} > 140\,^{\circ}\mathrm{C}$), which is accompained by an increase of surface roughness [74, 77]. The grain size after thermal annealing is decreased for thin polymer films [74]. Under high pressure and constriction of the co-polymer surface by PTFE templates, the increase of surface roughness with increasing annealing temperature can be prevented [117].
In literature the terms grain and crystallite are not clearly differenciated. It seems not clear if a grain exhibits several ferroelectric crystallites or if a grain confines only one ferroelectric crystallite. While the latter is evidenced by the uniform friction force along the surface of a grain [50], the former is based on the value of the long period (see section 2.3.7.1), which is almost an order of magnitude smaller than the average grain size. A detailed analysis concerning the matter is presented by Lee et al. [58] suggesting an average grain to consist out of 12 lamellae (lamella = ferroelectric crystallite).

### 2.3.10 Ferroelectric polarization reversal in P(VDF-TrFE)

The microscopic mechanism of ferroelectric polarization reversal, which inevitably includes a dipole reorientation or dipole flipping motion, is controversially discussed. The involved dipoles are illustrated in FIG. 2.2. The most recent model proposed includes a 120° or a 180° dipole rotation about the molecular chain [101]. The rotations can be achieved in two different ways: (1) solitonic propagation of a kink wave and (2) simultaneous rotation of all the dipoles in a chain. The solitonic propagation of a kink wave is accepted as more plausible [25].
The ferroelectric polarization switching time $\tau$ is defined as the duration required to flip the orientation of the ferroelectric polarization by application of an externally applied electric field pulse of certain amplitude $E_{ext}$. The ferroelectric polarization switching transient $P(t)$ can be approximately described by a stretched exponential function [24, 69]

$$P(t) = P_{switch}(E_{ext}) \left(1 - \exp\left(\frac{t}{\tau}\right)^{\delta}\right) \tag{2.7}$$

where $\delta$ is a stretching factor with values between 0 and 1. $P_{switch}$ is the amount of switchable polarization. If not stated differently, equation (2.7) is used to determine $\tau$ from the best fit to an experimental ferroelectric polarization switching transient.
Studies on ferroelectric polarization switching processes in several ferroelectric materials have shown, that the ferroelectric polarization switching time $\tau$ follows either a power law (at high field strength [59])

$$\tau = \tau_{0,power} \cdot E_{ext}^{-n} \tag{2.8}$$

or an exponential law (at low field strength [59])

$$\tau = \tau_{0,exp} \cdot \exp\left(\frac{E_a}{E_{ext}}\right) \tag{2.9}$$

$\tau_{0,power}$, $\tau_{0,exp}$ and $E_a$ are constants, n is close to 1 and $E_{ext}$ is the amplitude of the electric field step applied. Equation (2.8) and (2.9) were found empirically by Merz [76]. Phenomenological models of nucleation and growth have been proposed, which give the forms in equation (2.8) and (2.9) [23, 24]. The ferroelectric polarization switching process speeds up with increasing temperature Arrhenius like:

$$\tau = \tau_{0,Arrh} \cdot \exp\left(\frac{W_a}{k_B T}\right) \tag{2.10}$$

In P(VDF-TrFE) 70/30 the constants $\tau_{0,Arrh}$ and $W_a$ are found to be $5 \times 10^{-10}$ s and 0.54 eV, respectively [69].
The coercive field $E_c$ and $\tau$ are closely related. In this work, $E_c$ is found by application of an alternating triangular electric field signal. $E_c$ depends on the frequency of the applied field signal and on the temperature. $E_c$ increases linearly as a logarithmic function of the frequency [70]. $E_c$ is piecewise, between 30° to 80° and between −20° to 10°, a linear function of the temperature, with differing slope in these two temperature regimes [69, 123]. Table 2.1 lists some exemplary values of $\tau$ and $E_c$.

TABLE 2.1: Basic ferroelectric polarization switching properties of P(VDF-TrFE) 70/30

| | | |
|---|---|---|
| Ferroelectric polarization switching time $\tau$ | 30 µs | at 25 °C; step $E_{ext}$=100 MV m$^{-1}$ [106] |
| Coercive field $E_c$ | $\approx$ 60 MV m$^{-1}$ | at 30 °C; frequency of $E_{ext}$: 1 Hz [74] |

### 2.3.11 Pyroelectric response in PVDF and P(VDF-TrFE)

In PVDF polymers the in plane linear thermal expansion coefficients ($\alpha_1$ and $\alpha_2$ in equation (2.6)) are of the order $10^{-4}$ K$^{-1}$ [112]. Thus $p'_{pyro,3}$ can be around 50 % higher than $p_{pyro,3}$ [9]. The pyroelectric coefficient $p_{pyro,3}$ increases piecewise linearly in each of the following regimes for temperatures between $-100$ °C and 50 °C: $T < T_{gl}$, $T_{gl} < T < T_{gu}$ and $T_{gu} < T_\alpha$, where $T_{gl}$, $T_{gu}$ and $T_\alpha$ are the glass-, upper glass- and $\alpha_c$-relaxation transition temperature, respectively [112]. Variations in $p_3(T)$ are not linear above $T_\alpha$ (see section 2.3.11.2). The transition temperatures are given in table 2.2. In the glassy state ($T < T_{gl}$) primary pyroelectricity seems to play a major

TABLE 2.2: Transition temperatures determined by DSC and pyroelectric measurements for P(VDF-TrFE) 75/25 [40]

| *Method* | $T_{gl}$ | $T_{gu}$ | $T_\alpha$ |
|---|---|---|---|
| DSC | $-36$ °C | 5 °C | 46 °C |
| pyrocurrent | $-38$ °C | 10 °C | 60 °C |

role [110, 112]. Primary pyroelectricity can in its most simplified representation be understood as the reversible change in average dipole orientation with changing temperature;

$$P_{fe} = \frac{N}{V} m_{fe} < cos\theta > \quad \xrightarrow{\text{equation(2.4)}} \quad p_{primPyro} = \frac{N}{V} m_{fe} \frac{d < cos\theta >}{dT} \tag{2.11}$$

In equation (2.11) $N$, $V$ and $m_{fe}$ are the number of ferroelectric dipoles, the sample volume and the elementary ferroelectric dipole moment and $< cos\theta >$ is the averaged cosine of the angle between the individual ferroelectric dipoles and the 3-axis (axis perpendicular to the electrode plane) [110]. More complex models on primary pyroelectricity in PVDF polymers include that the dipole moment is dependent on the local field, dipole libration and other effects [47, 110]. Throughout the glass transition range ($T_{gl} < T < T_{gu}$), the observed increase in pyroelectricity can be mainly attributed to secondary pyroelectricity [110]. Secondary pyroelectricity appears to be well described by the rigid dipole model, which assumes dimensional variations (thermal expansion) coupled with the polarization of crystallites [110, 112]. These dimensional variations arise mainly from the amorphous phase [110]. The pyroelectric coefficient due to secondary pyroelectricity along the 3-axis is in the rigid dipole model is given by:

$$p_{secPyro,3} = -P_{fe} \cdot \alpha_3 \tag{2.12}$$

[9] $p'_{pyro,3}$ and $p_{pyro,3}$ are defined in section 2.2. Note also the discussion on in plane thermal expansion, regarding unsymmetric top- and bottom side sample structure, given in section 2.2.1

$\alpha_3$ is the thermal expansion coefficient in direction perpendicular to the electrode plane. Besides, it was shown that the total experimental pyroelectric coefficient in PVDF is proportional to the remanent polarization $P_{rem}$ [11, 47].

$$p_{pyro,3} \sim -P_{rem} \tag{2.13}$$

Some values of $p_{pyro,3}$ at certain temperatures are given in table 2.3. The pyroelectric coefficient is usually measured in short circuit conditions while measuring the exchanged charge between the two electrodes when the sample temperature is changed by a known amount. Two conventional techniques are then applied: A dynamic method consisting of measuring the current when sinusoidally modulated thermal radiation is applied. A more direct method consists in measuring the short circuit current by changing the temperature with constant rate. The latter method is used in this work.

TABLE 2.3: $p_{pyro,3}$ at different temperatures in P(VDF-TrFE) 75/25 [40]

| $T\,[^\circ\mathrm{C}]$ | -60 | -30 | 0 | 20 | 40 |
|---|---|---|---|---|---|
| $p_{pyro,3}\,[\mu\mathrm{A\,s\,m^{-2}\,K^{-1}}]$ | -11.5 | -14 | -18.5 | -23 | -38 |

#### 2.3.11.1 Pyroelectric response of poled and un-poled samples

The pyroelectric (current) response of a poled sample is found to be several orders of magnitude higher compared to that of an un-poled sample [103]. It is assumed that the ferroelectric polarization vectors of ferroelectric crystallites ($\mathbf{P}_{fe-cryst}$) point in random directions in an un-poled sample. In this work, un-poled samples are those which have never been subjected to a high electric field ($E_{ext} << E_c$). A similar pyroelectric current response as for un-poled samples is expected for samples, which have been annealed in the paraelectric state (i.e. de-aged above $T_C$ see section 5.2.3) initial to the measurement, since annealing above $T_C$ is known to delete the thermal and electrical history [3] [10]. Assuming the ferroelectric polarization ($P_{fe}$) to be the only polarization present in the polymer film, the current density due to primary and secondary pyroelectric effect (see section 2.2.1) can be written as

$$j_{pyro} = \frac{dP_{fe}}{dT}\frac{dT}{dt} \tag{2.14}$$

where $\frac{dT}{dt}$ and is the rate of change in temperature T with respect to time t. Assuming, that $P_{fe-max}$ equals the value of the ferroelectric polarization in the case that all $\mathbf{P}_{fe-cryst}$ point straight towards the same electrode, then equation (2.14) can be rewritten as

$$j_{pyro} = \eta\frac{dP_{fe-max}}{dT}\frac{dT}{dt} \tag{2.15}$$

where $\eta$ is a dimensionless factor, which takes the spatial distribution of $\mathbf{P}_{fe-cryst}$ into account [10].

Pyroelectricity is per definition defined only for reversible changes in polarization brought about by a change in temperature (see section 2.2). Thus, irreversible

[10] In the course of this work this assumption is found to hold, see section 6.2.3.

changes of the ferroelectric polarization due to irreversible reorientation of $\mathbf{P}_{fe-cryst}$ or incorporation of thermal defects into the DFE phase in the broad Curie transition temperature range (see section 2.3.8.2 and [3]) are in this definition not included. Besides, structural changes, such as transformations from orthorhombic to hexagonal crystal cells at the Curie transition (see section 2.3.8.2), as well as reversible changes in crystallinity do not belong to primary nor secondary pyroelectricity. Kepler and Anderson [47] established a thermodynamic formalism for the latter. In the case of PVDF, the prediction of the formalism and experimental observation were however not found to match really up [47]. Integration of $j_{pyro}$ in equation (2.14) respective to time across the Curie transition range yields the ferroelectric polarization, which had decayed/built-up while heating/cooling, even if structural changes occur. This is because the integral effectively considers only the difference in polarization between the initial and final state.

#### 2.3.11.2 $\alpha_c$ - relaxation

The $\alpha_c$ relaxation is a not-well understood process described in literature which contributes to the pyroelectric response. It occurs dependent on the thermal history at temperatures between 20 °C to 100 °C [82]. The $\alpha_c$ process appears not only in pyroelectric currents [82, 96, 112], but also in differential scanning calorimetry traces as a small endotherm [65, 112, 113], in storage and loss tensile moduli [95] and in the electric permittivity [95]. The $\alpha_c$ relaxation is connected to pyroelectric [113] and piezoelectric [56] aging. Both, for the pyroelectric [40, 82] and the piezoelectric [56] aging a logarithmic dependence on the storage time is observed. For temperatures just above the $\alpha_c$ relaxation, relaxation processes are found to follow a specific temperature dependence known as the compensation law [11] [113].

[11] The compensation law is given in equation (6.6) and discussed in section 6.9.3 seqq.

# Chapter 3

# Theoretical basis II: Ferroelectric Imprinting

## 3.1 Introduction to ferroelectric imprint

Imprinting often addresses the phenomenon that the ferroelectric polarization hysteresis shifts along the electric field axis over time. The process depends on the duration $t_w$, which is the time waited in a certain ferroelectric polarization state (e.g. $\pm P_{rem}$). Imprint is observed in several ferroelectric materials like PZT ceramics [13], $BaTiO_3$ [2], BNdT ceramics [121], SBT ceramics [1] and also in P(VDF-TrFE) [41]. Various models have been proposed to explain imprinting and it seems that the underlying mechanism also varies with the ferroelectric material under investigation. This work deals solely with the imprint mechanism in the co-polymer P(VDF-TrFE), whereas it is possible that the New Imprint Model presented in section 3.3 can be transferred to other ferroelectric materials.

## 3.2 Imprint models literature review: Imprinting in P(VDF-TrFE)

Several attempts were made to understand the imprint mechanism in P(VDF-TrFE). The models used to understand imprinting are now presented in chronological order of appearance in literature.

### 3.2.1 Definition of the waiting time $t_w$

The waiting time is defined as the time elapsed since introducing a non-zero ferroelectric polarization. Experimentally, that definition is impractical, since the ferroelectric polarization is present at all times below the Curie Temperature. The experimental waiting time is defined in section 4.3.3. In the results section the literature model are revised in the light of our experimental findings.

### 3.2.2 Space Charge Model

To the authors knowledge, the first model to explain imprinting in P(VDF-TrFE) was presented by Ikeda et al. [41]. They suggested space charges, mobile in the amorphous phase, to accumulate at the edges of ferroelectric crystallites during $t_w$. The accumulated space charges collectively generate a field within the crystallite. This

field stabilizes the ferroelectric polarization state and hinders ferroelectric polarization reversal. The mechanism described by the Space Charge Model is illustrated in FIG. 3.1.

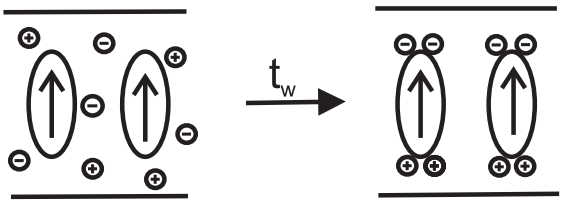


FIGURE 3.1: Space Charge Model.

### 3.2.3 Dead Layer Model

The dead layer model was first used to explain imprinting in PZT ceramics [30] and was then adapted for P(VDF-TrFE) [57, 125]. The model is outlined in FIG. 3.2. In the model charges are injected from the electrode into an electrode adjacent non-ferroelectric "dead layer" during $t_w$. The driving force for charge injection is the field $E_{dl}$ (see equation 3.2) , which is generated by the ferroelectric polarization $P_{fe}$ in the bulk.

In short circuit condition:

$$E_{depol} = \frac{P_{fe} d_{dl}}{\varepsilon_0(\varepsilon_{dl} d_{bu} + \varepsilon_{bu} d_{dl})} \quad (3.1)$$

$$E_{dl} = -E_{depol} \cdot \frac{d_{bu}}{d_{dl}} \quad (3.2)$$

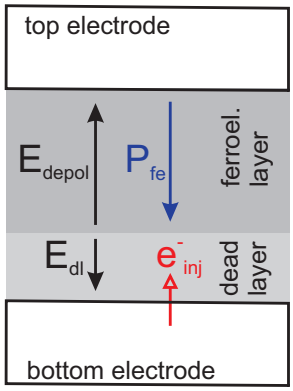


FIGURE 3.2: Dead Layer Model.

In equation (3.1) and (3.2), $d_{bu}$, $d_{dl}$, $\varepsilon_{dl}$ and $\varepsilon_{bu}$ are the thicknesses and the permittivities of the ferroelectric bulk (bu) and the dead layer (dl), respectively. $\varepsilon_0$ is the vacuum permittivity. Injected charges accumulate during $t_w$ in the dead layer and progressively screen the ferroelectric polarization. As a consequence, the remanent polarization decays as a function of $t_w$. Additionally, the injected charges hinder the ferroelectric polarization reversal (in the beginning of the ferroelectric switching process) by reducing the depolarization field $E_{depol}$. In literature this model is often used to explain imprinting in ferroelectrics [30, 31, 105].

### 3.2.4 Deep Traps Model

Lew et al. presented the Deep Traps Model to explain imprinting in P(VDF-TrFE) [60, 61]. The proposed mechanism was designed to give reason to the huge time span over which imprinting evolves: $E_c(t_w)$ was shown to steadly increase over at least 10 decades ($10^{-4}$ s to $10^6$ s) of $t_w$, without any indication of reaching an end

value [61]. The model assumes electronic trap states to be filled and emptied by thermal excitation. "Based on the logarithmic behavior ... these charge trap states are distributed approximately uniformly in energy and stabilized by the orientation of the polymer dipoles [61]". Lew et al. presented, that imprinting can be monitored in the short circuit while heating [60, 61].

## 3.3 The New Imprint Model

This imprint model [52, 86, 87] was designed in the course of this work. It will be used to explain several experimental results associated to imprinting. The model is based on previous imprint models, but overcomes disagreements to experimental observations, some of which are presented in sections 5.6 and 5.7. In this model the mesoscopic structures present in the co-polymer film, which are in detail discussed in section 2.3 play an important role. The mesoscopic structures in the co-polymer can briefly be described as, the co-polymer material consists of ferroelectric crystallites which are embedded in a non-ferroelectric amorphous phase. A ferroelectric crystallite is composed of two different ferroelectric phases, denoted as FE and DFE phase (see section 2.3.9). The FE, DFE and amorphous phase exhibit permanent dipoles with the repeat formula $(CH_2 + CF_2)_n$ (see FIG. 2.4). Still these dipoles are differentiated, depending on their location. Permanent dipoles in the ferroelectric crystallite are denoted as ferroelectric dipoles (fd) and dipoles in the amorphous phase are denoted as relaxational dipoles (rd). While the fd remain fixed with the ferroelectric polarization state (due to dipole-dipole coupling, which can conveniently be described by the Weiss mean field) the rd reorient in time. A detailed description of fd and rd is given in section 3.3.2.

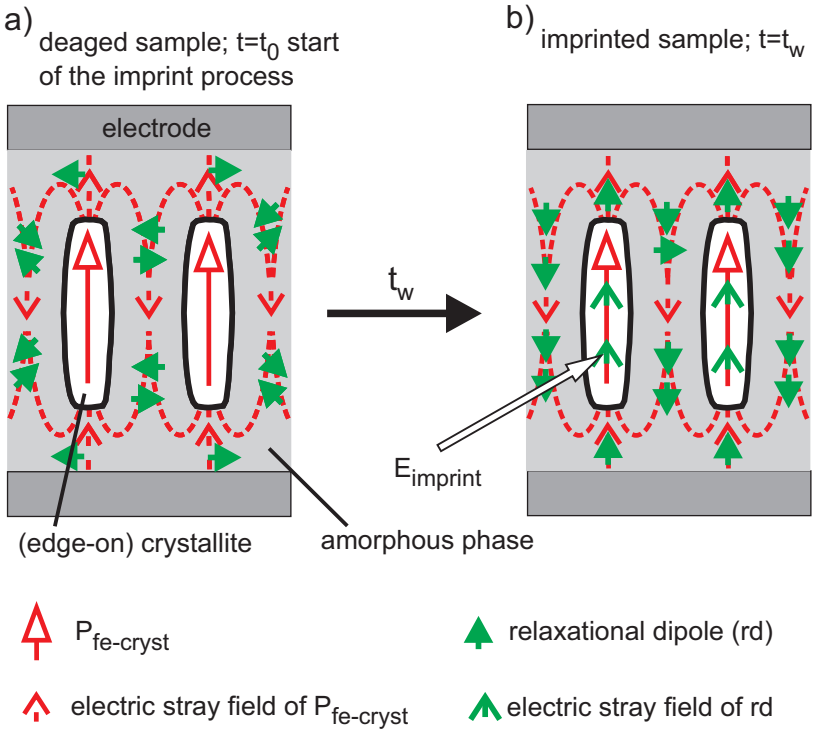


FIGURE 3.3: The New Imprint Model: a) No imprint. b) Imprinted state. Reproduced from [87], with the permission of AIP Publishing.

FIG. 3.3 outlines the mechanism of imprinting in the New Imprint Model. Note, the co-polymer structures shown in FIG. 3.3 are in more detail presented in FIG. 2.4. Lets assume that at $t = 0$ all fd point perpendicular to the electrode surface and all rd point statistically in random directions. The aligned fd jointly build up the ferroelectric polarization in the crystallite, denoted as $P_{fe-cryst}$. As long as the sample remains in the remanent ferroelectric polarization state ($P_{rem}$) the fd are assumed to be immobile, that means that $P_{fe-cryst}$ remains constant during $t_w$. $P_{fe-cryst}$ generates an electric stray field in the surrounding of the ferroelectric crystallite, illustrated in dashed red lines in FIG. 3.3. This stray field acts on the rd and forces them to reorient. After reorientation the rd point in the direction of the stray field. The rd are assumed to relax independently from each other and to exhibit a distribution of relaxation times (see section 3.3.3). $t_0$ is the shortest relaxation time of rd, thus in the time period $0 \leq t < t_0$ the rd remain to point in random directions and imprint is zero [1]. The zero imprint situation is illustrated in FIG. 3.3 a). In the time period $t_0 < t < t_w$, imprinting progresses: the rd reorient gradually, according to their relaxation time. As soon as some rd have aligned a feedback comes into play: The aligned rd evoke themselves jointly a stray field. This stray field is denoted as electric imprint field $E_{imprint}$ at the location of $P_{fe-cryst}$ (see FIG. 3.3 b)). Note, $E_{imprint}$ points in the direction of $P_{fe-cryst}$. Consequently, $E_{imprint}$ stabilizes $P_{fe-cryst}$ and also the overall ferroelectric polarization $P_{fe}$ [2]. Thus, $E_{imprint}$ obviously acts as hindrance to ferroelectric polarization reversal.

### 3.3.1 Experimental observations leading to the New Imprint Model

There are crucial experimental observations which led to the New Imprint Model and which conversely can be explained by the model. These observations are:

- imprinting is coupled to the ferroelectric polarization: The effects of imprinting ($E_c(t_w)$, $\tau(t_w)$, $P_{rem}(t_w)$ and $\varepsilon(t_w)$, see also section 5.1) evolve symmetrically with respect to both (positive and negative) remanent polarization states (see section 5.1).

- all imprint effects evolve independent of the co-polymer film thickness (see section 5.3). Thus, imprinting is not an interface related effect as assumed in the Dead Layer Model (see section 3.2.3).

- a change in the degree in crystallinity of the co-polymer, impacts on the speed of which imprint effects proceed $\rightarrow$ amount of non crystalline phase plays a role in the imprinting mechanism (see section 5.11).

- imprinting evolves over several decades in time $\rightarrow$ several concurrent processes involved, which proceed on different time scales $\rightarrow$ broad distribution of relaxation times (see section 5.8).

- imprint impacts on the ferroelectric polarization switching processes in a manner as if the external electric field applied is reduced $\rightarrow$ existence of an inherent imprinting field (denoted as $E_{imprint}$) which superimposes with the externally applied electric field (see section 5.8).

- the imprint current density ($j_{rel}$) behaves like: $j_{rel} \sim t_w^{-\alpha}$ with $\alpha \approx 1$ (see section 5.9). Such a relation between short circuit current density and time is typically

[1] Side note: $t_0$ also appears in equation (5.3)

[2] see the definition of $P_{fe}$ and $P_{fe-cryst}$ in section 3.3.4

found for a system of independently relaxing polarization processes with a broad distribution of relaxation times (see section 3.4).

- the irreversible current density ($j_{irrev}$) which is observed in pyroelectric experiments is identified as the imprint current density $j_{rel}$ (see section 6.8). Using the New Imprint Model, in particular by assuming a system of independently relaxing polarization processes with a broad distribution of relaxation times, described by a uniform energy barrier distribution, $j_{rel}$ while heating is successfully [3] calculated (see section 6.9).

### 3.3.2 fd and rd - Dipoles in the New Imprint Model

P(VDF-TrFE) contains a strong permanent dipole moment that points from the fluorine atoms to the hydrogen atoms, as indicated by a red arrow in FIG. 2.2 and FIG. 2.4. In the New Imprint Model, these permanent dipole moments belong to two types of dipoles:

- ferroelectric dipoles (fd), are located in the ferroelectric crystallites. In the ferroelectric crystallites the TTTT conformation prevails (see section 2.3.9). The fd are stably aligned and build up $P_{fe-cryst}$.

- relaxational dipoles (rd) are dipoles in the amorphous phase. The amorphous phase is not ferroelectric and initially ($t_w$ =0) not polarized. The rd point in random direction at $t_w$=0. The rd exhibit a broad distribution of relaxation times for dipole reorientation which is reasoned in section 3.3.3. Besides, in the New Imprint Model it is assumed that the rd reorient independently from each other. During the waiting time $t_w$ the rd reorient in the stray field generated by $P_{fe-cryst}$.

### 3.3.3 Dipole reorientation in the amorphous phase - origin of the distribution of relaxation times

Reorientation of a permanent dipole occurs through sequential rotation of monomer units. A calculation of the maximum energy barrier along such a pathway predicts a value of 0.9 eV for pure PVDF in the amorphous phase, while local maxima differ in a range $0.1\,\text{eV} \leq W_i \leq 0.9\,\text{eV}$ [122]. The sequential rotation of monomer units depends on the local field generated by neighboring dipoles. For example, the sequential rotation of monomer units is easier adjacent to TrFE monomers [122]. It is assumed that, once kicked off, the sequential rotation of monomer units is very fast, compared to the (actual) relaxation time which elapses to commence the kick off. A small range of energy barriers such as $0.1\,\text{eV} \leq W_i \leq 0.9\,\text{eV}$, leads to relaxation times, which are distributed over 13 decades at room temperature calculated by Boltzmann's factor for thermally activated relaxation processes (e.g. Arrhenius equation (2.10)).

### 3.3.4 The polarizations $P_{fe-cryst}$, $P_{fe}$, $P_{rel}$ and $P_{rem}$

Four types of polarizations are differentiated in the New Imprint Model. For clarity and comprehensibility they are listed in the following:

[3] Successful, in the sense that the calculated short circuit currents while heating fit well to the experimental counterparts.

- ferroelectric polarization in a ferroelectric crystallite $P_{fe-cryst}$: This polarization exists inside the ferroelectric crystallites and is build-up by the alignment of fd.
- ferroelectric polarization $P_{fe}$: This polarization exists in the total volume $V$ between the electrode plates and is caused by aligned fd.
- relaxational polarization $P_{rel}$: This polarization exists in the total volume between the electrode plates and is caused by aligned rd.
- remanent ferroelectric polarization $P_{rem}$: This is the total polarization measured on the electrode plates at zero external field. Considering $P_{fe}$ and $P_{rel}$ to be the prevalent polarizations in the sample gives $P_{rem} = P_{fe} + P_{rel}$ [4].

## 3.4 Mathematical derivation of $j_{rel} \sim t^{-1}$

In this section the $t^{-1}$ behavior of the short circuit current density is derived, which is a characteristic of imprint, as presented in the result sections 5.1 and 5.9. In the following it will be shown that the $t^{-1}$ behavior can be derived assuming a distribution of relaxation times. As stated in section 3.3.3, the rd exhibit a distribution of energy barriers 0.1 eV$\leq W \leq$0.9 eV for dipole reorientation which results in a broad distribution of relaxation times. Assuming the distribution density function

$$g(W) = g_0 \quad \text{for} \quad W_1 \leq W \leq W_2 \tag{3.3}$$

where $W_1$=0.1 eV and $W_2$=0.9 eV [87]. From the energy barrier $W_i$ the relaxation times of relaxational dipoles $\tau_{rd,i}$ can be calculated, e.g. using the Arrhenius equation (6.7). For convenience instead of $\tau_{rd,i}$ simply $\tau_i$ is written. In the following the continuous counterpart to $\tau_i$ is used:

$$\tau_i \underset{\text{discrete}}{\overset{\text{continuous}}{\rightleftharpoons}} \tau_{rd} \tag{3.4}$$

The distribution density function $f(\tau_{rd})$ of $\tau_{rd}$ is related to $g(W)$ by:

$$f(\tau_{rd})d\tau_{rd} = g(W)dW \tag{3.5}$$

Inserting equation (3.3) in equation (3.5) and assuming an Arrhenius temperature dependence for the relaxation frequencies yields

$$g(W) = g_0 = \frac{1}{k_B T}\tau_{rd} f(\tau_{rd}) \rightarrow f(\tau_{rd}) = \frac{g_0 k_B T}{\tau_{rd}} \tag{3.6}$$

Let $P_{rel,eq}$ be the equilibrium polarization in a system of relaxational dipoles. To an interval $d\tau_{rd}$ belongs

$$dP_{rel} = P_{rel,eq} f(\tau_{rd}) d\tau_{rd} \tag{3.7}$$

[4] In the New Imprint Model $P_{fe}$ and $P_{rel}$ are usually oriented in anti-parallel fashion. In the New Imprint Model $P_{fe}$ remains constant during $t_w$ and $|P_{rel}|$ increases as a function of $t_w$, thus $|P_{rem}|$ decays as a function of $t_w$ (see section 5.1).

The time dependent polarization $dP_{rel}$ is a solution of the relaxation equation (3.8). $dP_{rel}$ relaxes towards $dP_{rel,eq}$ and equals $dP_{rel,eq}$ in the limit of infinite time.

$$\tau_{rd}\frac{\partial}{\partial t}dP_{rel} + dP_{rel} = dP_{rel,eq} \tag{3.8}$$

Lets start in $dP_{rel,eq} = 0$ with $dP_{rel} = 0$. The presence of an homogeneous electric field which is switched on at $t = 0$ (e.g. application of an electric field step) results in $dP_{rel,eq} \neq 0$. Equation (3.8) is then solved by

$$dP_{rel} = dP_{rel,eq}\left(1 - e^{-t/\tau_{rd}}\right) \tag{3.9}$$

The time dependent current density $dj_{rel}$ in the outer circuit can be calculated via derivation of $dP_{rel}$ respective to time

$$dj_{rel}(t) = dP_{rel,eq} \cdot \frac{1}{\tau_{rd}}e^{-t/\tau_{rd}} \overset{(3.7)}{=} P_{rel,eq}f(\tau)d\tau_{rd} \cdot \frac{1}{\tau_{rd}}e^{-t/\tau_{rd}} \tag{3.10}$$

Integration over relaxation times within the range $\tau_{rd,1} \leq \tau_{rd} \leq \tau_{rd,2}$ yields

$$j_{rel}(t) = P_{rel,eq}\int_{\tau_{rd,1}}^{\tau_{rd,2}} f(\tau_{rd}) \cdot \frac{1}{\tau_{rd}}e^{-t/\tau_{rd}} \cdot d\tau_{rd} \tag{3.11}$$

$$\overset{(3.6)}{=} P_{rel,eq} \cdot g_0 k_B T \int_{\tau_{rd,1}}^{\tau_{rd,2}} \frac{1}{\tau_{rd}^2} \cdot e^{-t/\tau_{rd}} \cdot d\tau_{rd} \tag{3.12}$$

$$= P_{rel,eq} \cdot g_0 k_B T \left(e^{-t/\tau_{rd,2}} - e^{-t/\tau_{rd,1}}\right) \cdot t^{-1} \tag{3.13}$$

Thus, $j_{rel}(t) \sim t^{-1}$.

Note, the following normalization applies:

$$\int_0^\infty g(W)dW = 1 \xrightarrow{g(W)=g_0} g_0 = \frac{1}{W_2 - W_1} \tag{3.14}$$

# Chapter 4

# Experimental details

This chapter describes the procedures of P(VDF-TrFE) film preparation and the used measurement setups.

## 4.1 Sample preparation

The sample structures illustrated in FIG. 4.1 are processed. The list below enumerates the steps followed while sample preparation in the chronological order:

- Cleaning the substrate
- Formation of bottom electrodes
- P(VDF-TrFE) film preparation
- Annealing
- Formation of top electrodes

✓ Sample ready for testing

The active area of the P(VDF-TrFE) co-polymer film is after sample preparation confined by two electrically conducting electrodes, forming a plate capacitor structure (see FIG. 4.1). Each sample component and procedure during sample preparation is in the following discussed in detail.

### 4.1.1 Substrate

The substrate is the bottommost component in the plate capacitor stack. As substrate serve thin glass plates (see FIG. 4.1 a)), highly doped silicon wavers (see FIG. 4.1 b)) and failure wavers (see FIG. 4.1 c)) kindly provided for free by Siltronic AG. Since the thickness of the glass substrate plays a role in pyroelectric- and related experiments, its thickness is given here: 1 mm. Highly doped silicon functions at the same time as substrate as well as bottom electrode (see FIG. 4.1 b)). Highly doped silicon substrates are used if it comes to a comparative study between epitaxial grown P(VDF-TrFF) films and casually processed P(VDF-TrFE) films. This includes the samples which are processed to study the dependence of imprinting on the degree of crystallinity, presented in section 5.11. Failure wavers exhibit a very smooth surface. A smooth substrate surface is a precondition for processing large area films with low film-thickness variation e.g. for IR investigation.

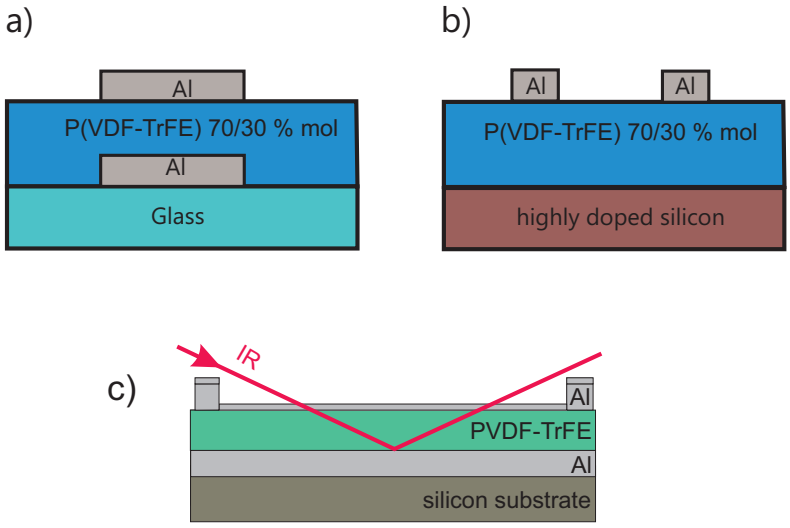


FIGURE 4.1: Sample structures. a) Standard sample. b) Sample for investigating the crystallinity dependence. c) Sample with IR transparent top electrode.

The first step in the sample preparation process is cleaning the substrate. The cleaning process follows the below-mentioned steps in chronological order:

- mechanical cleaning of the substrates surface with a fuzz-free tissue soaked with isopropanol.
- ultra-sonic bath in isopropanol at 50 °C for 15 min
- drying the substrate in a nitrogen stream
- ultra-sonic bath in distilled water at 50 °C for 15 min
- drying the substrate in a nitrogen stream

After cleaning, the glass plates and silicon failure wavers (not the highly doped silicon waver) are put into an oven for approximately 1 h at 200 °C. This process removes solvent (water and isopropanol) residues from the substrate surface. Additionally, oven baking reduces the background current (see section 4.5) when using glass substrates.

### 4.1.2 Formation of bottom electrodes

The bottom electrodes are deposited through a shadow mask on the substrates surface via a thermal evaporation process. As electrode material aluminum (Al) is used if not stated differently. Al is often used as electrode material due to its low deposition temperature, its chemical passivation feature and suppression of charge injection from the metal electrode [73]. The pressure in the evaporation chamber is controlled by a EDWARDS Active Gauge. At the start of the evaporation process the pressure is below $8 \times 10^{-6}$ mbar. The thickness and the deposition rate during thermal evaporation is displayed by a EDWARDS FTM7 unit. This unit is based on a quartz crystal and an oscillator unit. It calculates the film thickness and the deposition rate from a given material density and acoustic impedance.

### 4.1.3 P(VDF-TrFE) film preparation

P(VDF-TrFE) in a composition of 70/30 mol% bought from Piezotech ®, France is used. The P(VDF-TrFE) films are cast from solution (spin-coating) on the substrate and the bottom electrodes. Directly after spin-coating the polymer films are thermally annealed.

#### 4.1.3.1 Spin coating

Spin coating is a fast method to produce P(VDF-TrFE) films in a thickness range between 50 nm and several microns. A variation of the thickness of the polymer film can be achieved by controlling the spin speed and the concentration of polymer in solution [69]. Polymer power provided by Piezotech, France is dissolved in 2-butanone in a concentration range of 1 weight% to 6 weight%. The boiling point of 2-butanone is at 80 °C. A spin coater, KW-4A from Chemat Technology, in a speed range of 1000 to 5000krpm is used in this work. The polymer film adheres to the substrate and the bottom electrodes upon which it had been cast. The film is preferably smooth and dense (without holes) and exhibits low thickness variation. Spin-coating is an art: The solvent evaporates while spinning, when centrifugal forces and viscous forces are in the balance of forces [43].

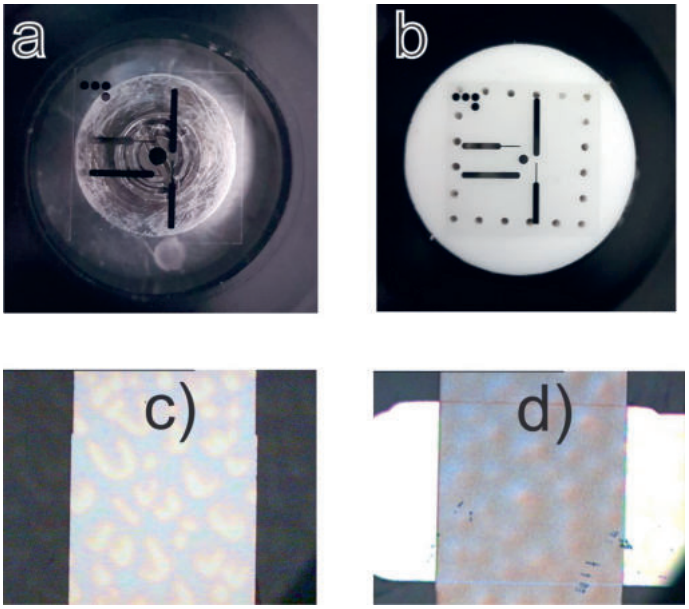


FIGURE 4.2: Glass substrate with aluminum bottom electrode tracks mounted on a) the standard chuck, b) the PTFE chuck. c) Inference pattern on the polymer film. d) Top electrode attached to the polymer film. The zone where electrode tracks intersect mark the active area.

The viscosity of the solution depends on various parameters and it is often a game of try and error to find a set of parameters leading to good films. In this work best films in terms of utmost homogeneous film thickness are produced using elevated environmental temperatures (≈ 50 °C), elevated solution temperatures (≈ 50 °C) and by preheating (≈ 50 °C) the substrate with bottom electrodes just before spin-coating. The film quality increases by a lot by using a PTFE chuck instead of the metal (standard) chuck (see photographs in FIG.4.2 a) and b)). Using the metal chuck to spin-cast polymer films results in co-polymer films with thickness variations, apparent in interference patterns with a shape alike the shape of the metal chuck. It is hypothesized that at positions at which the metal touches the substrate at the bottom side, the substrates top side is comparatively cooler than at other positions, which effectively results in polymer film thickness variations, since the viscosity of the solution depends on the temperature. These interference pattern disappear by using the PTFE chuck. Furthermore another kind

of interference pattern appear (FIG.4.2 c)), which can be spotted with the bare eye if the polymer film is tilted against the incident light. FIG.4.2 d) depicts a microscopic top view photograph of a polymer film with interference pattern packed between bottom- and top electrode. Hilly surface structures can clearly be spotted. All interference patterns almost disappear by using the PTFE chuck, by conducting spin-coating at elevated environmental temperatures and by using preheated solutions.
A recently better understood phenomenon is the formation of so called "pores" or "pin holes" [34, 62]. These holes in polymer films down to the substrate form during spin-coating and are a result of the difference in boiling point between the solvent and water residues in the solvent. The tendency of a solvent to absorb water is called hygroscopy. The formation of pin holes can be prevented by using a solvent with low hygroscopy and by processing spin-coating in water free atmosphere [62]. In the later stages of this work a glovebox was designed to make best spin coating conditions possible, like high environmental temperatures and a dry ($\approx$ 3% relative humidity) nitrogen-enriched environmental atmosphere. Besides, for samples produced with low water contamination the background current contributions in pyroelectric measurements are reduced to a great extent. Experimental results regarding the background current are presented in section 6.2.1. Additionally to the features provided by the glovebox, water contamination is especially prevented by using 2-butanone (which exhibits low hygroscopy) with extra low water content!
An easy and fast method for a first quality check directly after spin coating is an optic investigation with the bare eye: Dense polymer films (i.e. absence of pinholes) with uniform film thickness are transparent and do not exhibit interference patters. On the contrary, milky polymer films exhibit pin holes ([62, 73]) and polymer films with variable film thickness exhibit interference pattern.

#### 4.1.3.2 Thermal annealing

Directly after spin-coating the sample is placed on a heating plate for thermal annealing. Annealing proceeds also in the glovebox. In the annealing process the sample is heated from the environmental temperature of spin-coating to the maximum annealing temperature $T_{anneal}$, kept at this temperature for 2 h and is then cooled down to room temperature. A heating and cooling rate of 0.25 $\frac{^{\circ}\mathrm{C}}{\mathrm{min}}$ is used. It seems essential to use a low heating and cooling rate to obtain high quality polymer films. The temperature $T_{anneal}$ is above the Curie temperature $T_C$ but below the melting temperature $T_m$ of the co-polymer, if not stated differently. Thermal annealing results in evaporation of residual solvent, increased adhesion between co-polymer film and substrate and increased degree in crystallinity by transforming amorphous phase to the FE and DFE phase (see section 2.3.7.1). By variation of $T_{anneal}$ in the range $T_C < T_{anneal} < T_m$ the degree in crystallinity and the surface roughness can be altered (see section 2.3.9.2). Samples with varying degree in crystallinity are discussed in section 4.1.3.3. An important note: The annealing temperature $T_{anneal}$ is after sample preparation never exceeded.

#### 4.1.3.3 Co-polymer films with variable degree in crystallinity

In section 5.11 three samples with low, middle, and high crystallinity are compared. The samples with low, middle crystallinity differ only by $T_{anneal}$ with 116 °C and 133 °C, respectively. The increase in crystallinity with increasing $T_{anneal}$ is discussed in section 2.3.9. The high crystallinity sample exhibits an epitaxially grown film (see

section 4.1.6). Note, in the comparative study with different degrees in crystallinity all samples exhibit the same sample structure, which is presented FIG. 4.1 b).

### 4.1.4 Formation of top electrodes

After thermal annealing metal top electrodes are deposited by thermal evaporation through a shadow mask on the polymer surface. The evaporation process parameters correspond to those used for the bottom electrode formation (see section 4.1.2).

#### 4.1.4.1 Infrared-transparent top electrode

Here, the top electrode is made of two parts: an aluminum conduction ring and an infrared transparent ultra-thin aluminum layer. First, an aluminum conduction ring of around 100 nm thickness is thermally evaporated on the co-polymer surface. This conduction ring can be electrically connected via silver conductive paint and a strip of gold leaf without damaging the sample. Second, directly after the Al conduction ring an ultra-thin aluminum layer is evaporated on top of the co-polymer surface and the conduction ring. This ultra-thin aluminum layer functions simultaneously as electrode and as infrared (IR) window to the co-polymer film. 11 nm aluminum was tested out as trade-off satisfying sufficient electrical conductance and IR transparency. A sketch of the sample structure is shown in FIG. 4.1 c). The evaporation process for the ultra-thin Al electrode is conducted in extra low pressure $\approx 1 \times 10^{-6}$ mbar.

The functionality of the ultra-thin aluminum layer deteriorates by exposure to atmospheric humidity: Storing the sample in free air results in an increase of the electric resistance over time. Furthermore the ultra thin films losses its IR transparency after long time storage. It is hypothesized that aluminum hydroxide is formed over time. In the IR measurement chamber (which is kept dry (see section 7.2)) the sample remains functional.

### 4.1.5 Determination of the co-polymer film thickness and roughness

The surface roughness and the thickness of the polymer film are determined using an atomic force microscope (AFM, Veeco ® diInnova). The surface roughness (root mean square) is determined by the AFM software from a surface topography measurement. The co-polymer film thickness is determined via scratching a trench into the co-polymer film down to the substrate. The height difference between co-polymer surface and substrate determines the thickness of the co-polymer film.

### 4.1.6 Sample with epitaxially grown P(VDF-TrFE) film

These samples are provided by the group of Professor Dr. Guodong Zhu from the Fudan University, China. The sample structure is shown in FIG. 4.1 b). The P(VDF-TrFE) films are processed under high pressure and epitaxially grow on removable PTFE templates [117]. These co-polymer films are characterized by a high degree in crystallinity. FIG. 4.3 compares X-ray diffraction spectra of two co-polymer films (on a silicon substrate): One co-polymer film is prepared as explained in section 4.1.3 and using $T_{anneal} = 133\,^{\circ}\mathrm{C}$, the other sample exhibits an epitaxially grown co-polymer film as mentioned above. The peak at $2\Theta$ is assigned to the (110) and (200) orientations which are attributed to the ferroelectric all-trans phase (see section 2.3.7).

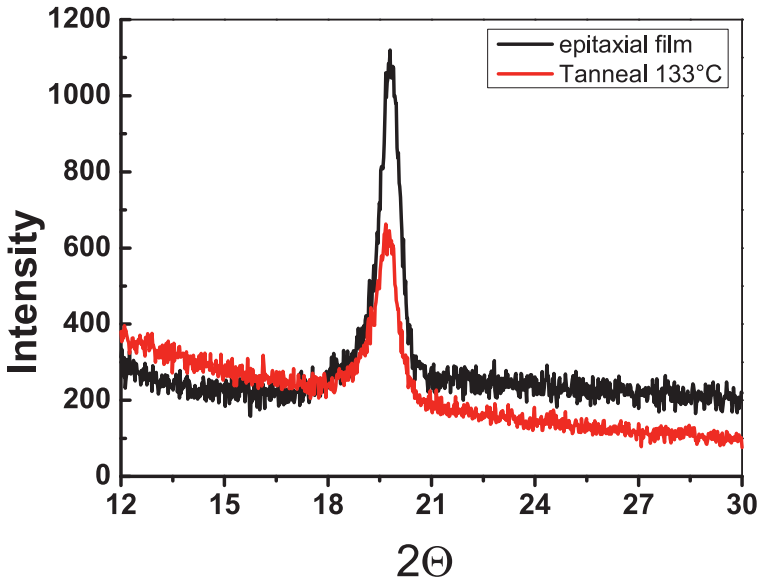


FIGURE 4.3: Comparison of XRD spectra belonging to an epitaxial grown co-polymer film and a co-polymer film which has been annealed at $T_{anneal} = 133°C$: The degree in crystallinity is higher for the epitaxial grown film. Reproduced from [87], with the permission of AIP Publishing.

## 4.2 Measurement setup

### 4.2.1 Measurement environment

If not stated differently, all electrical measurements are conducted in an electrically shielded measurement cell made of steel and in low pressure conditions (pressure $\approx 1 \times 10^{-2}$ mbar).

### 4.2.2 Electrical contacting

The sample is connected via spring mounted metal needles, which are attached at the forefront of so called manipulators. If temperature dependent measurements are conducted, the electrical contact might disrupt due to different extent of thermal expansion/contraction of various involved components. A weak point, even if spring mounted, is the connection between the electrode tracks and the contacting needles. For that reason longish pieces are cut from gold leaf and glued with silver conducting paint on one side to an electrode track and on other other side to the contacting needle to bridge this weak spot. A photograph of an electrically connected sample ready for testing is shown in FIG. 4.4.

### 4.2.3 Polarization measurement

The polarization is measured with an institute-made Sawyer-Tower-Setup [69]. Two different data acquisition cards with different time resolution and different input impedance make this setup able to monitor fast and slow polarization and depolarization processes in one run.

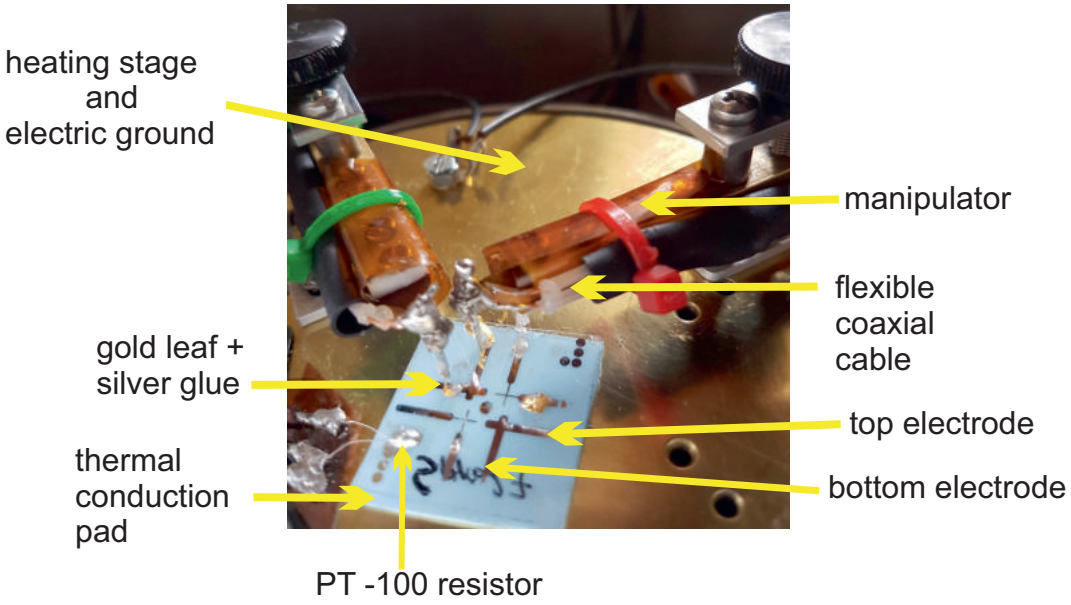


FIGURE 4.4: Electrically contacted sample in measurement chamber.

### 4.2.4 Current measurement

Several devices are used to monitor currents. In the short time range ( $< 10^{-7}$ s) the current is calculated from the voltage drop across a known resistor. In the intermediate time range ($10^{-7}$ s $< t <$ 1 s) the before mentioned method, a current amplifier (Keithley 428 Current Amplifier) or the Sawyer-Tower-Setup (see section 4.2.3) is used. When using the Sawyer-Tower-Setup, the current density is determined via differentiation of the polarization respective to time. For times above 1 s mostly an electrometer is used (Keithley 6514 System Electrometer).

### 4.2.5 Permittivity measurement

Real- and imaginary part of the permittivity are determined from capacitance -, tan $\delta$ measurements using a 4 point LCR - meter (Agilent 4294A). The maximum amplitude applied in permittivity measurements is between 0.1 V to 0.5 V[1].

## 4.3 Field signals applied in imprint measurements

Imprint affects several material properties. As will be shown in section 5.1. Before the measurement of imprint effects, the sample is de-aged by switching, see section 5.2.2 [2].

### 4.3.1 Field signals and determination of $\tau$ and $E_c$

The field signals applied to determine the coercive fields $E_c$ and the ferroelectric polarization switching times $\tau$ as functions of the waiting time are depicted in FIG. 4.5 a) and b), respectively. First the sample is de-aged by switching (see section 5.2.2). The subsequent measurement signal consists of triangular or rectangular

[1] here: V = Volt

[2] The exception are pyroelectric- and related measurements presented in chapter 6, where the samples are initially de-aged above $T_C$.

pulses with increasing waiting interval in between. The time interval between the pulses is denoted as the waiting time $t_w$, which increases subsequently with the law: $(t_w)_{n+1} = 2^n(t_w)_n$, where n is the number of the pulse in the pulse sequence. The duration in the inverted ferroelectric polarization state is kept short ($< 5$ ms) to avoid de-aging. The impact of de-aging within the measurement sequence was tested out and was found to be negligible (not shown). The ferroelectric polarization switching time $\tau$ is determined from a best fit to a stretched exponential function (see section 2.3.10) if not stated differently. The coercive fields (positive $E_c$ and negative $E_c$) are determined from symmetrized hysteresis loops: The measured hysteresis is shifted along the $D$ axis, so that $|D(E_p)| = |D(E_n)|$, where $D$ is the dielectric displacement and $E_p$ and $E_n$ are the maximum electric field amplitudes applied in positive and negative direction, respectively.

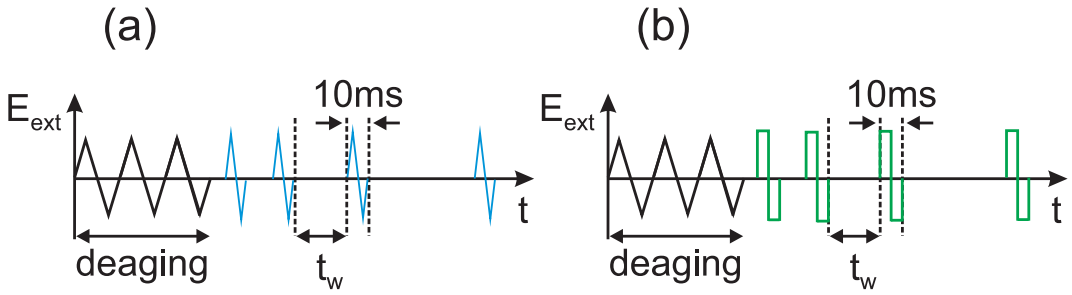


FIGURE 4.5: Electric field signals applied to the sample to determine a) coercive fields $E_c$ and b) ferroelectric switching times $\tau$ as a function of the waiting time $t_w$. Reproduced from [88], with the permission of AIP Publishing.

### 4.3.2 Field signals to determine $\varepsilon$ and $j_{rel}$

After de-aging by switching, the sample is in a remanent polarization state. The measurement of the permittivity $\varepsilon$ proceeds while waiting in the remanent polarization state.
After de-aging by switching an electric field pulse is applied to switch the ferroelectric polarization state. After switching off the field the depolarization current density $j_{depol}$ is measured in the outer short circuit. The imprinting current density $j_{rel}$ is determined from $j_{depol}$, for details see section 5.9. The system remains during the complete measurement period in a remanent polarization state.

### 4.3.3 Definition of the experimental waiting time $t_w$

The waiting time $t_w$ stated when presenting experimental results is defined as the time elapsed since last ferroelectric polarization reversal [3]. Note, while measuring the $\tau$ and $E_C$ the system changes the polarization state in the measurement sequence (see section 4.3.1). In contrast during the measurement of $\varepsilon$ and $j_{rel}$ the polarization state is never changed (see section 4.3.2).

## 4.4 Temperature measurement

In all experiments the temperature is continuously monitored by two PT-100 sensors (HERAEUS®). One sensor measures the temperature of the heating/cooling stage.

[3] See section 3.2.1 to compare with definition of $t_w$ in the imprint models.

The other is glued (Arctic® thermal adhesive glue) directly on top of the polymer film (see FIG. 4.4). In FIG. 4.6 a) the temperature difference $\Delta T$ between co-polymer surface and heating/cooling stage is depicted. To FIG. 4.6 a) corresponds the temperature loop measured at the co-polymer surface shown in FIG. 4.6 b). The absolute value of temperature difference $|\Delta T|$ is at max in the beginning of the heating- and in the beginning of the cooling process and can there be as much as 2.2 °C (see FIG. 4.6 a)) for a heating/cooling rate of 3 °C min$^{-1}$, which is the maximum rate used in the work. This difference in temperature limits the temperature measurement accuracy. Additionally, that indicates that a small temperature gradient is present in the co-polymer film when performing temperatures cycles. All temperature information stated in the results section is measured at the polymer surface, if not stated differently.

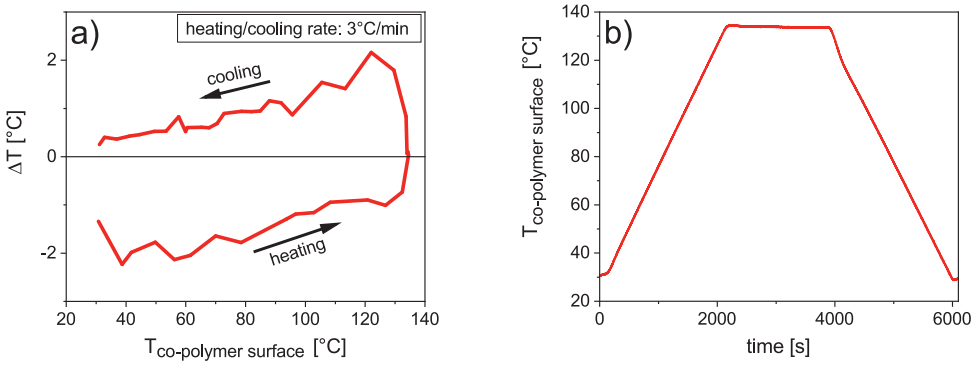


FIGURE 4.6: a) $\Delta T$ = Temperature difference between the co-polymer surface and the heating stage. b) Temperature loop with heating/cooling rate of 3 °C min$^{-1}$; measured at the co-polymer surface.

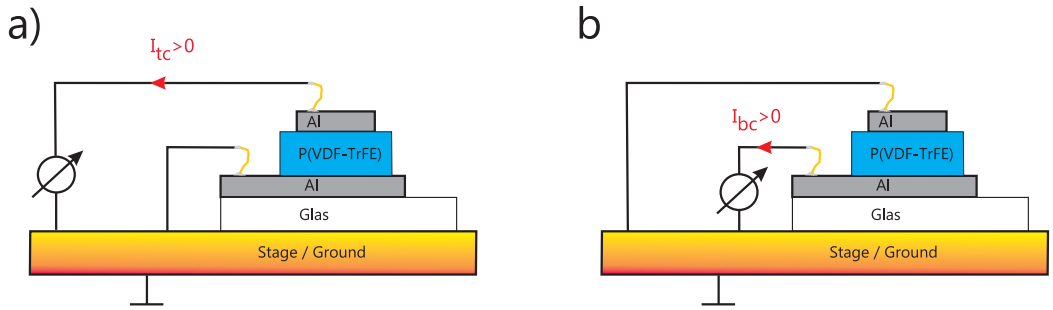


FIGURE 4.7: Pyroelectric measurement setup: a) top connection (tc). b) bottom connection (bc).

## 4.5 Current measurement while thermal cycling

The heating/cooling cycles in chapter 6 are performed with constant rate. FIG. 4.6 b) depicts an exemplary temperature loop. In the early stages of conducting measurements during such cycles, the sample (Al/P(VDF-TrFE)/Al/Glas) was glued with thermal paste (Amasan T12, produced by Juergen Armack GmbH) directly on the heating/cooling stage. Later, a stack of following components was formed: starting with sample at the top, thermal pad (Arctic ® ACTPD00004A) with thickness 1 mm, $Al_2O_3$ platelet with thickness 1 mm, thermal paste which makes contact with the stage (see FIG. 4.4). Both, thermal pad and $Al_2O_3$ platelet exhibit low electric- but high thermal conductivity. This stack guarantees uniform heat transfer between stage and sample.
The heating/cooling stage is made of brass and functions also as electric ground (see FIG. 4.4). The stage is electrically heated and cooled by pouring cool gaseous nitrogen into the tubular system within the stage.
**Background (bg) current:** Since not all currents in pyroelectric measurements could be assigned to an underlying physical process, various origins of current sources contributing to the short circuit current were explored. A sketch of the measurement setup is illustrated in FIG. 4.7. The sample is either connected in top-connection (tc) as shown in FIG. 4.7 a) or in bottom connection (bc) as shown in FIG. 4.7 b). If not stated differently the measurement circuit consists of the sample which is connected in series with an electrometer. Let's assume a current to originate from charge movements in the polymer to be positive if measured in tc. The current which originates from the same charge movements is then negative if measured in bc. In contrast, a current which originates from charge movements outside the polymer (e.g. charge movements in the glass-substrate, the thermal pad and the top electrode-atmosphere interface) which is positive in tc is also positive in bc [4]. Consequently by conducting measurements in tc and bc one can differentiate current sources from outside and inside the polymer.
Experimentally it is found that a certain current contribution originates from charge movements the glass substrate. Note, other sources to the bg current are discussed in section 4.1.3.1.

[4]Currents, which origin from charge movements in the cable isolation or other parts of the connection setup cannot be differentiated with this method from the current which originates from the co-polymer film. Such contributions were however never observed in the numerous measurements conducted.

# Chapter 5

# Experimental Results and Discussion I: Imprinteffects

## 5.1 Imprint effects and their characteristics

Imprinting affects several material properties, as will be presented in the following. Probably most prominent for imprinting is the time dependent shift of the polarization hysteresis along the electric field axis. This shift is symmetric, as shown in FIG. 5.1 a) and b): Waiting in $-P_{rem}$ results in a shift of the hysteresis to the right and waiting in $+P_{rem}$ results in a shift of the hysteresis to the left. The values of the coercive field that is passed first (i.e. $E_c^+$ and $E_c^-$ in FIG. 5.1 a) and b), respectively), lie on a straight line, when plotted against $\log(t_w)$, as shown in FIG. 5.1 c). $E_c$ that is passed second changes only little with $t_w$, which is discussed in section 5.2.

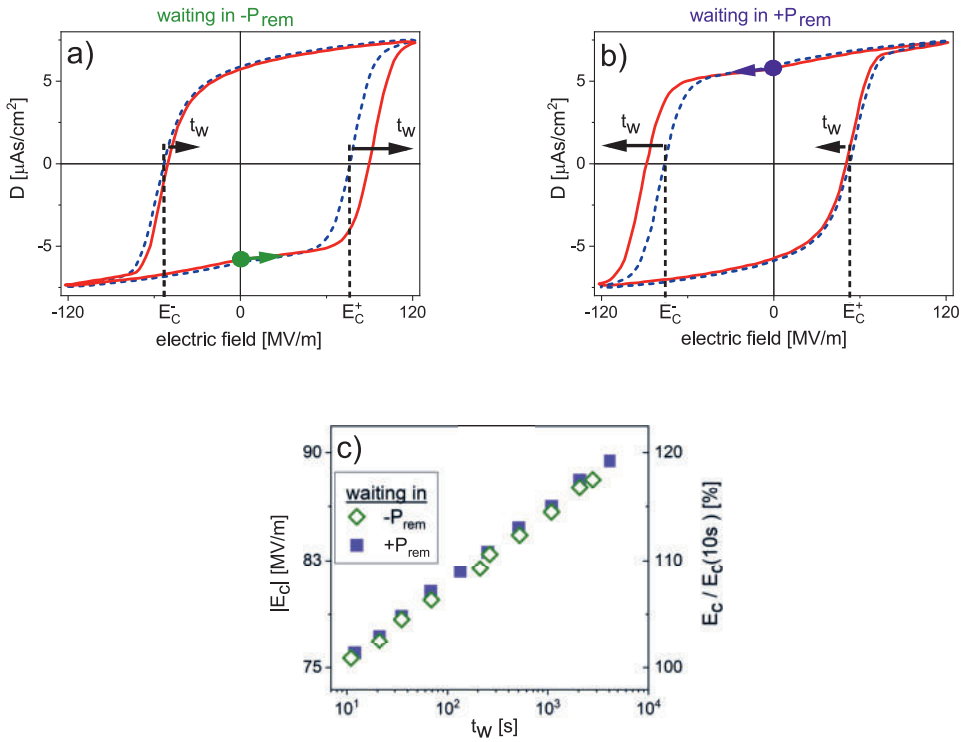


FIGURE 5.1: Effect of imprinting; shift of the polarization hysteresis with $t_w$: a) waiting in $-P_{rem}$. b) waiting in $+P_{rem}$. c) Coercive field, that is passed first, as a function of the waiting time ($t_w$). Reproduced from [87], with the permission of AIP Publishing.

Its plausible that an increase of the coercive field $E_c$ implies an increase in the ferroelectric switching time $\tau$. In contrast to $E_c$, the values of $\log(\tau)$ lie on a straight line as a function of $\log(t_w)$ [41], see also FIG.5.12.
Furthermore, the permittivity $\varepsilon$ and the remanent polarization $P_{rem}$ are also affected by imprinting, which becomes apparent by taking a closer look at FIG. 5.1 a) and b):

- the slope close to the starting point of the loops becomes the flatter, the longer the waiting time. For small electric field signal amplitudes applied by a LCR meter, the system remains close to $P_{rem}$. The permittivity in the remanent polarization state can be expressed as

$$\varepsilon(t_w) = \frac{dD}{dE_{ext}}\Big|_{\approx P_{rem}} \tag{5.1}$$

- the hysteresis shrinks in vertical direction with increasing $t_w$ (see FIG. 5.1 a) and b)). But more conclusive is the observation that the imprint current density $j_{rel}(t_w)$ is registered during $t_w$ in the short circuit (see section 5.9.1). From a technical point of view, more important is the related decay of the remanent polarization during $t_w$:

$$P_{rem}(t_w) = P_{rem}\Big|_{t=t_0} - \int_{t_0}^{t_w} j_{rel}\, dt \tag{5.2}$$

The effects of imprinting are altogether found to be dependent $\log(t_w)$:

$$\left.\begin{array}{ll} i=1: & E_c \\ i=2: & \log(\tau) \\ i=3: & P_{rem} \\ i=4: & \varepsilon \end{array}\right\} = a_i + b_i \cdot \log\left(\frac{t_w}{t_0}\right) \tag{5.3}$$

$a_i$ and $b_i$ in equation 5.3 are constants for the value of the material property at zero imprint ($t < t_0$) and the speed of which an imprint effect progresses, respectively. $b_i$ is positive for i=1 and i=2 and negative for i=3 and i=4. Consequently, $\tau(t_w)$ and $E_c(t_w)$ increase and $P_{rem}(t_w)$ and $\varepsilon(t_w)$ decrease with increasing $t_w$. The time $t_0$ is a normalization constant, which marks the begin of imprinting as explained in section 3.3.

Characteristic for an imprint effect is:

- a logarithmic dependence on $t_w$, as presented in equation (5.3)
- a symmetric behavior regarding waiting in $+P_{rem}$ and $-P_{rem}$ (see FIG. 5.1)
- to evolve independent of the thickness of the co-polymer film, as discussed in section 5.3
- a dependence on the co-polymers crystallinity (see section 5.11)
- to evolve over a huge time span (see section 5.8)

## 5.2 De-aging

De-aging is a procedure with the aim to delete imprint. In this work two kinds of de-aging procedures are used, termed "de-aging by switching" and "de-aging above $T_C$". The latter procedure is more effective, but also more laborious and was discovered in a later stage of this work. If not stated otherwise, before an imprint experiment [1] the sample is always de-aged by switching, whereas in chapter 6 the samples are initially de-aged above $T_C$.

### 5.2.1 De-aging in the view of the New Imprint Model

In the view of the New Imprint Model presented in section 3.3, de-aging can be understood as the process to randomize the orientations of rd. A description of both de-aging procedures on behalf of the New Imprint Model is given in the following:

- de-aging by switching: switching $P_{fe-cryst}$ is connected to the reversal of the stray field of $P_{fe-cryst}$ and thus both, the applied field and the stray field alternate and both act on the rd. Thereby, the rd are switched back and forth, which diminishes their alignment.
- de-aging above $T_C$: $P_{fe-cryst}$ equals zero, at temperatures above $T_C$. Consequently, the stray field of $P_{fe-cryst}$ is zero also. In this "zero" field environment the orientations of the rd randomize due to the disordering force of the temperature.

### 5.2.2 De-aging by switching

De-aging can be accomplished by subsequent ferroelectric polarization switching processes [41]. Such a de-aging process is depicted in FIG. 5.2 a): Initially the sample was left for $t_w = 24h$ in $-P_{rem}$. Then, the ferroelectric polarization hysteresis is continuously traversed with a frequency of the applied field of 10 Hz. The legend in FIG. 5.2 a) states the cycle of the loop. FIG. 5.2 b) depicts the coercive fields that are passed first (i.e. here $+E_c$) in a loop as a function of the duration of the de-aging process, whereas the parameter is the frequency of the continuous triangular electric field signal applied. Note, the coercive fields that are passed second in a loop change only slightly as can be seen in FIG. 5.2 a). This can be understood by considering that rd with long (compared to the amplied frequency) relaxation times tend to remain in the imprinted position while those with short relaxation times are switched every time when travering the loop. In FIG. 5.2 b), $E_c$ that is passed first enters a plateau after around five cycles at a frequency of 0.01Hz. Reconsidering that numerous switching events affect the imprint rate [2] [124], this plateau seems the best compromise between fast and gentle de-aging.
"De-aging by switching" - procedure: The ferroelectric polarization hysteresis loop is traversed five times with a frequency of the applied triangular field of 0.01 Hz.

### 5.2.3 De-aging above $T_C$

De-aging can be accomplished by heating the sample to a sufficiently high temperature. It is believed that the temperature $T_{dis}$ (subscript means disorientation) above

[1] In an imprint experiment, effects of imprint are measured as a function of $t_w$. Effects of imprint are listed in equation (5.3)

[2] $b_i$ in equation (5.3)

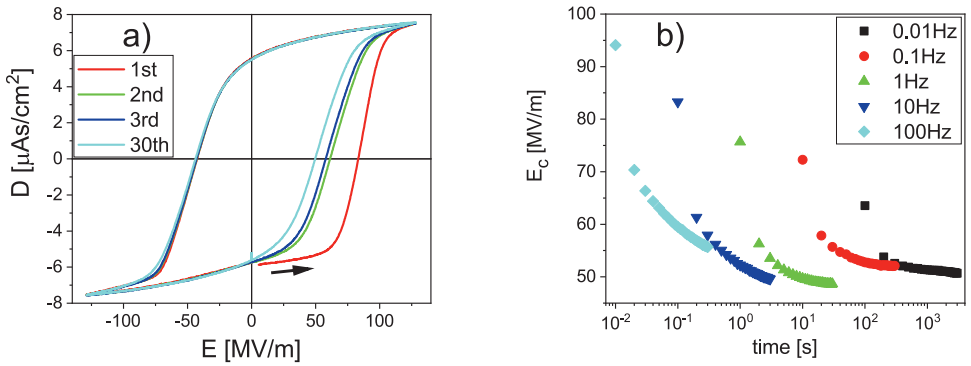


FIGURE 5.2: De-aging by switching. a) Frequency of the applied field signal is 10 Hz. b) $E_c$ that is passed first as a function of the de-aging time at various frequencies of the applied field. Sample thickness: 260nm. b) is reproduced from [88], with the permission of AIP Publishing.

which the sample de-ages completely [3] is approximately identical to $T_C$. In the high temperature range there are some current contributions which could not be assigned to the underlying physical process , so de-aging above $T_C$

"De-aging above $T_C$" - procedure: Heating the short circuited sample above the Curie Temperature $T_C$, keeping it there for at least 10 min and cooling it to the temperature at which a measurement is in the following conducted. If not mentioned differently a heating and cooling rate of 3 °C min$^{-1}$ is used.

After de-aging above $T_C$ the ferroelectric polarization vector in a ferroelectric crystallite ($\mathbf{P}_{fe-cryst}$) is assumed to point in a random direction at room temperature, since the pyroelectric response of an un-poled sample at room temperature is weak (see section 6.2) compared to that of a poled sample (see section 6.6 but also [103]). At high temperatures imprint builds up comparatively fast [4]. The imprint situation after de-aging above $T_C$ and subsequent cooling to 30 °C might be as illustrated in FIG. 5.3 b). rd in close vicinity to the ferroelectric crystallites are aligned with the stray fields of $\mathbf{P}_{fe-cryst}$. The stray fields of $\mathbf{P}_{fe-cryst}$ further away from the crystallites are statistically canceled out and there the rd point in a random direction. FIG. 5.3 a) depicts two poling processes at 30 °C. In the course of poling the ferroelectric polarization hysteresis loop is traversed in total three times. One poling process is conducted directly after de-aging above $T_C$ (solid line), the other after de-aging above $T_C$ and subsequent waiting for around 24 h at 30 °C (dashed line). As can be seen, the field strength necessary to pole the sample is in both cases very high, thus much imprint is initially present. The effect of waiting 24 h is further a aggravation of the poling process. The loops of the second and the third cycle are symmetric with regard to the electric field axis. This symmetry indicates that the rd point on the large scale in random direction, after de-aging above $T_C$ and subsequent poling.

Note, thematically related are the experimental results presented in section 6.3.

[3] De-aging by heating is accompanied by short circuit currents, see section 6.5)

[4] The temperature dependence of relaxation times is in detail discussed in section 6.9.

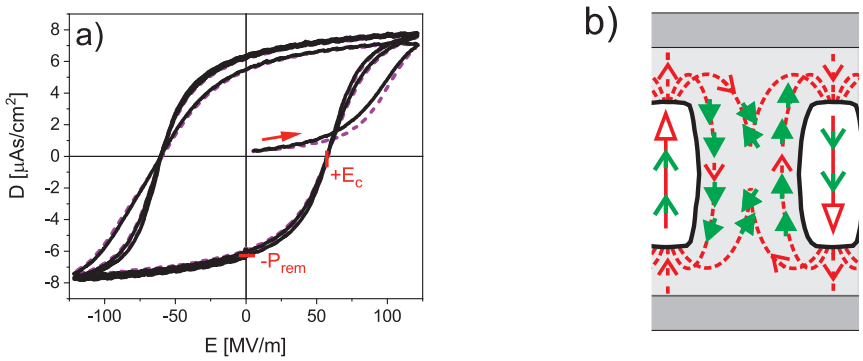


FIGURE 5.3: a) Poling a sample at 30 °C after de-aging above $T_C$: directly after de-aging (solid line) and after de-aging and waiting for 24 h at 30 °C. b) The illustration is based on the New Imprint Model (see also section 3.3). Imprint situation at 30 °C after de-aging above $T_C$.

### 5.2.4 Comparing the effectiveness of both de-aging processes

FIG. 5.4 b) compares $E_c(t_w)$ after de-aging by switching with $E_c(t_w)$ after de-aging above $T_C$. In both cases an electric field pulse of 120 MV m$^{-1}$ amplitude and 10 s duration was applied between de-aging and the measurement of $E_c(t_w)$ (see FIG. 5.4 a)). This field pulse exceeds the high field necessary to pole an un-poled sample after cooling from above $T_C$ (see section 5.2.3). For the reason of comparability after de-aging by switching the field pulse is applied also. According to FIG. 5.4 b) de-aging above $T_C$ is more effective than de-aging by switching, because $+E_c(t_w)$ is especially at short $t_w$ lower after de-aging above $T_C$ compared to after de-aging by switching.

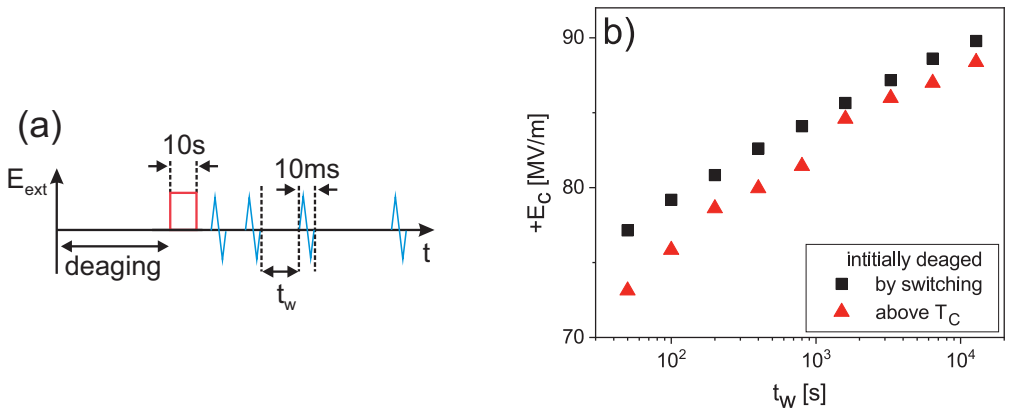


FIGURE 5.4: Comparison of "de-aging by switching" with "de-aging above $T_C$". a) Field signal applied. b) Coercive field as a function of the waiting time, measured after de-aging.

## 5.3 Polymer film thickness variation

Polymer films covered by aluminum electrodes below a critical thickness of 100 nm are affected by thin films effects [71]. Below 100 nm, the ferroelectric polarization switching time $\tau$ [5] and the coercive field $E_c$ increase and the permittivity $\varepsilon$ and remanent polarization $P_{rem}$ decrease with decreasing polymer film thickness. The following thickness independent expressions are introduced to compare the effects of imprint over a wide thickness range:

$$V_c^{norm}(t_w) = \frac{V_c(t_w)}{V_c(10s)} = \frac{E_c(t_w)}{E_c(10s)} \qquad C^{norm}(t_w) = \frac{C(t_w)}{C(100s)} = \frac{\varepsilon(t_w)}{\varepsilon(100s)} \tag{5.4}$$

FIG. 5.5 and FIG. 5.6 depict effects of imprint with the polymer film thickness as parameter. As can been seen the impact of imprinting on material properties is independent of the polymer film thickness. The Dead Layer Model presented in section 3.2.3 is not consistent with this experimental finding as discussed in detail in section 5.6.

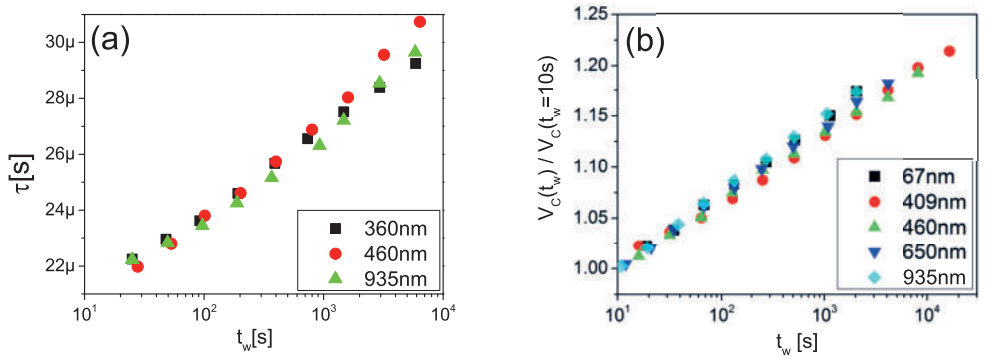


FIGURE 5.5: Evolution of imprint for various co-polymer thicknesses: (a) $\tau(t_w)$. (b) $V_c^{norm}(t_w)$. Reproduced from [88], with the permission of AIP Publishing.

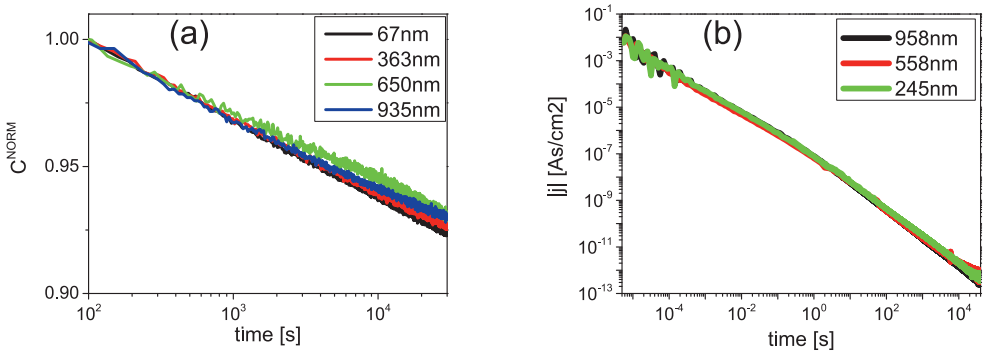


FIGURE 5.6: Evolution of imprint for various co-polymer thicknesses [6]: (a) $C^{norm}(t_w)$ at a frequency of 10 kHz. (b) depolarization currents after a field step of 130 MV m$^{-1}$ and 10s duration. Note, for $j(t > 10s)$ the current density is solely related to imprinting for details see section 5.9. Reproduced from [88], with the permission of AIP Publishing.

[5] $\tau$ is here defined as the duration since application of the field pulse and the point in time at which the amount of switched polarization reaches 75% of the saturation polarization. For details see [88].

[6] The time in a) equals the waiting time as defined in section 4.3.3. In b) the relation between the time and $t_w$ is more complex, for details see section 5.9.

## 5.4 Electric field offset during the $t_w$

Applying an external electric field in the direction of the ferroelectric polarization vector during the waiting time $t_w$, results in a slowdown of the imprinting process. This is shown in FIG. 5.7 for the coercive field $E_c'$ and the ferroelectric switching time $\tau$. FIG. 5.7 a) and b) depict the electric field signals applied in this experiment for measuring $E_c'(t_w)$ and $\tau(t_w)$, respectively. $E_c'$ denotes the electric field at the current maximum when passing through the hysteresis loop. The switching times $\tau$ in FIG. 5.7 b) were determined by a best fit of a stretched exponential function to the polarization transient (see equation (2.7)).

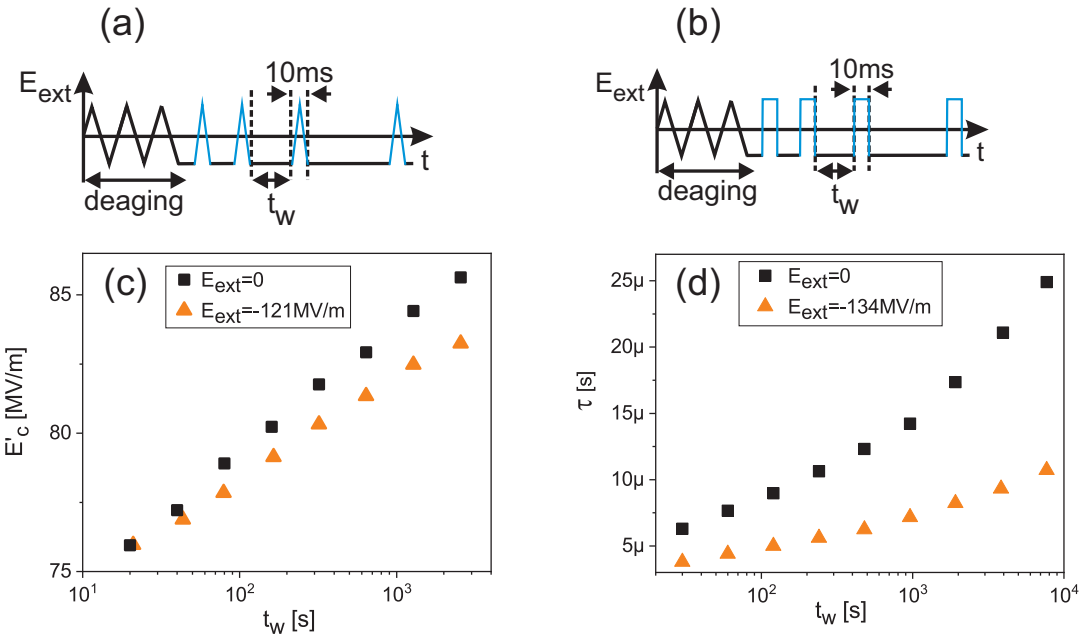


FIGURE 5.7: Electric field offset during $t_w$: (a) and (b) electric field signals for measuring $E_c'(t_w)$ and $\tau(t_w)$ with field offset, respectively. (c) and (d) $E_c'(t_w)$ and $\tau(t_w)$, respectively, with and without field offset. (c) is reproduced from [87], with the permission of AIP Publishing.

FIG. 5.8 depicts the New Imprint Model for the scenario with an field offset applied during $t_w$. As reasoned also in section 5.9 it can be assumed that most of the rd are located in the interstitial space between the crystallites. In the interstitial space, the stray electric fields of $P_{fe-cryst}$ and $E_{ext}$ point in opposite direction. Thus, $E_{ext}$ hinders the rd from aligning in the stray field's direction. As a consequence, $E_{imprint}$ is decreased in the case with field offset, compared to the case without field offset. Other imprinting models as those presented in section 3.2 don't provide such an easy interpretation of this experimental finding, or predict even a contradictive behavior, as discussed in detail in section 5.6.3.

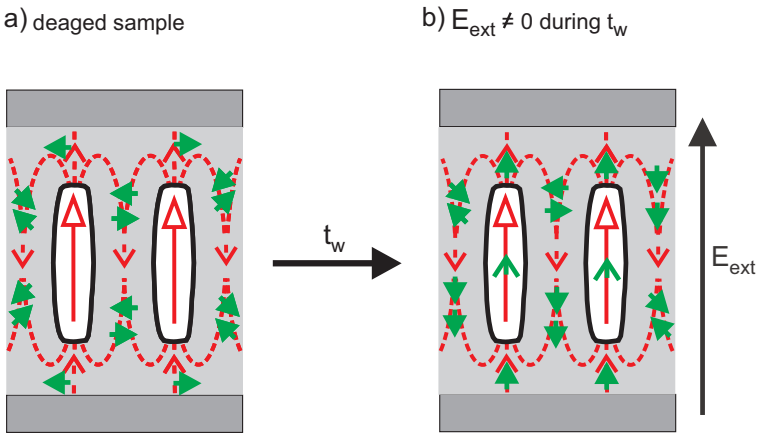


FIGURE 5.8: New Imprint Model (see section 3.3) if during $t_w$ an external electric field $E_{ext}$ is applied. (a) No imprint. (b) Imprinted sample. Reproduced from [87], with the permission of AIP Publishing.

## 5.5 Temperature dependence of $E_c(t_w)$

FIG. 5.9 depicts $E_c(t_w)$ measured at different temperatures. The initial de-aging process, the imprinting process (waiting for a duration $t_w$) and the measurement of the coercive field take place at the stated temperature. In FIG. 5.9 $E_c(t_w)$ evolves in the whole temperature range investigated continuously according to the law stated in equation (5.3). Additionally, it seems that the speed of which imprinting proceeds doesn't depend much on the temperature. A corresponding experimental result is found for the ferroelectric switching time [124]. Still, waiting for a certain time period $t_w$ at a high temperature results in more imprint than waiting the same time period at a cooler temperature, because the rd-relaxation times generally decrease with increasing temperature (for details see section 6.9). It needs to be stressed that measuring the coercive field includes partial de-aging by switching. The experimental results shown in FIG. 5.9 is again discussed in section 6.10 in the light of new findings. In a future investigation one could monitor $\varepsilon(t_w)$ to determine the temperature dependence of imprinting, since the measurement of $\varepsilon(t_w)$ doesn't include disturbing the imprinting process by partial de-aging.

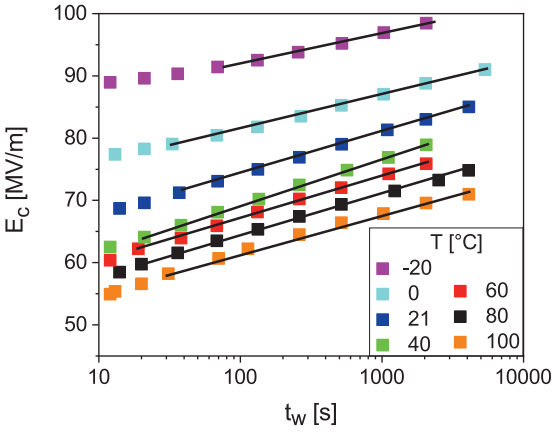


FIGURE 5.9: Coercive field (that is passed first in the hysteresis loop) as a function of the waiting time $t_w$ at various temperatures. Lines are guides for the eye.

## 5.6 Revisiting the Dead Layer Model

The Dead Layer Model is explained in section 3.2.3. In the following, the Dead Layer Model is revised in the light of present experimental findings.

### 5.6.1 Thickness independence of $C^{norm}(t_w)$:

Let's assume the imprint mechanism takes place in an electrode adjacent non-ferroelectric layer. Lets consider the sample as two capacitors in series as illustrated in section 3.2.3. One capacitor represents the ferroelectric bulk and the other the dead layer in which the imprint mechanism takes place. $E_{bu}$, $E_{dl}$, $P_{bu}$ [7], $P_{dl}$, $\varepsilon_{bu}$, $\varepsilon_{dl}$, $d_{bu}$ and $d_{dl}$ are the electric fields, the polarizations, the permittivities, and the thicknesses of/in the bulk (bu) and of/in the dead layer (dl), respectively. Then the two capacitors in series yield for the normalized capacitance

$$C^{norm}(t_w) = \left(\frac{d_{dl}}{\varepsilon_{dl}(100s)} + \frac{d_{bu}}{\varepsilon_{bu}(100s)}\right)\left(\frac{d_{dl}}{\varepsilon_{dl}(t_w)} + \frac{d_{bu}}{\varepsilon_{bu}(t_w)}\right)^{-1} \tag{5.5}$$

Derivation of $C^{norm}$ respective to the bulk thickness is non zero:

$$\frac{\partial C^{norm}}{\partial d_{bu}} \neq 0 \tag{5.6}$$

Experimentally, $C^{norm}(t_w)$ is however found to be independent of $d_{bu}$. Thus, the prediction of the Dead Layer Model doesn't comply with the experimental finding.

### 5.6.2 Thickness independence of $j(t_w)$:

The two capacitors in series are now assumed to remain in short circuit condition during the waiting time ($t_w$). The imprint process is again assumed to take place in

[7] $P_{bu} = P_{fe}$

the dead layer, thus $\varepsilon_{dl}(t_w)$ and $P_{dl}(t_w)$ [8] are dependent on $t_w$. The continuity conditions for the dielectric displacement D in equation (5.7) and the Maxwell equation (5.8) yield equation (5.9).

$$D(t_w) = P_{dl}(t_w) + \varepsilon_{dl}(t_w)E_{dl}(t_w) = P_{bu} + \varepsilon_{bu}E_{bu}(t_w) \tag{5.7}$$

$$-E_{dl}(t_w)d_{dl} = E_{bu}(t_w)d_{bu} \tag{5.8}$$

$$D(t_w) = P_{bu} + (P_{dl}(t_w) - P_{bu})\left(\frac{\varepsilon_{dl}(t_w)}{\varepsilon_{bu}}\frac{d_{bu}}{d_{dl}} + 1\right)^{-1} \tag{5.9}$$

Differentiating equation (5.9) respective to time yields the imprint current density: $j(t_w)$[9]$= \frac{dD}{dt_w}$, presented in equation (5.10). Note, $\dot{\varepsilon} = \frac{d\varepsilon}{dt_w}$ and $\dot{P} = \frac{dP}{dt_w}$ .

$$j(t_w) = \dot{\varepsilon}_{dl}(t_w)\frac{d_{bu}}{d_{dl}\varepsilon_{bu}}\left(\frac{\varepsilon_{dl}(t_w)}{\varepsilon_{bu}}\frac{d_{bu}}{d_{dl}} + 1\right)^{-2}(P_{dl}(t_w) - P_{bu}) + \left(\frac{\varepsilon_{dl}(t_w)}{\epsilon_{bu}}\frac{d_{bu}}{d_{dl}} + 1\right)^{-1}\dot{P}_{dl}(t_w) \tag{5.10}$$

In the present sample structure an electrode adjacent $Al_2O_3$ layer of around 4 nm thickness [98]) is known to exist, which is held responsible to some extent for thin film effects in P(VDF-TrFE) [69]. Let the dead layer be 4 nm thick, thus $d_{sl} << d_{bu}$ and lets additionally assume that $\varepsilon_{dl}(t_w)$ and $\varepsilon_{bu}$ are of the same order of magnitude, then "+1" in equation (5.10) can be neglected, which yields:

$$j(t_w) \approx \frac{d_{dl}}{d_{bu}}\frac{\varepsilon_{bu}}{\varepsilon_{dl}(t_w)}\left(\frac{\dot{\varepsilon}_{dl}(t_w)}{\varepsilon_{dl}(t_w)}(P_{dl}(t_w) - P_{bu}) + \dot{P}_{dl}(t_w)\right) \tag{5.11}$$

The ratio of two imprint current densities originating from samples with different thicknesses $d^{(1)} = d_{dl} + d_{bu}^{(1)}$ and $d^{(2)} = d_{dl} + d_{bu}^{(2)}$ is:

$$\frac{j^{(1)}(t_w)}{j^{(2)}(t_w)} \approx \frac{d_{bu}^{(2)}}{d_{bu}^{(1)}} \tag{5.12}$$

The ratio of the current densities originating from polymer thicknesses of 245 nm and 958 nm, respectively, is in FIG. 5.6 b) over the full time range always below 1.5, whereas equation (5.12) predicts 958nm/245nm = 3.9. Consequently, the origin of the current in FIG. 5.6 b), especially for $t > 10s$, cannot be explained with the Dead Layer Model.
In conclusion, the Dead Layer Model predicts thickness dependent $C^{norm}(t_w)$ and $j_{rel}(t_w)$, which is in contradiction to the experimental finding.

### 5.6.3 Field offset experiment

The Dead Layer Model with field offset ($E_{ext}$) is outlined in FIG. 5.10. The model predicts a speed up of the imprint process when applying $E_{ext}$, because $E_{dl}$ and $E_{ext}$ point into the same direction. But the opposite is found in the experiment, where imprinting is slowed down by the field offset (see section 5.4).

In conclusion, the Dead Layer Model predicts a thickness dependent $C_{norm}$, a thickness dependent imprinting current and a speed up of imprint due to the external field offset. All these predictions are in contradiction to the experimental findings.

[8] $P_{dl}$ equals the injected electron charge density.
[9] $j(t_w) = j_{rel}(t_w)$

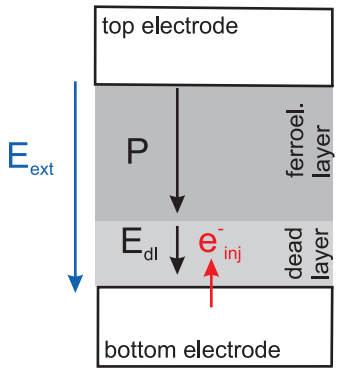


FIGURE 5.10: Dead Layer Model with $E_{ext}$ applied during $t_w$.

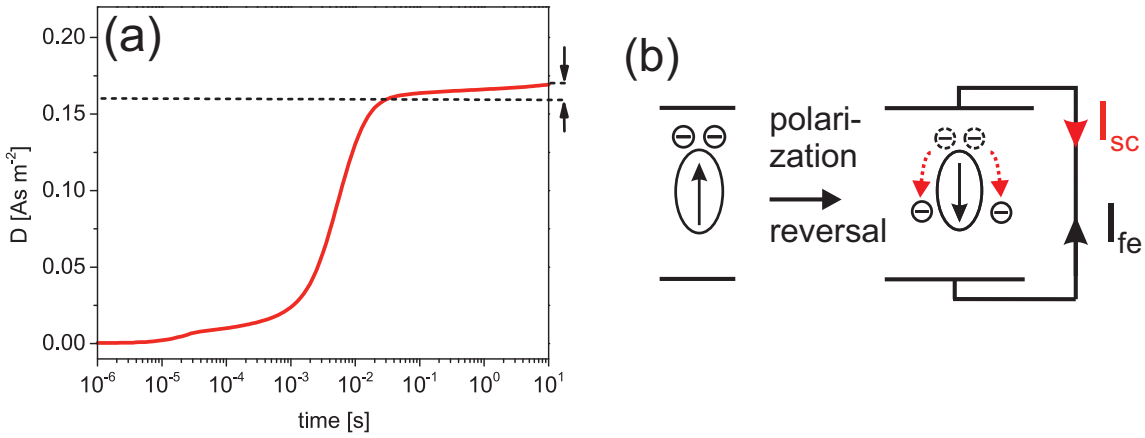


FIGURE 5.11: (a) Ferroelectric polarization switching transient. b) Currents during ferroelectric polarization switching in the Space Charge Model.

## 5.7 Revisiting the Space Charge Model

The Space Charge Model is explained in section 3.2.2. In the following its validity is discussed in the light of present experimental findings. FIG. 5.11 a) depicts a ferroelectric polarization switching transient when applying an electric field step. In the retarded stages the polarization increases linearly on a logarithmic time scale (lift-off from the dashed line in FIG. 5.11 a)). Space charges, which are assumed to redistribute after polarization reversal within seconds [41], would result in a decay of the ferroelectric polarization switching transient in these retarded stages as outlined in FIG. 5.11 b). For simplicity only one charge species is depicted in FIG. 5.11 b) without loss of generality. The current associated to the change in ferroelectric polarization ($I_{fe}$) and that associated to redistributing space charges ($I_{sc}$), flow in opposite direction. Thus, the experimental result and the prediction of the Space Charge Model are in contradiction. But it needs to be stressed that an external field induced polarizing of the amorphous phase could cover the current sourced by the redistribution of space charges. Consequently, the increase of the ferroelectric polarization switching transient in the retarded stages is not evidence enough to discredit the Space Charge Model.

There is another experimental observation which isn't consistent with the pre-

dictions of the space charge model as discussed in the following. The time constant for the redistribution of space charges is given by the Maxwell relaxation time $\tau_{sc} = \varepsilon_r \varepsilon_0 / \sigma$, with estimations for the relative permittivity $\varepsilon_r = 10 - 15$ and the conductivity $\sigma = 10^{-11}\,\mathrm{A\,V^{-1}\,m^{-1}}$ to $10^{-12}\,\mathrm{A\,V^{-1}\,m^{-1}}$ [41]. From these values, $\tau_{sc}$ is estimated to be between 10 s to 100 s. Lew and Thompson demonstrated that the coercive field $E_c(t_w)$ evolves according to equation (5.3) at minimum over a range of $t_w$ between $10^{-4}$ s to $10^6$ s. Besides, in section 5.5 it is presented that $E_c(t_w)$ evolves at temperatures between $-20\,^\circ$C to $100\,^\circ$C continuously with a logaritmic dependence on $t_w$. Thus, to explain imprinting solely by the Space Charge Model, the existence of several space charge species exhibiting different mobilities is indispensable. The space charge relaxation process in P(VDF-TrFE) observed up to now is described by using a single relaxation time $\tau_{sc}$ [72]. Measurements at various temperatures revealed, that $\tau_{sc}$ follows an Arrhenius law, with $\tau_{sc} \approx 1$ s at $70\,^\circ$C [72]. In conclusion, the Space Charge Model cannot explain imprinting as a whole, but it is possible that space charges play a (minor) role in imprinting.

## 5.8 Imprint stretches over several decades in time

The imprint process stretches over several decades of $t_w$. Lew et al. demonstrated that the coercive field $E_c(t_w)$ follows the functional behavior stated in equation (5.3) over a huge time span of at least $10^{-4}s \leq t_w \leq 10^6 s$ [61]. A similar result is found in this work. FIG. 5.12 depicts the evolution of $\tau(t_w)$ over several decades of $t_w$. To gain data of $\tau(t_w)$ over such a wide range of $t_w$, three different experimental methods were applied, which are illustrated in FIG. 5.12 on the right. Next to the conventional de-aging by switching process described in section 5.2, an alternative de-aging process denoted as "alt. de-aging" is used. The alt. de-aging process consists in a continuous application of bipolar field pulses until $\tau$ resulting from two subsequent pulses is found to be the same. Note, in contrast to the measurement technique to gain red data points, the technique to gain blue data points includes a field offset during $t_w$. Besides, all techniques neglect the duration the system takes to switch in negative polarization direction ($\approx 3$ ms). This duration is included in $t_w$. While that is negligible for gaining red points, for blue data points that duration can be in the order of magnitude of $t_w$. Blue data points shall mainly be seen as evidence that imprint effects evolve even for very small values of $t_w$.

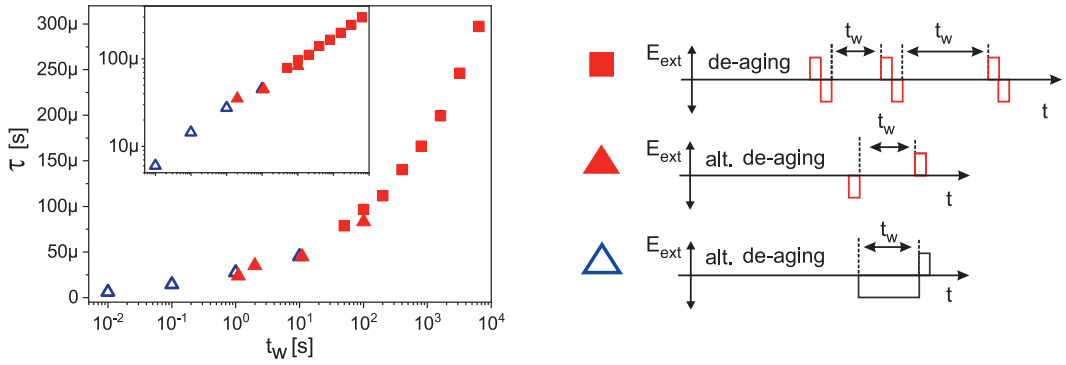


FIGURE 5.12: Evolution of imprint over a broad time scale. The inset shows the same data in a log-log plot. The amplitude of the applied electric field steps is $\pm$ 80 MV m$^{-1}$.

### 5.8.1 First evidence for $E_{imprint}$

Ikeda et al. demonstrated that if the polarization transients for different $t_w$ are scaled by $\tau$, all polarization transients collapse to one master polarization transient [41]. Since this is also true for polarization transients for different applied fields, the effect of waiting and that of the applied field satisfy the same scaling rule over time. Thus, it seems reasonable to assume that the effect of waiting is due to the decrease of the effective field [41]. Substituting the external field $E_{ext}$ by the effective field $E_{ext} - E_{imprint}$ which includes the imprint field $E_{imprint}$, yields in the empirical law for the external field dependence of the ferroelectric switching time $\tau$ [10].

$$\tau = \tau_{0,Arrh} \exp\left(\frac{E_a}{E_{ext} - E_{imprint}}\right) \tag{5.13}$$

[10] see equation 2.9 for the unmodified law

For $E_a >> E_{ext} >> E_{imprint}$ equation (5.13) results for $\log(\tau)$ in a straight line as a function of $E_{imprint}$. Comparison with the experimental result depicted in the inset of FIG. 5.12, where $\log(\tau)$ is a linear function of $\log(t_w)$, leads to the suggestion that $E_{imprint} \sim \log(t_w)$. This relation between $E_{imprint}$ and $\log(t_w)$ is also deduced in section 5.9.1.

## 5.9 Imprinting current density $j_{rel}$

After ferroelectric switching with an electric field pulse of $80\,\mathrm{MV\,m^{-1}}$ amplitude and 10s duration, the short ciruit current density $j_{depol}$ is measured. $j_{depol}$ is depicted in FIG. 5.13. In a linear time invariant (LTI) system $j_{depol}$ flows approximately as long as the poling pulse has been. This implies that for times $>> 10\,\mathrm{s}$, $j_{depol}$ in FIG. 5.13 originates either from a non-LTI system or there exists another source causing $j_{depol} \neq 0$ for times $>> 10\,\mathrm{s}$. In fact, $j_{depol}$ behaves as expected for a LTI system [75] at temperatures above $T_C$ as was shown by means of the field reversal experiment. Thus the non-LTI behavior is coupled to ferroelectricity.
Besides, it was found that an electric field pulse applied in opposite direction of the ferroelectric polarization vector without ferroelectric switching results in a short circuit current which flows for around the pulse duration [72]. A more detailed analysis (not shown) reveals, that this current changes sign at that point in time. Anticipating the explanation for the imprinting current, the change in sign of this current is caused by $j_{rel}$ which flows in this case in opposite direction to the current which is caused by relaxation of pulse activated dipoles.

Integration of $j_{depol}$ respective to the time elapsed since poling yields the time dependent decay of the remanent polarization $P_{rem}$. Note, for times much longer than the pulse duration, the time $t$ equals approximately $t_w$ [11]. According to the inset in FIG. 5.13, $P_{rem}$ decays per decade elapsed $t_w$ by the amount $\Delta P = 49\,\mathrm{nA\,s\,cm^{-2}}$.

### 5.9.1 Origin of $j_{rel}$ and estimate for $E_{imprint}(t_w)$

Using the New Imprint Model from section 3.3 the flow of $j_{depol}$ for times $> 10\,\mathrm{s}$ can be explained. For simplification some rd are omitted in FIG. 5.14 compared to the picture in FIG. 3.3. Hence, only rd located in the interstitial space between the crystallites are considered. These rd reorient during $t_w$ in anti-parallel fashion to $P_{fe-cryst}$. This simplification can be reasoned by the outcome of the field offset experiment (see section 5.4) and on the experimentally observed flow-direction of $j_{rel}$ (see later). The charges drawn in the electrodes in FIG. 5.14 are caused by electric influence. The red charges correspond to $P_{fe}$ and the green charges to $P_{rel}$ [12]. $P_{rel}$ and the imprint are zero in FIG. 5.14 a). In the time period $t_0 < t < t_w$, the rd align gradually, causing the build up of $P_{rel}$ and the flow of $j_{rel}$. Red and green charges have opposite signs, because $P_{fe}$ and $P_{rel}$ point in opposite direction. Since $P_{rel}$ increases as a function of $t_w$ the remanent polarization $P_{rem}$ decays as a function of $t_w$.

$j_{depol}(t)$ or rather $j_{rel}(t_w)$ can be used to estimate $E_{imprint}(t_w)$ as presented in the following. $P_{rel}$ can be calculated via the integral given in equation (5.14), whereas

[11] $t$ is the time elapsed since switching off the external field ($E_{ext} = 0$). $t_w$ is defined in section 4.3.3. Switching the polarization state at this field strength takes a fraction of a second. Consequently, one has $t \approx t_w - 10s$, thus for $t >> 10s$ one has $t = t_w$.

[12] Definitions for $P_{fe}$ and $P_{rel}$ are given in section 3.3.4

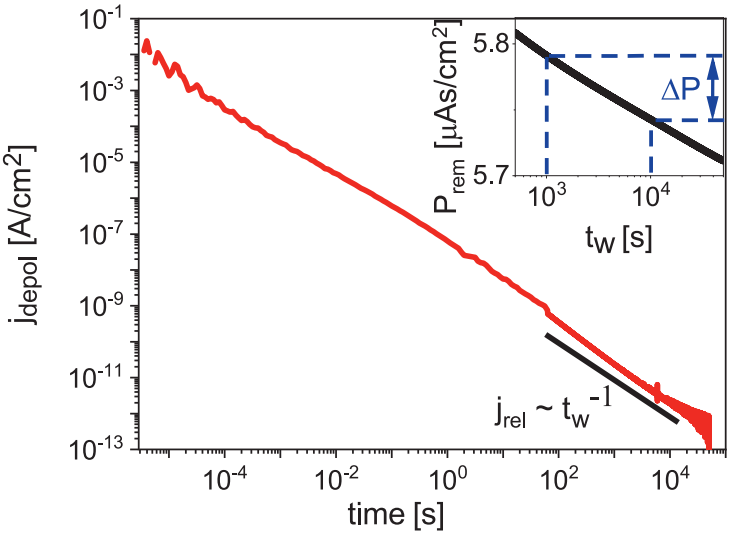


FIGURE 5.13: Short circuit current density $j_{depol}$ after a ferroelectric polarization switching pulse of 80MV/m and 10s duration. Reproduced from [87], with the permission of AIP Publishing.

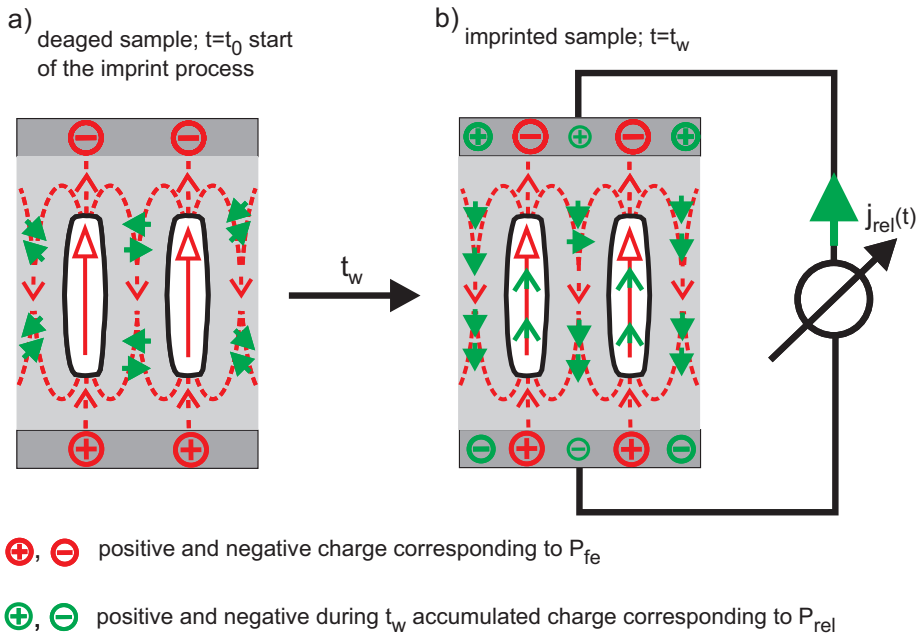


FIGURE 5.14: Origin of $j_{rel}(t_w)$ in the New Imprint Model (see also section 3.3): the imprint current density $j_{rel}(t_w)$ is caused by the reorientation of rd. a) No imprint. b) Imprinted sample. Reproduced from [87], with the permission of AIP Publishing.

$j_{rel}(t_w)$ is approximately proportional to $t_w^{-1}$, as can be seen in FIG. 5.13.

$$\text{for} \quad j_{rel} \sim t_w^{-1}: \quad P_{rel} = \int_{t_0}^{t_w} j_{rel}(t'_w)\, dt'_w = -\Delta P \cdot \log\left(\frac{t_w}{t_0}\right) \tag{5.14}$$

$$P_{rem}(t_w) = P_{fe} + P_{rel}(t_w) = P_{fe} - \Delta P \ \log\left(\frac{t_w}{t_0}\right) \tag{5.15}$$

Equation (5.15) presumes that the ferroelectric polarization $P_{fe}$ and the relaxational polarization $P_{rel}$ are the only contributions to the remanent polarization $P_{rem}$. In general other charge distributions like compensation charges (see section 6.5) contribute to $P_{rem}$ also. In equation (5.15) and in the inset of FIG. 5.13, $P_{rem}(t_w)$ decays by the same amount $\Delta P$ in each decade $t_w$. That means that in each decade of $t_w$ the same amount of rd align anti-parallel to $P_{fe-cryst}$ [13]. A linear relationship between $P_{rel}$ and $E_{imprint}$ is hypothesized:

$$E_{imprint} \sim \text{number of aligned rd} \sim P_{rel} \tag{5.16}$$

$$\Rightarrow \boxed{E_{imprint} \sim \Delta P \cdot \log\left(\frac{t_w}{t_0}\right)} \tag{5.17}$$

Equation 5.17 gives the time dependence of the imprint field. This results will be used in section 5.12 to calculate the effects of imprint.

## 5.10 Independence of imprinting from the electrode area

FIG. 5.15 depicts, that imprinting dosen't depend on the electrode area $A_{el}$. FIG. 5.15 on the left shows the ferroelectric switching time $\tau$ as a function of the waiting time $t_w$. FIG. 5.15 on the right shows $C^{norm}$ which is defined in equation (5.4) as a function of the waiting time $t_w$.

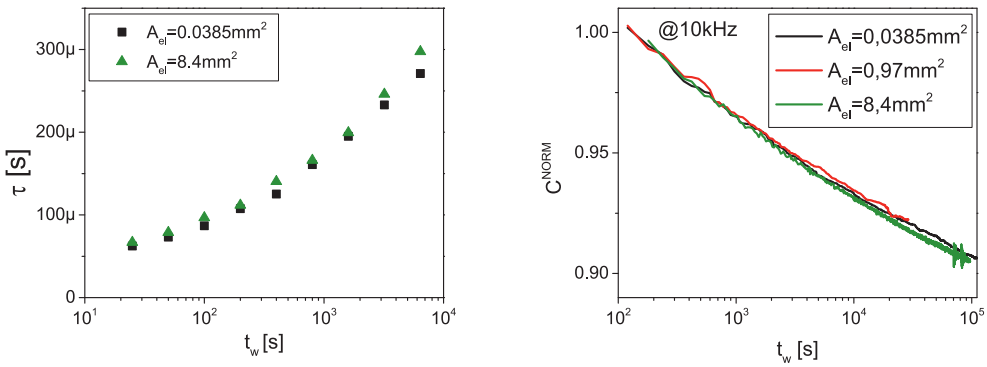


FIGURE 5.15: Imprinting is independent of the electrode area.

[13] This view is simplified, because the material exhibits at least two sorts of rd with different dipole moment, reconsidering the molecular dipoles of VDF and TrFE.

## 5.11 Dependence of imprinting on the crystallinity

P(VDF-TrFE) is a semi-crystalline co-polymer, as discussed in detail in section 2.3. The degree of crystallinity is altered using different sample preparation procedures (see section 2.3.9.2). FIG. 5.16 a) to d) depict imprinting effects for different degrees of crystallinity of the co-polymer. Depicted are the ferroelectric switching time $\tau$ (FIG. 5.16 a) and b)), the depolarization current density $j_{depol}$ (FIG. 5.16 c)) and the (relative change in) permittivity ((FIG. 5.16 d)). A fact to inform about when discussing FIG. 5.16 d) is, that the same trend which is observed for $\varepsilon(t_w)/\varepsilon(100s)$ with changing the crystallinity, is also observed for $\varepsilon(t_w)$. From these figures it can be concluded that imprint is slowed down for increased crystallinity.

For the reason of completeness, the absolute values of $\varepsilon$ at measurement frequency of 10 kHz are depicted in FIG. 5.16 f) as a function of the applied bias field. Interestingly, $P_{rem}$ dosen't markedly change comparing samples with different crystallinity (FIG. 5.16 e)). This is surprising, because the crystallinity is related to the amount of FE phase in the material. Thus, one would expect an increase in $P_{rem}$ with increasing crystallinity. A rather constant value of $P_{rem}$ for samples of various degree in crystallinity was also observed by another group [74]. Nevertheless, imprinting proceeds the slower the higher the co-polymers crystallinity. Conversely, the higher amorphous material content the faster proceeds imprint. In the view of the New Imprint Model, this experimental results are interpreted as follows: The higher the amorphous material content the more rd there are, which can align in direction of the stray field of $P_{fe-cryst}$ during $t_w$. The more rd align the higher $j_{rel}(t_w)$ and $E_{imprint}(t_w)$, which causes the change in $\tau$, $E_c$ and $\varepsilon$ as a function of $t_w$ (see section 5.12). A final note: Irrespective of the degree in crystallinity, the imprint effects depicted in FIG. 5.16 proceed all as functions of $\log(t_w)$. This evidences that the crystallinity doesn't affect the distribution of energy barriers [14] / relaxation times of rd.

[14] the existence of an energy barrier distribution for reorientation of rd is reasoned in section 3.3.3.

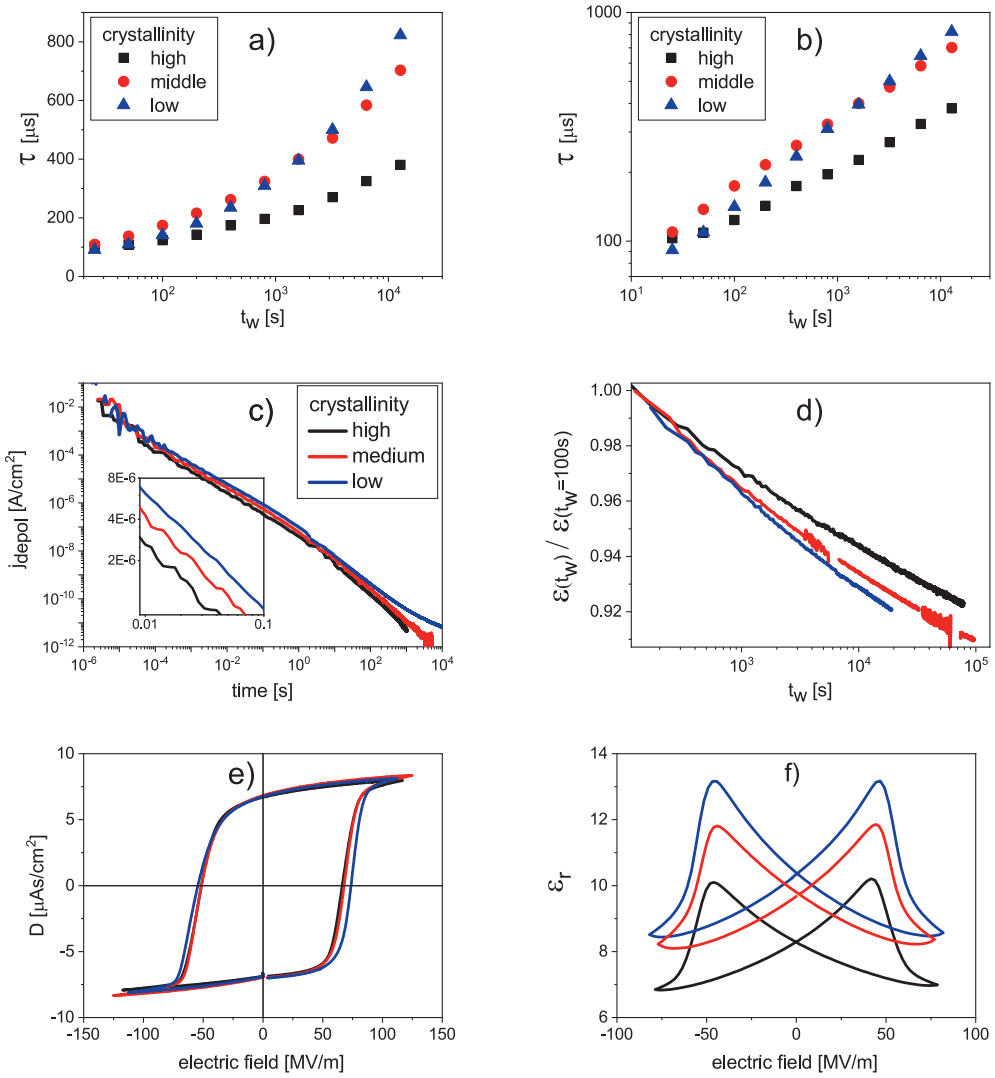


FIGURE 5.16: Variable degree in crystallinity. Effects of imprint in a), b), c) and d). Polarization hysteresis in e). Relative permittivity in f). The legend in c) also applies to d), e) and f). The polymer films have a thickness of around 500 nm. Reproduced from [87], with the permission of AIP Publishing.

## 5.12 Calculation of the effects of imprint - The extended Weiss model

The impact of the imprint field $E_{imprint}$ on the coercive field $E_c$, the ferroelectric switching time $\tau$ and the permittivity $\varepsilon$ is calculated using an extended Weiss model [53, 87]. The model only considers the ferroelectric phase but includes the imprint field in the local field present at the location of ferroelectric dipoles (fd).
The model is essentially a feedback-model: The ferroelectric polarization $P$ [15] feeds back on the local electric field $E_{loc}$, as can be seen by the Weiss field (see also equation (2.3)) contribution in equation (5.18). The local electric field at a ferroelectric dipole site can then be written as

$$E_{loc} = \underbrace{\beta P}_{\text{Weiss field}} + E_{imprint} + E_{ext} \tag{5.18}$$

where $\beta$ and $\beta P$ is a coupling constant and the so called Weiss field, respectively. The external electric field ($E_{ext}$) is applied to induce ferroelectric polarization switching. Note, the polarization, which changes in time during ferroelectric polarization switching, acts via the Weiss field first as hindrance to ferroelectric polarization reversal but as soon as the polarization changes sign, the new polarization state is endorsed.
Considering positive charges representative for fd, the process of ferroelectric polarization switching can be described by charges fluctuating in double well (dw) potentials. The dw potentials are depicted in FIG. 5.17. The number of charges occupying either the right or the left well depends on $E_{loc}$.
The transient polarization is described by a first order rate equation ($\tau_0$ microscopic relaxation time, $W_0$ barrier height of the double well potentials, m dipole moment, n dipole density and $k_B$ Boltzmann constant).

$$\tau \frac{dP}{dt} + P = nm \tanh\left(\frac{mE_{loc}}{k_B T}\right) \tag{5.19}$$

$$\tau = \frac{\tau_0}{2} \exp\left(\frac{W_0}{k_B T}\right) \Big/ \cosh\left(\frac{mE_{loc}}{k_B T}\right) \tag{5.20}$$

$E_{imprint}$ is set constant during ferroelectric switching which includes the time period while traversing a hysteresis loop. The differential equation (5.19) is numerically solved using a forth order Runge Kutta algorithm.

FIG. 5.17 illustrates how the fields act on a double well (dw) potential system. The dw's are symmetrical if the local field is zero. A charge q occupies the left and the right well with same probability (FIG. 5.17 a)). A non-zero ferroelectric polarization results in a Weiss field with the potential contribution $W_{weiss} = m\beta P$. According to the direction of the Weiss field, more charges occupy the left well and the ferroelectric polarization stabilizes itself via the Weiss field (FIG. 5.17 b)). The imprint field with a potential contribution of $W_{imprint} = mE_{imprint}$ stabilizes the ferroelectric polarization state furthermore (FIG. 5.17 c)). Now, switching the ferroelectric polarization by application of an external field $E_{ext}$ is hindered by $E_{weiss}$ [16] and $E_{imprint}$ as

[15] $P$ is not $P_{fe}$, because the model neglects the amorphous material content.

[16] $E_{weiss}$ hinders ferroelectric polarization switching only in the beginning of the ferroelectric switching process. After passing $P = 0$ the Weiss field enhances ferroelectric switching.

depicted in FIG. 5.17 d). $E_{imprint}$ increases according to the equation 5.17 with $t_w$, thus the ferroelectric polarization switching processes is the more delayed/hindered the longer $t_w$. In equation (5.17), $E_{imprint}$ increases linearly on a logarithmic time scale.

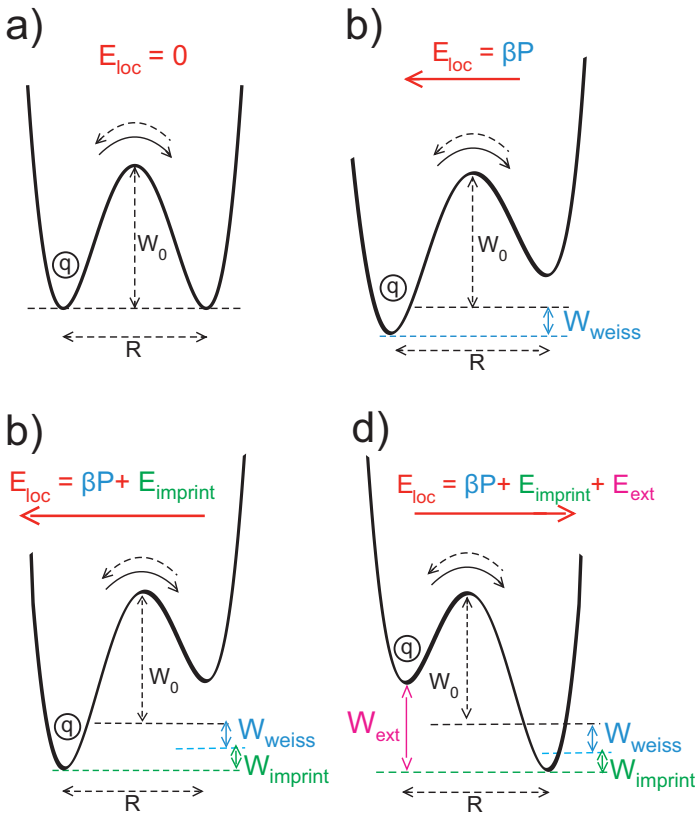


FIGURE 5.17: Double well (dw) potentials. The electric dipole moment $m$ equals $qR/2$, where $R$ is the distance between the wells. (a) Symmetric dw. (b) $E_{loc}$ equals the Weiss field that stabilizes the ferroelectric polarization $P$. (c) $E_{imprint}$ stabilizes the polarization state as does the Weiss field. (d) $E_{ext}$ is applied to switch the polarization state; $q$ tends now to jump to the right well. Reproduced from [87], with the permission of AIP Publishing.

Thus a linear increase of $E_{imprint}$ in the model corresponds to imprint effects which evolve as a function of $\log(t_w)$. The model based calculations are carried out with the following set of parameters: $\beta = 0.05/\varepsilon_0$ ($\varepsilon_0$...vacuum permittivity), $W_0$=4.5 $\cdot$ $10^{-20}$J, 2m=qR=1.5 $\cdot$ $10^{-27}$ Ccm, n=1.85 $\cdot$ $10^{22}$ cm$^{-3}$, $\tau_0$=$10^{-11}s$.

In FIG. 5.18 a) and b) model-based hysteresis loops and polarization switching transients are depicted. In the Weiss calculation, $W_{imprint}$ is set to remain constant while traversing a hysteresis loop. As a consequence, the whole hysteresis loop shifts to the right, and both coercive fields change with equal magnitude. This equal shift of $-E_c$ and $+E_c$ is not observed experimentally, which is reasoned in section 5.2.2. From FIG. 5.18 a) the coercive fields and the relative permittivities are determined. In contrast to the experiment, where $\varepsilon_r$ is determined by a LCR meter measurement at 10kHz, the model based values of $\varepsilon_r$ are found by using equation (5.1) [17]. Note, the model based $\varepsilon_r$ neglects the amorphous phase and the high frequency polarization. From FIG. 5.18 b) the ferroelectric switching times are determined by a best fit of a

[17] $D$ is substituted by $P$

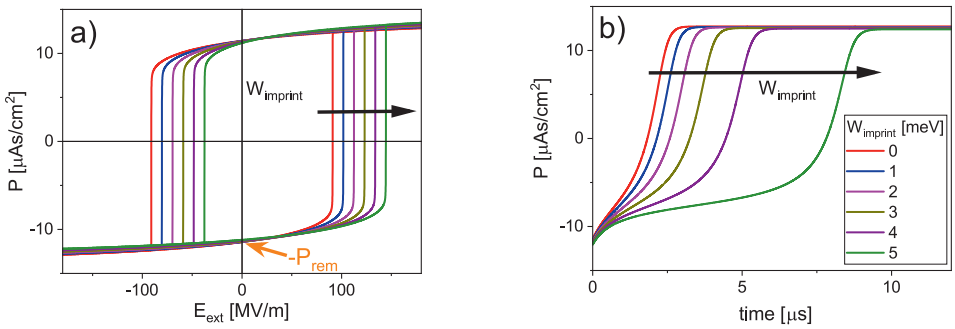


FIGURE 5.18: a) Calculated ferroelectric polarization hysteresis loops. b) Calculated ferroelectric polarization switching transients. The legend in b) also applies to a). Reproduced from [87], with the permission of AIP Publishing.

stretched exponential function to the calculated polarization transient (see equation (2.7)).
FIG. 5.19 compares model to experiment based values of $E_c$, $\varepsilon_r$ an $\tau$. While the model based values are plotted as a function of $W_{imprint}$, whereas $W_{imprint} \sim E_{imprint} \sim \log(t_w)$, the experimental values are plotted as a function of $\log(t_w)$. As shown in FIG. 5.19, model and experimental based values of $E_c$, $\varepsilon_r$ and $\tau$ follow the same functional trends. Note, the applied field $E_{ext}$ in the model at $E_{imprint} = 0$ was adjusted to equal the experimental value of $\tau(t_w = 25)$.

Going more into detail, becomes difficult, because the model fails to predict the experimentally observed absolute value of $E_c$ and $\varepsilon_r$, for the used set of parameters, which is often a complication in calculations [59, 80]. Still it's tried to answer the question if the same $W_{imprint}$ causes $E_c$ and $\varepsilon_r$ to change. Comparing the relative change of $E_c$ and $\varepsilon_r$ over 3 decades of $t_w$: The experimental $E_c$ changes by 18.7% in FIG. 5.19 b). 18.7% change in $E_c$ correspond to a change of 1.64 meV in $W_{imprint}$ in FIG. 5.19 a). The case is more complex for $\varepsilon_r$, since at first the omission of the amorphous phase needs to be recondsidered. That is done by using the Maxwell–Garnett approximation [102] for the following assumptions: the permittivity of the amorphous phase does not change with imprint, the permittivity of the ferroelectric phase equals the permittivity of the amorphous phase at $W_{imprint} = 0$, the crystalline inclusions (ferroelectric crystallites) are spheres, and the degree of crystallinity is approximately 60% [3]. The Maxwell-Garnett approximation is given by the red dashed line in FIG. 5.19 c). Second, the curves $\varepsilon_r(t_w)$ as well as $\varepsilon_r(W_{imprint})$ are not entirely straight thus the relative change calculated depends on the decades of $t_w$ considered. In the 3 decades of $t_w$ between $1 \times 10^2$ s and $1 \times 10^5$ s $\varepsilon_r$ decreases by 9.7% in the experiment. Starting for the calculated values of $\varepsilon_r$ at $\varepsilon_r(W_{imprint} = 0)$ and decreasing this value by 9.7%, then the corresponding value is found at 1.65 meV, under consideration of the Maxwell Garnett approximation. Thus in this rough estimation with relative changes, the magnitude of change resulting from the same $W_{imprint}$ is comparable for $E_c$ and $\varepsilon_r$.
Note, the behavior of $P_{rem}(t_w)$ is included in the model, since equation (5.17) was deduced from $j_{rel}(t_w)$, which is connected to $P_{rem}(t_w)$ via equation (5.2).

In summary, introducing the imprint field from equation (5.17) as local field contribution in the Weiss mean field approach yields for all in equation 5.3 stated effects of imprint a correct description of the functional time behavior.

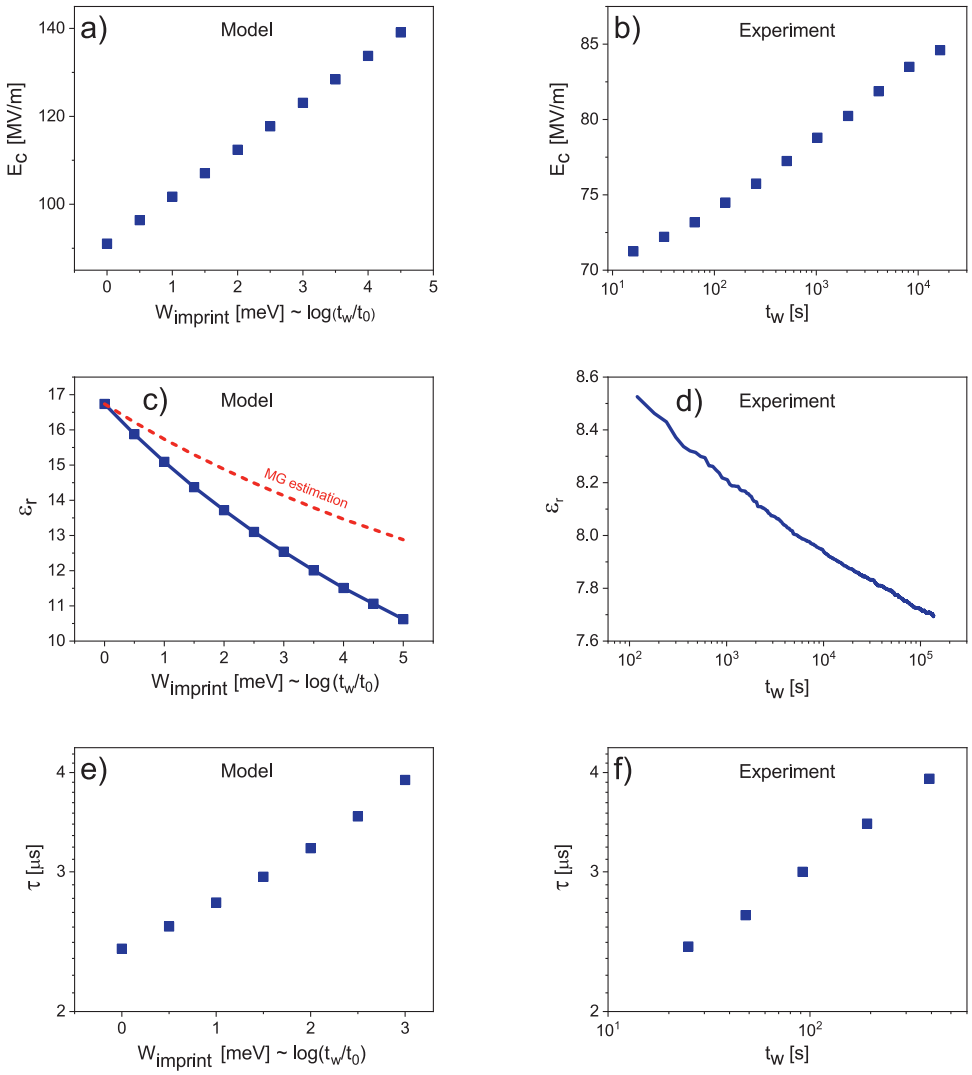


FIGURE 5.19: Comparison of model based and measured imprint effects. In a), c) and e) model based values of the coercive field, the permittivity and the ferroelectric switching time are presented, respectively, as functions of the energy barrier $W_{imprint}$. In b), d) and f) experimental values of the coercive field, the permittivity and the ferroelectric switching time are presented, respectively, as functions of the waiting time. Reproduced from [87], with the permission of AIP Publishing.

# Chapter 6

# Results and Discussion II: Imprinting and Pyroelectricity

## 6.1 Introduction

The main goal in this chapter is a describtion of the temperature dependence of imprinting. Therefore the current flowing in the outher circuit is monitored when the samples temperature is changed with constant rate. The investigation is restricted to temperatures between $-20\,^{\circ}\mathrm{C}$ to $135\,^{\circ}\mathrm{C}$, which is above the lower glass transition (see section 2.3.11) and below the melting temperature $T_m$ [1].
According to section 4.4 there exists a small temperature gradient across the sample, which limits the accuracy of the temperature measurement. The term background (bg) current (see section 6.2.1) is used to summarize all short circuit current contributions, which origin form subsidiary effects. In the later stages of this work the amplitude of the bg current could be reduced to a great extent by measures listed in section 6.2.3. Still, data of before and intermediate stages of bg current reduction are discussed, since some interesting results were found before some factors influencing the bg current were discovered. The data presented for poled samples were gained from experiments in which all in section 6.2.3 listed measures were applied to reduce the bg current.
Due to varying sample preparation parameters and measurement setups, relevant experimental details are stated using in a smaller font size.
At first un-poled samples are investigated. A ferroelectric polarization versus temperature hysteresis is found by thermal cycling across the Curie transition [2]. In unpoled samples these hysteresis loops are closed.
In contrast for poled samples, these hysteresis loops are not closed. Besides, for poled samples it is shown that the short circuit current under thermal cycling is composed of a reversible and an irreversible current contribution, at temperatures below the ferroelectric to paraelectric phase transition temperature range. It is shown that the origin of the reversible and irreversible current contribution is pyroelectricity and imprinting, respectively. Using the New Imprint Model and assuming Debye-like polarization processes in the imprinting mechanism the imprinting current $j_{rel}$ while heating with constant rate is calculated. Finally, in section 6.11 and 6.11.1 the location of imprint related relaxation processes is rediscussed.

[1] $T_m$ equals approximately $148\,^{\circ}\mathrm{C}$ [74].
[2] Note, the definition of the Curie Temperature $T_C$ given in section 2.1.

## 6.2 Un-poled samples

Samples directly after sample preparation or after de-aging above $T_C$ (see section 5.2.3) are investigated. Short circuit currents are monitored while heating and cooling with constant rate. Except in the end of this section the current while external field application is measured in the outer circuit while cooling. The temperature range investigated is 25 °C to 135 °C. The only phase transitions expected in this temperature range are the transition from the ferroelectric to the paraelectric state and the transition from the paraelectric to the ferroelectric state. These transitions occur between 80 °C to 110 °C and between 80 °C to 50 °C while heating and cooling, respectively [3]. A literature review on the structural changes taking place in heating-cooling cycles in the temperature range 25 °C to 135 °C is given in section 2.3.8.2. Note, the discussion on pyroelectricity for un-poled and poled samples in section 2.3.11.1.

### 6.2.1 Background (bg) current

Details on sample preparation and the measurement setup: The sample is annealed above $T_m$ and the co-polymer film is approximately 460 nm thick. No measures are taken to reduce the bg current (see section 6.2.3). A heating/cooling rate of 1 °C min$^{-1}$ is used. The temperature is determined from the sensor in the heating stage (see section 4.4).

FIG. 6.1 a) depicts the short circuit current density measured during a heating - cooling cycle directly after sample preparation (1st temperature loop). At temperatures above $T_C$, thus in the paraelectric phase ($T_C < T < T_m$) [3], neither a pyroelectric current, an imprinting related current nor any other current associated with the ferroelectric polarization is expected and consequently the measured current equals the so called background (bg) current. A measurement conducted thereafter (3rd temperature loop), is depicted in FIG. 6.1 b). The bg current has declined and remains now rather constant at the maximum temperature. It is observed, that the bg current declines fast at elevated temperatures and is decreased in subsequent measurements. FIG. 6.2 compares short circuit current densities measured in bc and tc [4]. FIG. 6.2 a) and b) depict the heating- and cooling process, respectively [5]. Charge movements located in the space between the electrodes generate current densities with $j_{bc} = -j_{tc}$. The complement are charge movements located outside the plate capacitor structure, which generate current densities with the same sign for $j_{bc}$ and $j_{tc}$. Comparing $j_{tc}$ just before the start of the cooling process with $j_{bc}$ in the end of the heating process, thus at the maximum temperature, where the bg current is the only contribution to the measured current, it can be concluded that a certain part of the bg current originates from between the electrode plates [6] and another part from outside. The current density peaks at temperatures around 100 °C while heating and 50 °C while cooling, can be associated to the decay and build-up of the spontaneous ferroelectric polarization, respectively as discussed in detail in the following sections.

[3] The Curie Temperature $T_C$ marks the lowest temperature above which ferroelectricity has completely vanished (see section 2.1). For un-poled standard annealed samples $T_C$ equals around 113 °C, see also FIG. 6.4 a).

[4] Details on the experimental setup regarding bottom connection (bc) and top connection (tc) are given in section 4.5.

[5] The measurement in bc was conducted after the measurement in tc.

[6] see the discussion in section 4.5

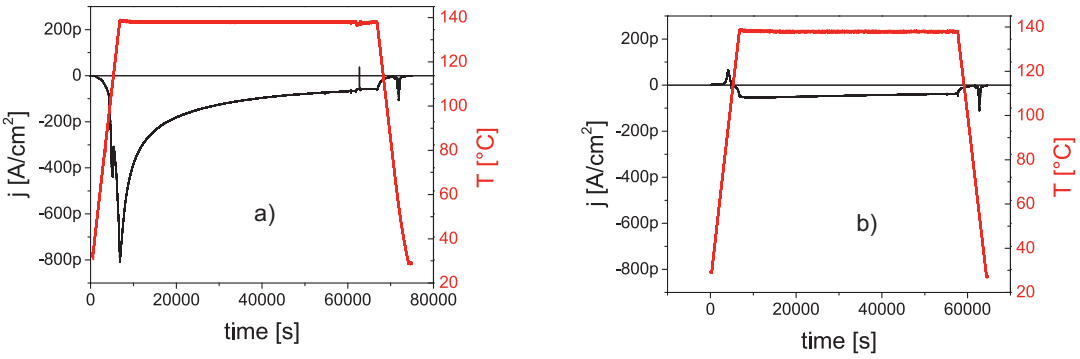


FIGURE 6.1: Short circuit current density and temperature as a function of time. Data is recorded: a) directly after sample preparation; b) in a subsequent temperature cycle.

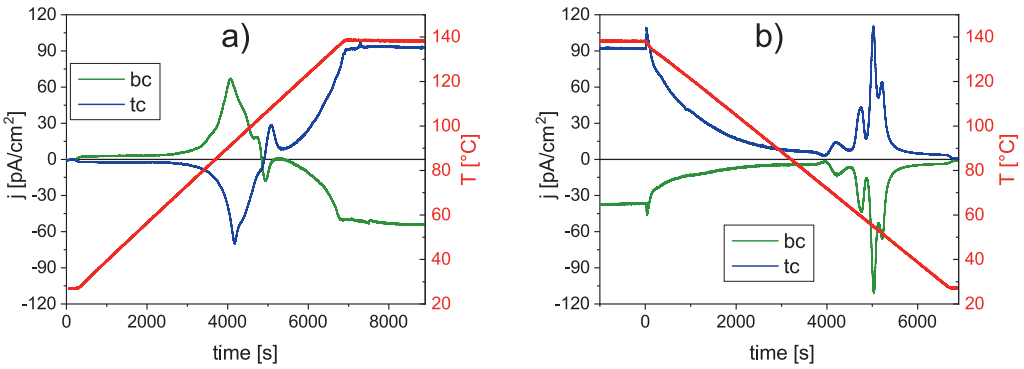


FIGURE 6.2: Comparison of the short circuit current density measured in tc and bc. a) Heating process. b) Cooling process. Sample with $T_{anneal} > T_m$.

### 6.2.2 Fit-function for the bg current

FIG. 6.3 depicts the current density from FIG. 6.2 in tc as a function of the temperature. The functions $j_A$ [7] are best-guess functions for the bg current contribution present while heating and cooling. $j_B$ is the average of $j_A$ while heating and $j_A$ while cooling (see equation 6.2). Subtraction of $j_B$ from the measured current density $j$ in FIG. 6.3 a) results in the current density depicted in FIG. 6.3 b). Integration of the current density depicted in FIG. 6.3 b) respective to time and considering that the ferroelectric polarization is zero above $T_C$ results in the polarization versus temperature hysteresis shown in FIG. 6.3 b). Note, the vector of the polarization depicted in FIG. 6.3 b) points towards the top electrode.

$$j_A(T) = j_0 + j_1 \cdot \exp(T/T_0) \tag{6.1}$$

$$j_B = \frac{1}{2} \cdot \left(j_{A,heating}(T) + j_{A,cooling}(T)\right) \tag{6.2}$$

[7] The time dependence of $j_A$ is neglected. This is reasoned by the small difference ($1\,\mathrm{pA\,cm^{-1}}$) in $j$ which results by waiting 1 h at the maximum temperature (see FIG. 6.2 b)). Such a small difference results if the sample is annealed at high temperature for many hours before the measurement (for details see section 6.2.1).

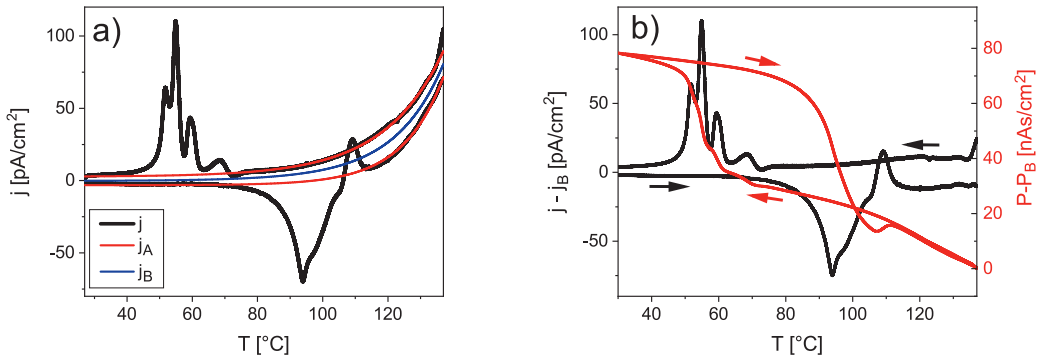


FIGURE 6.3: a) Exponential function fit to the bg current. The sample has been annealed above $T_m$. b) Current density after bg current density correction and polarization versus temperature hysteresis (in red) determined after bg current density correction.

### 6.2.3 Samples prepared in water-free environment

Details on sample preparation and the measurement setup: The sample is prepared with $T_{anneal}$ =130 °C ($T_C < T_{anneal} < T_m$) and de-aged above $T_C$ before all measurements. A heating and cooling rate of 3 °C min$^{-1}$ is used. All below mentioned measures for bg current reduction are applied.

The bg current can be reduced by taking following measures:

- sample preparation in dry atmosphere and using a solvent with low water content (for details see section 4.1.3.1).
- preheating the glass-substrate before sample preparation (for details see section 4.1.1).
- inserting a stack of $Al_2O_3$ and thermal pad between sample and heating stage (for details see section 4.5).

FIG. 6.4 a) and b) depict short circuit current densities measured during heating-cooling cycles in tc and bc [8]. The bg current contribution is low, as is best seen at the maximum temperature. The residual bg current density is symmetric with $j_{bc} \approx -j_{tc}$, consequently the measured short circuit current density origins almost completely from the polymer and/or its interfaces with the electrodes (for details see section 6.2.1).

#### 6.2.3.1 Spontaneous ferroelectic polarization versus temperature hystereses

The temperatures denoted in FIG. 6.4 a) mark the peak and the end of the ferroelectric to paraelectric (PE) phase transition and vice versa. The ferroelectric to paraelectric phase transition while heating is completed at 113 °C and the paraelectric to

[8] Details on the experimental setup regarding bottom connection (bc) and top connection (tc) are given in section 4.5.

ferroelectric phase transition is completed at 48 °C, as it is similarly found in DSC and X-ray diffraction measurements [3]. These current peaks indicate that not all $\mathbf{P}_{\mathbf{fe-cryst}}$ [9] are randomly oriented in un-poled samples, as stated in section 2.3.11.1. This might be the consequence of a certain amount of pinned dipoles in the electrode adjacent layers [32]. $|P|$ depicted in FIG. 6.4 c) is calculated from the current densities

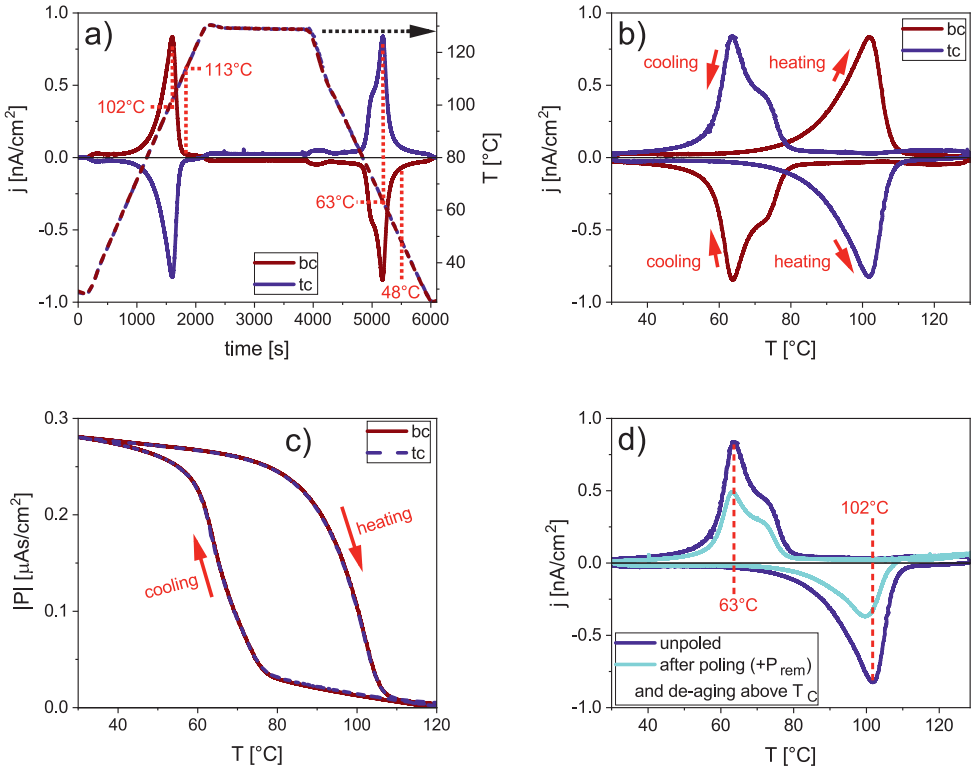


FIGURE 6.4: a) and b) Short circuit current densities measured once in tc and once in bc during a heating-cooling-cycle. c) Spontaneous decay and build up of the ferroelectric polarization. d) Effect of poling. Sample with $T_{anneal}$ =135 °C.

depicted in FIG. 6.4 a), by taking the absolute value of the integral respective to time in the limits of the heating/cooling duration and subsequent shift to equal zero at around 120 °C. This integral is based on equation (2.14) and theoretically discussed in section 2.3.11.1 . The polarization in FIG. 6.4 c) points towards the top electrode. This polarization arises and decays spontaneously by a change in temperature. The polarization versus temperature hysteresis presented in FIG. 6.3 b) and FIG. 6.4 c) originate from samples with different $T_{anneal}$. Clearly apparent is the difference in current peak pattern and the difference in amount of spontaneous ferroelectric polarization present at room temperature. This severe change in behavior is caused by the permanent structural change that takes place by thermal annealing above $T_m$ [10]. FIG. 6.4 compares current densities measured before the sample has ever been poled with thereafter. Poling appararently affects the amplitude of the current density related to decay and build-up of the ferroelectric polarization even after de-aging above $T_C$. Besides, the temperatures at the current density peaks are slightly shifted.

[9] $\mathbf{P}_{\mathbf{fe-cryst}}$ is the vector of the ferroelectric polarization in a ferroelectric crystallite.
[10] Further information is given in section 2.3.9.2.

A corresponding temperature shift is also seen in DSC measurements [3]. Nevertheless, according to FIG. 6.4 c), the impact of a poling history is rather low. Thus, in the following it is taken as confirmed, that by de-aging above $T_C$ the electric history is deleted as suggested by Bargain et al. [3].

## 6.3 Cooling with different rates from above $T_C$; temperature shift of the phase transition

Details on sample preparation and the measurement setup: The sample is annealed with $T_{anneal} = 135\,^{\circ}\mathrm{C}$, which is between $T_C$ and $T_m$. The co-polymer film is approximately 400 nm thick. The measurement is conducted in tc (see section 4.5). The temperature is determined from the sensor in the heating stage (see section 4.4). Following bg current reduction measures (see section 6.2.3) are applied: $Al_2O_3$ platelet between sample and stage and the glass-substrate is heated before sample preparation. A small background current is present, as can be seen in FIG. 6.5 a) at the maximum temperature, where the bg current density is the only contribution to the measured current density (for details see section 6.2.1).
FIG. 6.5 a) depicts the short circuit current measured while cooling for different cooling rates. It can be seen, that the current peaks which mark the climax of the paraelectric to ferroelectric phase transition while cooling are shifted to cooler temperatures with increasing cooling rate [11]. This can be explained as follows. An un-poled sample or a sample which has been de-aged above $T_C$ is imprinted at room temperature, but imprint free above $T_C$, as discussed in section 5.2.3. The ferroelectric polarization in crystallites ($P_{fe-cryst}$ (see section 3.3.4) starts to build up at the onset temperature of the paraelectric to ferroelectric phase transition. A bit later imprint starts to build up too: The rd, which are initially randomly oriented, align with the stray fields of $\mathbf{P_{fe-cryst}}$. This reorientation process of rd is fast at elevated temperatures [12], but still dependent on the time [13]. Consequently, with decreasing cooling rate an increased imprint field $E_{imprint}$ is present at any temperature just below the onset temperature of the paraelectric to ferroelectric phase transition. The imprint field points in direction of $\mathbf{P_{fe-cryst}}$ and promotes the build-up of $P_{fe-cryst}$. Thus, the slower the cooling process the higher the temperature at which a certain amount of ferroelectric polarization is built up. Moreover, the additional $\mathbf{P_{fe-cryst}}$ enhances the stray field. Thus, the shift of the above mentioned climax is self-reinforcing on the one hand by the temperature dependence of the rd reorientation process and on the other hand by the presence of higher stray fields the slower the cooling process.
For the counterpart, the heating process, additionally a shift of the Curie Temperature [14] is expected, since it can be assumed that $E_{imprint}$ enhances the temperature stability of the ferroelectric polarization/phase. To measure this effect, care has to be taken, not to conduct the initial cooling process with different rates.

The same experiment is conducted but with the sample discussed above with $T_{anneal} > T_m$. The short circuit current density measured while cooling is depicted in FIG. 6.5 b). Again a shift of the temperature which marks the climax of the paraelectric to ferroelectric phase transition is observed in the same manner as in the

[11] A shift is also observed in high precision DSC measurements conducted for a broad range of cooling (and heating) rates using melt crystalized samples [14], which are comparable to the sample with $T_{anneal} > T_m$
[12] The rd reorientation processes are faster the higher temperature
[13] due to the broad distribution of relaxation times, for details see section 3.3.3.
[14] Note, the definition of the Curie Temperature $T_C$ given in section 2.1.

above mentioned case, but the magnitude of the shift is smaller: Comparing the temperatures at the highest current density peak for cooling rates of 0.1 °C min$^{-1}$ and 1 °C min$^{-1}$ in FIG. 6.5 b) reveals a shift of 1.5 °C. For the above sample annealed with $T_{anneal}$ = 135 °C that shift amounts to 8 °C, as can be seen in FIG. 6.5 a). Following the reasoning from above, the temperature shift is caused by the positive feedback between the building-up of ferroelectric polarization and the building-up of imprint. The smaller temperature shift observed for the above $T_m$ annealed sample (FIG. 6.5 b)) compared to the sample with $T_{anneal}$ =135 °C (FIG. 6.5 a)) might be a consequence of the difference in ferroelectric polarization present. The remanent polarization determined from the polarization hysteresis at room temperature equal 6 µA s cm$^{-2}$ and 3 µA s cm$^{-2}$ for the at 135 °C and above $T_m$ annealed sample, respectively. The spontaneous polarization at around 30 °C determined from FIG. 6.4 c) and FIG. 6.3 b) equal 0.28 µA s cm$^{-2}$ and 0.08 µA s cm$^{-2}$ for the at 135 °C and above $T_m$ annealed sample, respectively [15].

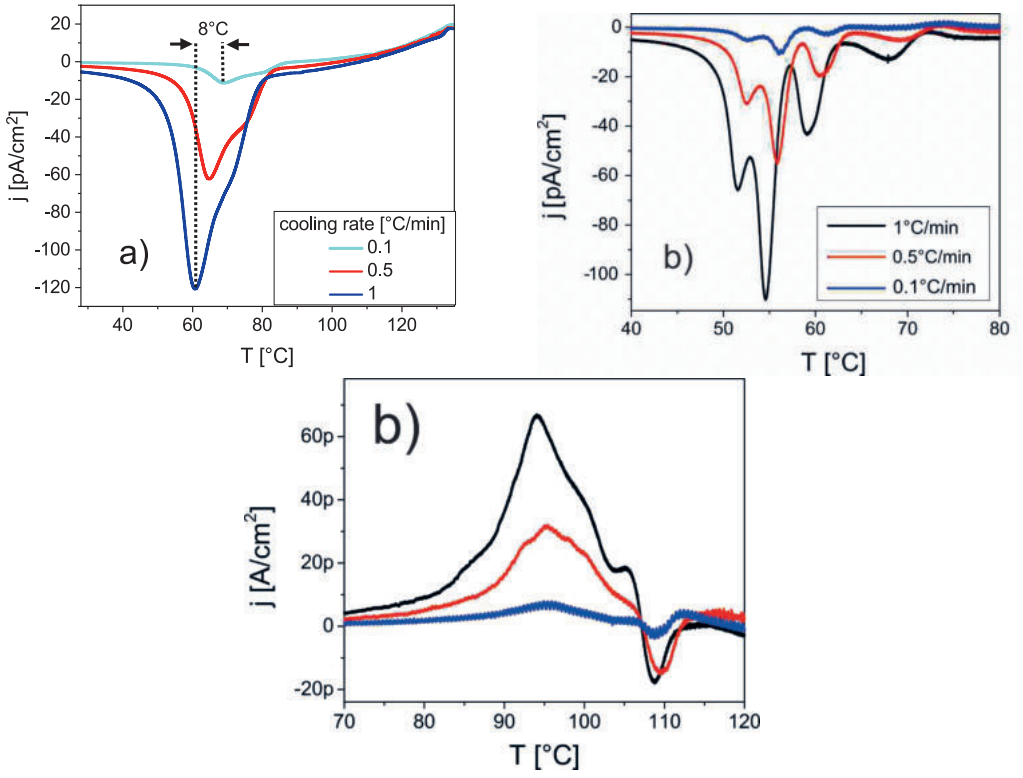


FIGURE 6.5: Short circuit currents densities while cooling from above $T_C$ for different cooling rates. a) Sample with $T_{anneal}$ =135 °C. b) Sample with $T_{anneal} > T_m$.

[15] A discussion on the impact various $T_{anneal}$ on the ferroelectric response and the amount of present ferroelectric phase is given in section 2.3.9.2.

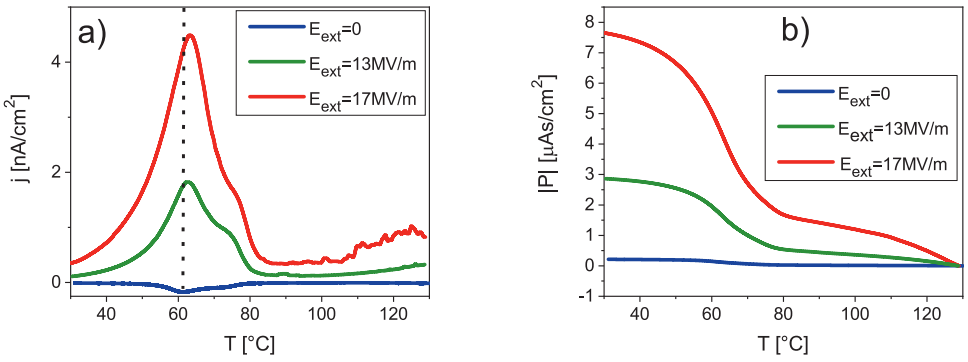


FIGURE 6.6: Impact of a field offset while cooling: The external electric field $E_{ext}$ is applied while cooling. a) Current density j. b) Integration of j (from a)) respective to time.

## 6.4 Electric field offset while cooling from above $T_C$

Details on sample preparation and the measurement setup: The sample is annealed with $T_{anneal} = 135\,°C$ and the co-polymer film is approximately 400 nm thick. The following measures are applied to reduce the bg current (see section 6.2.3): Preheating the glass-substrate before sample preparation. The temperature is determined from the sensor in the heating stage (see section 4.4).

A constant electric field $E_{ext}$ is applied while cooling with a rate of $1\,°C\,min^{-1}$. The amplitudes of $E_{ext} = 13\,MV\,m^{-1}$ and $E_{ext} = 17\,MV\,m^{-1}$ correspond to $E_c/3$ and $E_c/4$, respectively [16]. The value of the remanent polarization of the hysteresis might be of interest and is therefore given here: $P_{rem} = 7.2\,\mu A\,s\,cm^{-2}$. The external electric field $E_{ext}$ is applied at 133 °C, which is above $T_C$, and after letting the current response decline at this temperature for 30 min, the sample is cooled down to room temperature with the field still applied. FIG. 6.6 a) depicts current density, measured in the outer circuit while cooling. $|P|$, depicted in FIG. 6.6 b), is calculated via integration of the current densities depicted in FIG. 6.6 a) respective to time. For $E_{ext} \neq 0$ a part of the measured current is caused by dc conduction. It is assumed that dipoles located in the amorphous phase orient mainly at 133 °C during the time period of the current decline. The dipoles are *frozen in*[17] while cooling. The current density peaks occurring in FIG. 6.6 are associated to the build-up of the ferroelectric polarization and mark the climax of paraelectric to ferroelectric phase transition. The higher $E_{ext}$ the higher the current (peak). Note, only the ferroelectric polarization vector component perpendicular to the electrode plane contributes to the current (see section 2.3.11.1). $E_{ext}$ promotes this orientation while cooling.

Explaining the temperature shift of the current peaks: The current peaks are shifted with increasing $E_{ext}$ to higher temperatures. The external field applied while cooling eases the build-up of the ferroelectric polarization by inducing order into the system. Ferroelectricity is coupled to dipole order. In the dynamic process of the paraelectric to ferroelectric phase transition the system intents to reach equilibrium.

[16] The coercive field $E_c$ is determined from a ferroelectric polarization hysteresis at room temperature. The hysteresis is traversed with a frequency of 0.1 Hz.

[17] in the sense that, the dipoles maintain mostly their orientation

The equilibrium exists between the ordering forces, ferroelectric dipole (fd) interaction and $E_{ext}$, and the disordering force of the temperature. The system moves with increased deviation from equilibrium with increased speed towards the equilibrium and remains thereby dynamically balanced. To remain dynamically balanced, a certain ferroelectric polarization appears at higher temperatures with increasing amplitude of $E_{ext}$. Note, it can be assumed that the effect of $E_{ext}$ (see also section 5.4) on the shift towards higher transition temperatures is diminished by the dipoles which orient in the applied field before cooling. These field oriented dipoles in the amorphous phase generate a field similar to $E_{imprint}$, which is in contrast to $E_{imprint}$ in the short circuited case oriented anti-parallel to $P_{fe-cryst}$. That might be the reason why the temperature shift seen in the present experiment is smaller compared to that, that results when using different cooling rates (see section 6.3 and FIG. 6.5 a)).

## 6.5 Poled samples in the Curie transition temperature range

Sample parameters and measurement conditions: The co-polymer film is prepared with $T_{anneal} = 130\,°C$ and the co-polymer film is approximately 350 nm thick. The sample is initially de-aged above $T_C$ and then poled by traversing the ferroelectric polarization hysteresis three times with a frequency of 10 Hz at a temperature of 30 °C. 240 s after poling, the sample is heated to 130 °C kept at this temperature for 30 min and is then cooled back to 30 °C. A heating - / cooling rate of $3\,°C\,min^{-1}$ is used.

FIG. 6.7 a) depicts the short circuit current density and the temperature measured while heating. FIG. 6.7 b) depicts the polarization, which is calculated from the current densities measured while heating and cooling via integration respective to time.
Start in $-P_{rem}$:[18] Lets start with the description of the short circuit current density depicted in FIG. 6.7 a), for the case that the heating process starts at 30 °C in $-P_{rem}$. In the very beginning, right after poling, the temperature doesn't change much and remains for around 240 s between 30 °C to 31 °C. The current density declines in this time periode. This declining current density corresponds to the imprinting current density which flows after poling at constant temperature, as discussed section 5.9. In the temperature range between 32 °C to 80 °C the measured current exhibits two main contributions, which originate from pyroelectricity (see section 6.6 and 6.7) and imprinting (see section 6.8). Before reading the following paragraph it is advised to read section 2.3.8.2 first. The ferroelectric to paraelectric phase transition proceeds at temperatures exceeding 80 °C (see section 2.3.8.2). The DFE phase transforms in the approximate temperature range 80 °C to 100 °C continuously to the PE phase. The FE to PE phase transition occurs in the temperature range 100 °C to 112 °C. The completion of the ferroelectric to paraelectric phase transition can also be seen in FIG. 6.7 a), where the current density is almost zero above 115 °C. $P$ depicted in FIG. 6.7 b), equals the integral of the current density respective to time while heating/cooling with subsequent shift along the vertical axis to equal zero at 130 °C. For a start of the heating process in $-P_{rem}$, the value of $P$ equals $5.4\,\mu A\,s\,cm^{-2}$ at 30 °C. A similar value is found for the remanent polarization $P_{rem}$ $=6\,\mu A\,s\,cm^{-2}$ determined from the polarization hysteresis loop mentioned above. Thus, its reasonable to assume that the major contribution to the short circuit current density measured while heating originates from the decay of the ferroelectric polarization (and imprint). Annealing the sample above $T_C$ by waiting for 30 min at 130 °C, deletes the complete thermal and electrical history of the sample [3] [19]. Consequently, the current density measured in the cooling process equals approximately that of an un-poled sample (for details see FIG. 6.4 and especially FIG. 6.4 d)). FIG. 6.7 b) depicts $P$ for the complete heating and cooling cycle. The cooling processes are magnified in the inset.

Start in $+P_{rem}$: The short circuit current density j while heating discussed above differs significatly from that, which results if the heating process starts in $+P_{rem}$ at 30 °C. One would expect the following symmetry: $j_{start\ in\ -Prem}(T) = -j_{start\ in\ +Prem}(T)$. However an asymmetry is observed. To visualize the asymmetry, the orange dotted-dashed line which equals the on the time axis mirror imaged curve of $j_{start\ in\ +Prem}(T)$ is plotted into FIG. 6.7 a). It can be seen that $j_{start\ in\ -Prem} \approx -j_{start\ in\ +Prem}$ below 80 °C (dotted line), but above 80 °C (dashed line) the curves diverge. Thus, the

[18] In the negative remanent polarization state the vector of the ferroelectric polarization points towards the top electrode.
[19] see also section 5.2.3.

onset temperature for the asymmetric behavior equals the onset temperature (see section 2.3.8.2) of the DFE to PE phase transition. To the present moment no satisfactory explanation for the asymmetric behavior of $j$ regarding a start in $-P_{rem}$ and $+P_{rem}$ can be given, but it seems likely that compensation charges [15, 17, 20, 21, 92, 93] , polarization in the non-ferroelectric phase(s) [20, 21] and asymmetric electrode interfaces [104] and interphases [32] regarding top- and bottom side play a role, which will be reasoned in the following. Fedosov et al. [21] demonstrate experimentally and theoretically, that only that amount of ferroelectric polarization is stable at zero applied field, for which the depolarizing field in the ferroelectric (crystallites) is sufficiently compensated by compensation charges [20] and/or polarization in the non-ferroelectric phase [21]. In the ferroelectric to paraelectric transition temperature range both happens, the compensation charges are released from the polar ends of ferroelectric crystallites and the polarization in the non-ferroelectric phase decays. Assuming that the released compensation charges move towards the closest electrode for recombination results in a current which positively superimposes with the current due to the decay of the ferroelectric polarization. In contrast the current due to the decay of the polarization in the non-ferroelectric phase superimposes negatively [22] with the current due to the decay of the ferroelectric polarization. The compensation charges can be assumed to stick to the polar ends of ferroelectric crystallites, thus to the DFE phase. The onset temperature of their release might coincide with the onset temperature for the decay of the DFE phase which coincides with the onset temperature for the asymmetric behavior of $j_{start\ in\ -Prem}$ compared to $j_{start\ in\ +Prem}$. The temperature stability of $P_{rel}$ i.e. an polarization in the amorphous phase, is assumed to be at least 100 °C, since imprinting increases over time at this temperature as presented in section 5.5.

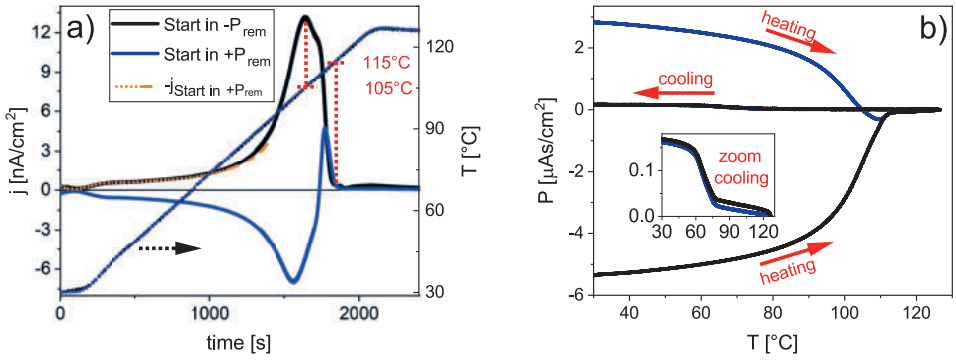


FIGURE 6.7: a) Short circuit current while heating starting at 30 °C in either $-P_{rem}$ or $+P_{rem}$. b) $P$ equals the current densities depicted in a) integrated respective to time.

Due to the sample preparation process, bottom- and top side electrode polymer interface and interphase differ. This is because the aluminum (Al) bottom electrode surface which faces towards the polymer film has during sample preparation for a certain time periode contact to free air. Additionally the polymer film and the bottom electrode are annealed in direct contact. In contrast, the top electrode is directly applied via thermal evaporation to the already annealed polymer film. Consequently

[20] FIG.3.1 on the right might serve as illustration. Compensation charges are to be confused with the compensation law.

[21] $P_{rel}$ is the consequence of such a polarization

[22] because $P_{rel}$ is anti-parallel to $P_{fe}$ in the New Imprint Model

it can be assumed that only at the bottom side exists an aluminum oxide layer [23]. Additionally at the bottom side exists an interphase, built by laying down H-C-F dipoles in the electrode adjacent layer [32]. The interface / interphase at the top-side is almost unexplored but electrical investigations with various electrode materials revealed that Al top electrodes deteriorate a ferroelectric polarization reversal process stronger than Al bottom electrodes [33], which implies an interphase at the top-side also. The exact role which play the interfaces and interphases is unclear, but interfaces and interphases are the only asymmetry in the sample which can to the present level of knowledge be imagined to cause the asymmetry of $j$ regarding a start in $-P_{rem}$ and $+P_{rem}$. Note, in section 7 an experimental method is presented, which could elucidate the presence and the role of interfaces and interphases in future investigations.

## 6.6 Poling and subsequent heating: Imprinting and pyroelectricity in the range 30 °C to 72 °C

Sample parameters and measurement conditions: The co-polymer film is prepared with $T_{anneal}$ =120 °C and is approximately 660 nm thick. The sample is initially de-aged above $T_C$, poled to $-P_{rem}$ with a pulse of 10 s duration and amplitude of 75 MV m$^{-1}$ at a temperature of 30 °C and then left in short circuited condition for $t_w = 1180$ s.

The short circuit current density $j$ is measured while passing through repeated heating cooling ramps. The temperature and $j$ are depicted in FIG. 6.8 a) as a function of time. The maximum temperature in the 1st, 2nd and 3rd heating-cooling cycle is 72 °C, which is according to section 6.7.1 below the onset temperature of the ferroelectric to paraelectric phase transition. Thus, all changes in the ferroelectric polarization brought about by a change in temperature are reversible and the associated current density $j_{pyro}$ can be assigned to pyroelectricity. $j_{pyro}$ is shown in FIG. 6.8 c). FIG. 6.8 d) demonstrates the proportionality [24] between $j \stackrel{!}{=} j_{pyro}$ and the heating rate in accordance to the definition of pyroelectricity as expressed by equation (2.5), whereas the proportionality factor equals here $-p_{pyro,3}$ [25].

FIG. 6.8 b) depicts $j$ as a function of the temperature. It can be seen that a certain current contribution is present only while first heating. FIG. 6.8 c) highlights this "irreversible" contribution to $j$, which is for now denoted as $j_{irrev}$. In the next sections it will be shown that $j_{irrev}$ can be identified as the imprinting current density $j_{rel}$ in a certain temperature range. A side note: the current experimental findings are discussed in the following section 6.6.1 on the basis of the New Imprint Model. The identification $j_{irrev}$=$j_{rel}$ fails when entering the ferroelectric to paraelectric transition temperature range as it is done in the 4th heating process, where the sample is heated to 119.5 °C $> T_C$. $j_{irrev}$ is in the 4th heating process above a certain temperature, which is determined in section 6.7.1, a composition of $j_{rel}$ and (among others, see section 6.5 for details) the current density associated to the irreversible decay of the ferroelectric polarization. Irreversible in the sense that the ferroelectric polarization is not recovered in the end of the temperature loop. Thus, by approaching $T > T_C$ in the 4th loop, the ferroelectric polarization decays completely and irreversibly and

[23] Al does form a 4 nm thick $Al_2O_3$ layer at ambient temperatures [98].

[24] The data in FIG. 6.8 d) is taken from the 4th heating process. Since $p_{pyro,3}$ depends on the temperature (see FIG. 6.11 and section 2.3.11) the temperature range was chosen narrow.

[25] The minus sign expresses that the system is in the negative remanent polarization state. In P(VDF-TrFE) the pyroelectric coefficient $p_{pyro,3}$ is negative (see FIG. 6.11 and section 2.3.11).

consequently $j$ while cooling is very low. $j$ while cooling from above $T_C$ is discussed in section 6.5.

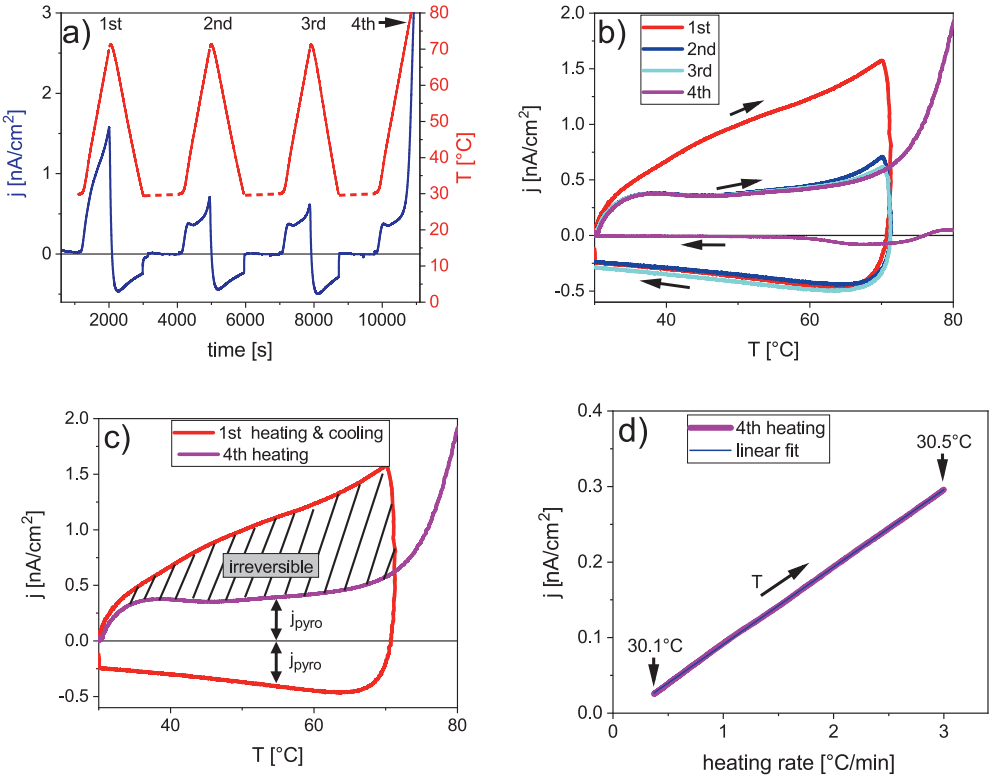


FIGURE 6.8: a)-c) Short circuit current densities and corresponding temperatures during subsequent heating-cooling cycles. d) Linearity of the current density associated to pyroelectricity as a function of the heating rate.

### 6.6.1 New Imprinting Model while thermal cycling far below $T_C$

The temperatures discussed here are below the onset temperature of the ferroelectric to paraelectric phase transition. The behavior of $j$ while thermal cycling in the temperature range between 30 °C to 72 °C shown in FIG. 6.8 a)-c) can be explained using the New Imprint Model. Lets assume that there are only two current contributions:

- The imprint related current density $j_{rel}$: The rd dipoles reorient only once. Then they remain in this (imprinted) position. Some rd reorient during $t_w$ at constant temperature (FIG. 6.9 a) -> b)). Others reorient in the first heating run (FIG. 6.9 b) -> c)). All rd with a relaxation time at 72 °C shorter than a few seconds, complete the reorientation process in the first heating run. Note, the relaxation time of rd decreases with increasing temperature, for details see section 6.9. During cooling and subsequent heating runs (FIG. 6.9 d) -> e)) only a few very slow rd reorientation processes proceed and consequently the amplitude of $j_{rel}$ is low.
- The pyroelectric current density $j_{pyro}$: This current density is linearly dependent on the heating rate (see equation (2.5)) and thus, flows while heating with same amplitude but in opposite direction as while cooling. $j_{pyro}$ is discussed in more detail in section 6.7.

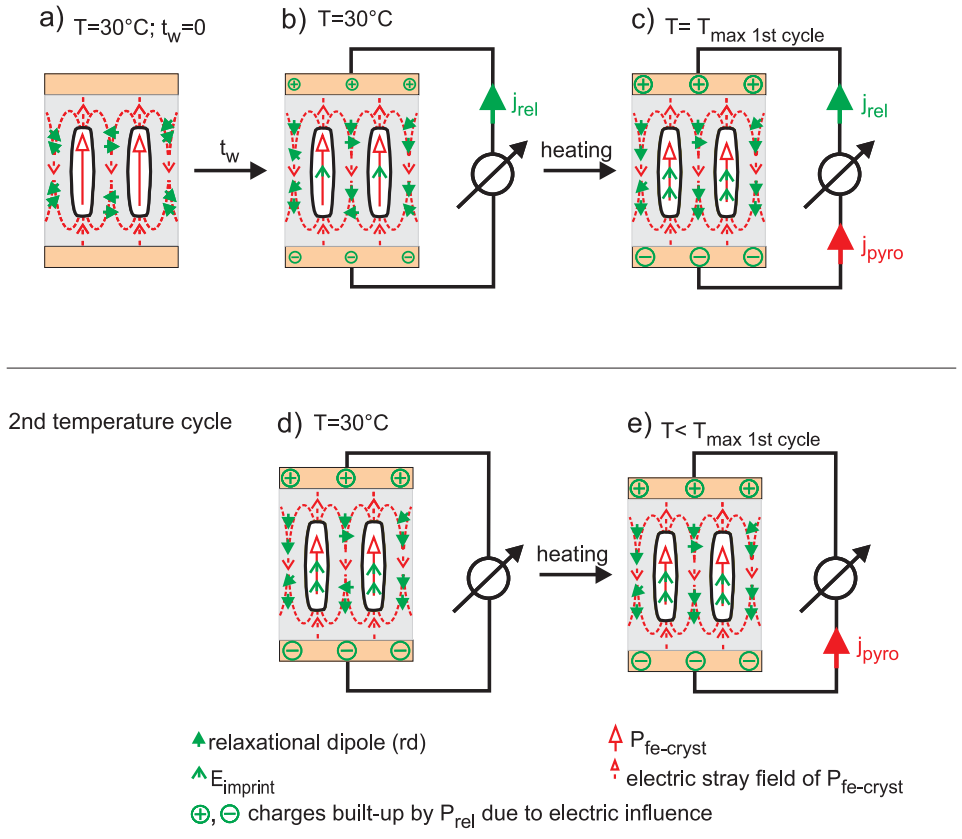


FIGURE 6.9: Illustration based on the New Imprint Model (see also section 3.3) to explain the behavior of $j$ while thermal cycling at temperatures below the ferroelectric to paraelectric phase transition with the New Imprint Model. Corresponding experimental data is presented in FIG. 6.8.

## 6.7 Poling and subsequent cooling: Imprinting and pyroelectricity in the range −25 °C to 80 °C

Sample parameters and measurement preconditions: The co-polymer film is prepared with $T_{anneal} = 120\,°C$ and is 660 nm thick. The sample is initially de-aged above $T_C$, poled to $-P_{rem}$ with a pulse of 10 s duration and amplitude of $75\,MV\,m^{-1}$ and then left in short circuit condition for $t_w = 1180\,s$ at the poling temperature of 10 °C.

The aim is here to extend the investigation from section 6.6: On the one hand the temperature stability of $P_{fe}$ [26] is investigated, thus determining the onset temperature of the ferroelectric to paraelectric phase transition, which is known to proceed over a broad temperature range (see section 6.5). On the other hand the behavior of $j_{irrev}$ [27] while heating and cooling is studied.
In FIG. 6.10 a), b) and c) $j$ is measured in cooling heating cycles, whereas the maximum temperature is subsequently increased (40 °C, 71 °C and 119 °C). The minimum temperature is always −30 °C. A cooling/heating rate of $1\,°C\,min^{-1}$ is used. The strong current response in the beginning of cooling processes is of pyroelectric nature and is a consequence of excessive cooling when the cooling system steps in. This excessive cooling stops the flow of $j_{irrev}$ immediately. While cooling and subsequent heating only $j_{pyro}$ flows in the short circuit provided that the temperature is sufficiently below the maximum temperature approached in a previous cooling-heating cycle. While heating $j_{irrev}$ increases by approaching this maximum temperature and its amplitude is high when exceeding this temperature. This behavior of $j_{irrev}$ can be understood on the basis of the New Imprint Model while thermal cycling as presented in section 6.6.1.

For the curve "new start 1. heating" in FIG. 6.10 d) the measurement is started anew under the same preconditions. The sample is this time directly heated up. As can be seen the "new start: 1. heating" curve overlaps piecewise with "2.heating"-, "4.heating"- and "6.heating"- curves. Thus, the process which generates $j_{irrev}$ pauses as long as the temperature is sufficiently below the maximum temperature approached in a previous cooling heating cycle.

The measurement is started again anew under the same preconditions. The sample is then heated to 75 °C and then cooled to 40 °C (not shown). The maximum temperature increases thereupon in subsequent heating-cooling-cycles (76.4 °C, 78 °C, 79.8 °C, 80 °C, 82 °C and 84 °C) in order to advance in small temperature steps towards and into the ferroelectric to paraelectric phase transition temperature range. The resulting short current densities are depicted in FIG. 6.10 e) along with two measurements which have already been depicted in FIG. 6.10 d). The temperatures at which $j$ is zero (or very close to zero) mark the start temperatures of the heating processes (FIG. 6.10 e)). The linear increase of $j_{pyro}$ in FIG. 6.10 e) can be seen extended to temperatures as high as around 73 °C. The red dashed line in FIG. 6.10 f) is a linear extrapolation ($T >$73 °C) of $j_{pyro}$. Subtracting the red dashed line from the curve labeled "new start 1. heating" yields $j_{irrev}$, which is depicted in FIG. 6.10 g). Integration of $j_{irrev}$ respective to time yields $P_{irrev}$ - $P^0_{irrev}$ depicted in FIG. 6.10 h), which will be discussed in detail in the following sections (section 6.8 ff).

[26] Recollect the relation between $p_{pyro,3}$ and the ferroelectric polarization described in section 2.3.11.
[27] In section 6.8 it will be shown that $j_{irrev} = j_{rel}$, at least in the temperature range 30 °C to 67 °C

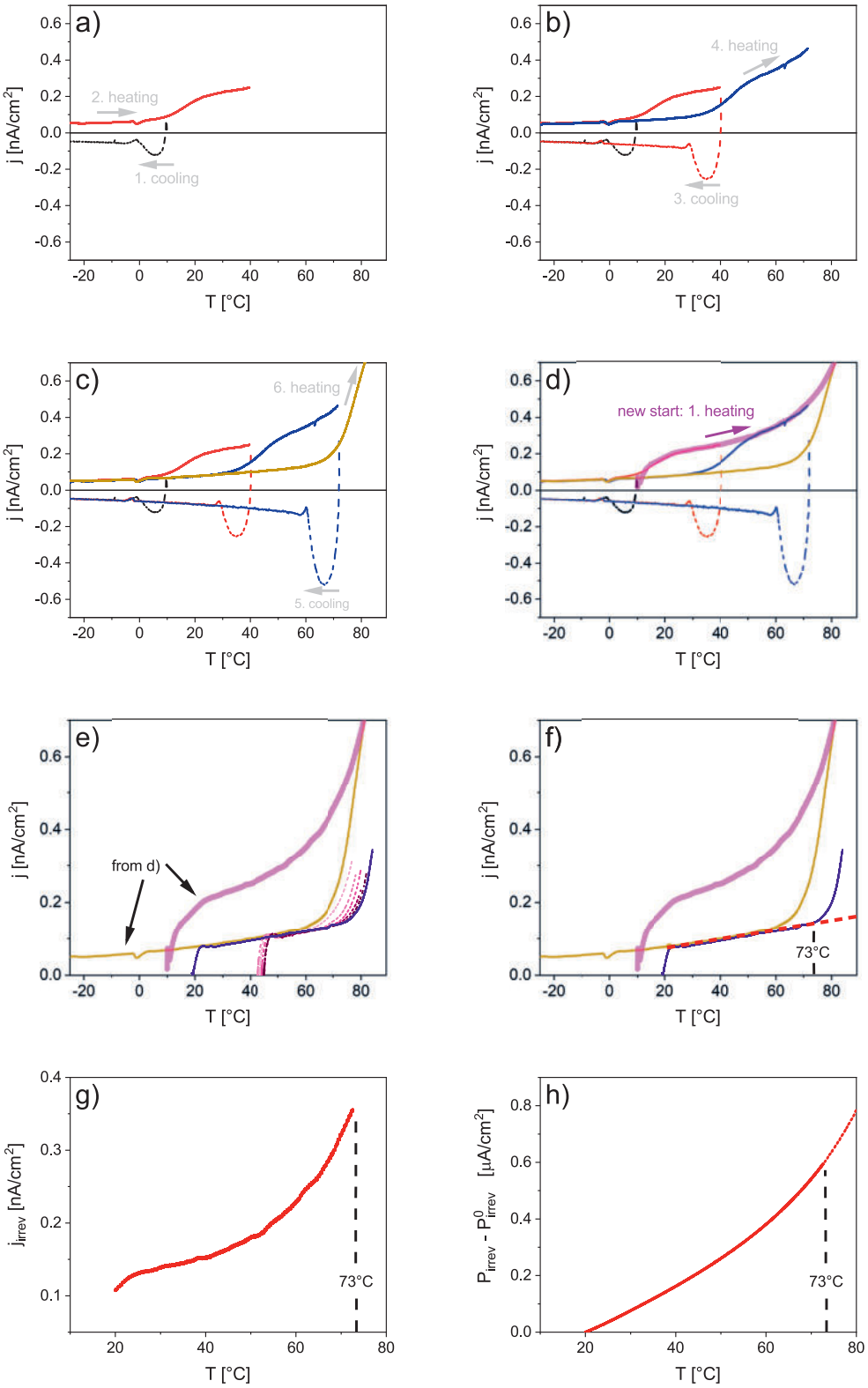


FIGURE 6.10: a)-f) Short circuit current during various cooling-heating cycles. g) Current resulting when subtracting the dashed line in f) from "new start: 1.heating". h) Integration of the curve in g) respective to time.

### 6.7.1 The pyroelectric coefficient and pyroelectric aging

The experimental pyroelectric coefficient $p_{pyro,3}(T)$ depicted in FIG. 6.11 is calculated from $j$ in FIG. 6.10, where $j$ can be identified as $j_{pyro}$, as discussed in section 6.7. $p_{pyro,3}(T)$ is given by multiplication of $j_{pyro}$ with the heating rate (see equation 2.5). $p_{pyro,3}(T)$ depends on the thermal history, as can be seen in FIG. 6.11. This is known in literature as pyroelectric aging [11, 20]. In the following it will be shown that imprint doesn't really impact on pyroelectric aging. It's rather presumed that pyroelectric aging is a consequence of the irreversible decay of the ferroelectric polarization when entering the ferroelectric to paraelectric phase transition temperature range.
In FIG. 6.11, $p_{pyro,3}(T)$ has declined after heating to 82.7 °C by around 5% (comparing values before and after at 50 °C). Such a decay in $p_{pyro,3}(T)$ is not observed in heating loops with cooler maximum temperatures, like when heating to 71 °C.
Equation (2.13) relates $p_{pyro,3}$ and $P_{rem}$ in a proportional manner. Referring to equation (5.17), the two major constituents to $P_{rem}$ are the imprint polarization $P_{rel}$ and the ferroelectric polarization $P_{fe}$. Thus, the change in $p_{pyro}$ related to pyroelectric aging is due to an increase in $P_{rel}$ and/or a (irreversible) decrease in $P_{fe}$ [28]. $P_{irrev}(T)$ in FIG. 6.10 h) can be interpreted as the decay in $P_{rem}$ when heating to a certain temperature T. Below the onset temperature of the ferroelectric to paraelectric phase transition ($\approx$ 80 °C, for details see section 2.3.8.2), the decay in $P_{rem}$ is most probably completely (see section 6.8) due to the building-up of $P_{rel}$, which increases by $P_{irrev}(71\,°C) - P_{irrev}(40\,°C) = 0.4\,\mu A\,s\,cm^{-2}$ when heating from 40 °C to 71 °C [29]. Reconsidering that $P_{rem}$ equals around $6\,\mu A\,s\,cm^{-2}$, a decrease by $0.4\,\mu A\,s\,cm^{-2}$ means a decay in $P_{rem}$ by 6.6%, which should equally be observed in $p_{pyro}$. However, the decay in $p_{pyro}$ is only around 1%, which is in the limit of noise. Consequently, $P_{rel}$ doesn't impact on pyroelectric aging. In contrast, heating to temperatures exceeding the onset temperature of the ferroelectric to paraelectric phase transition, results apparently in pyroelectric aging, as can be seen in the decay in $p_{pyro}$ when heating to 82.7 °C in FIG. 6.11. Thus, it can be concluded that pyroelectric aging is due to the irreversible decay of $P_{fe}$ that occurs in the ferroelectric to paraelectric phase transition temperature range.

[28] The decrease of $P_{fe}$ is two fold. The reversible part, that recovers in the end of a temperature loop, causes the pyroelectric current (see section 2.2). The other part doesn't recover in the end of a temperature loop. It is believed that this irreversible part displays a loss in alignment of the ferroelectric dipoles which occurs within the ferroelectric to paraelectric transition temperature range (see sections 6.2.3 to 6.5). (The dipole alignment can be reestablished by poling.)

[29] The short circuit current density while cooling equals approximately $j_{pyro}$. Thus, the increase in $P_{rel}$ happens for the most part while heating in a temperature loop such as from 40 °C to 71 °C and back to 40 °C. While cooling $P_{rel}$ remains almost constant (for details see section 6.7)

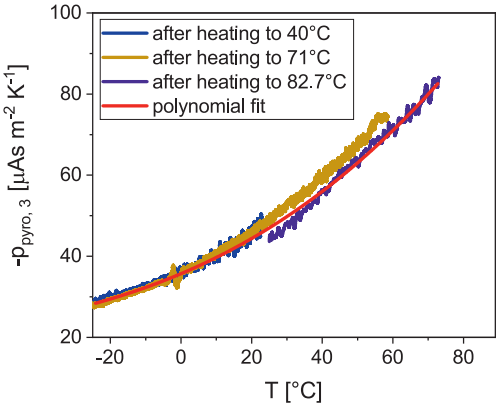


FIGURE 6.11: Pyroelectric coefficient (determined from FIG. 6.10).

## 6.8 Imprinting current ($j_{rel}$) while heating after imprinting at 30 °C

Sample parameters and measurement preconditions: The co-polymer film is prepared with $T_{anneal}$ = 135 °C and is 480 nm thick. The sample is initially de-aged above $T_C$ and then poled by traversing the polarization hysteresis three times with a frequency of 10 Hz and a maximum amplitude of the applied field of 94 MV m$^{-1}$. The sample is after poling in the negative remanent polarization state.

Directly after poling the sample is short circuited for various time periods $t_w$ and then heated up with a rate of 3 °C min$^{-1}$. The temperature at poling and waiting is 30 °C. FIG. 6.12 illustrates the temperature as a function of time, in the course of the $j$ measurement. FIG. 6.12 a) shows the time periods of deaging, poling, waiting and heating up with the start of the $j$ measurement. FIG. 6.12 b) shows the complete temperature cycle (heating and cooling).
FIG. 6.13 a) depicts the short circuit current densities $j$ measured during the complete temperature cycle. Integration of the short circuit current densities respective to time throughout the whole heating run yields around 5.8 µA s cm$^{-2}$, which equals approximately the remanent polarization $P_{rem}$ =6.25 µA s cm$^{-2}$ determined from the hysteresis of initial poling. The cooling curves do not markedly differ for different $t_w$ and correspond approximately to those presented in FIG. 6.4 a). FIG. 6.13 b) and c) depict the short circuit current densities while heating for a limited temperature range as a function of temperature and time, respectively. The $j$ - curves in FIG. 6.13 b) and c) will in the following be addressed as $j_{heating}$ curves. The dashed line in FIG. 6.13 b) denoted as $j_{pyro}$ is an estimation for the pyroelectric current density assuming a constant heating rate of 3 °C min$^{-1}$ [30]. In the temperature range 30 °C to 36 °C, which is in the beginning of the heating processes, the heating rate isn't stable (region with gray background in FIG. 6.13 b)).

[30]The data for the pyroelectric current density is calculated from the dashed line in FIG. 6.10 f) via multiplication by three to suit the present heating rate.

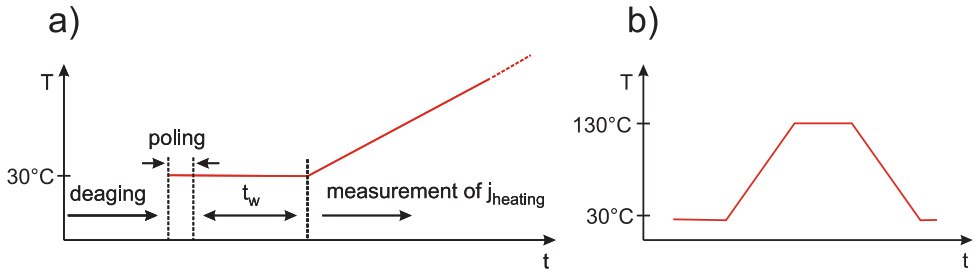


FIGURE 6.12: Schema of the experiment. Temperature $T$ versus time $t$. a) Start of the measurement with details. b) Complete temperature cycle.

Assigning $j_{irrev}$ to $j_{rel}$ in the temperature range 30 °C to 67 °C: In FIG. 6.13 b) and c)it can be seen, that the longer the initial waiting time $t_w$ the less current flows in the beginning of the heating process. This behavior was also observed by another research group investigating imprinting [60, 61]. Their measurements were however polluted by the bg current [31]. The dashed line in FIG. 6.13 b) shows the pyroelectric contribution to $j_{heating}$. The other contribution to $j_{heating}$ named $j_{irrev}$ in sections 6.6 and 6.7 will be now identified as the imprinting current density $j_{rel}$ in the temperature range 30 °C to 67 °C [32], as will be reasoned in the following on the basis of the New Imprint Model [33]. $j_{rel}$ at constant temperature is discussed in section 5.9.1. While heating from 30 °C towards higher temperature the rd relaxation times shorten continuously [34]. The temperature at which $j_{heating}$ lifts clearly off the $j_{pyro}$ base line is indicative for a shortening of the relaxation time, which had been $t_w$ at 30 °C, to the minutes or seconds range. In FIG. 6.13 b) and c) it can be observed that, with increasing temperature and depending on $t_w$ one $j_{heating}$ curve after another merges into a single curve. Eventually at 67 °C this single curve includes all curves. It is thereof concluded (with respect to the New Imprint Model), that above 67 °C and for each case depicted in FIG. 6.13 b), differing in $t_w$, the same amount of rd reorientation processes proceed, the same amount of rd have already aligned with the stray fields of $P_{fe-cryst}$ and the same $P_{rel}$ and $E_{imprint}$ are present. To check if really the same imprint is present at a temperature of 67 °C (and above), the same experiment is conducted again (with similar $t_w$ values), but this time the heating processes are stopped at 67 °C, the sample is cooled back to 30 °C (imprinting stops while cooling and imprint is frozen in, for details see section 6.7) and the imprint state is determined: A ferroelectric polarization hysteresis loop is subsequently traversed three times (see FIG. 6.13 f)). The values of $E_c$ that is passed first [35] are quasi identical for different initial $t_w$ (see FIG. 6.13 e)). Thus, indeed the same $E_{imprint}$ is present before the hysteresis is traversed. Thus, imprinting which takes days [36] at 30 °C, takes seconds or minutes at a temperature of 67 °C.
Integration of $j_{heating}$ respective to time in the limits of the two dashed vertical lines (at 250 s and 910 s) in FIG. 6.13 c), yield the values of $P_{heating}$ at 67 °C depicted in FIG. 6.13 d). The data points in FIG. 6.13 d) differ by the amount of $P_{rel}$ built-up during $t_w$ at constant temperature. The linear relationship between $P_{rel}$ and $t_w$ can be seen in

[31] The bg (background) current is discussed in section 6.2.1.
[32] Within this temperature range no significant pyroelectric aging is detected (see section 6.7.1) and thus the ferroelectric polarization ($P_{fe}$) recovers in the end of a temperature loop.
[33] Details on the New Imprint Model are presented in section 3.3.
[34] for details see section 6.9.3
[35] The $E_c$ that is passed first reflects the imprint state as discussed in section 5.1.
[36] $t_w$ =430 620 s equal approximately 5 days

FIG. 6.13 d) [37] as well as in section 5.9 where $P_{rel}(t_w)$ is investigated at constant temperature. The slope $-\Delta P'$ in FIG. 6.13 d) equals $-62\,\mathrm{nA\,s\,cm^{-2}}$ the equivalent value presented in section 5.9 equals only 80% of the value $\Delta P'$. To the present moment the best explanation for the 20% error is the error made when assuming $\alpha$ equals 1.

In summary there are three key observations which substantiate that $j_{irrev}$ equals $j_{rel}$ in the temperature range 30 °C to 67 °C:

1. The longer the waiting time, the smaller the amplitude of $j_{irrev}$. We presume that $j_{irrev} = 0$ for $t_w \to \infty$: The $j_{heating}$ curve in FIG. 6.13 b) is reduced to the $j_{pyro}$ base line when waiting long enough.
2. $j_{irrev}$ is related to imprinting effects ($E_c$=const. in FIG. 6.13 e)).
3. $\Delta P = \Delta P'$ : The current which flows during $t_w$ is missing in $j_{heating}$.

$$\Rightarrow \boxed{j_{irrev} = j_{rel} \qquad \text{(at least for: } 30\,^{\circ}\mathrm{C} < \mathrm{T} < 67\,^{\circ}\mathrm{C})} \tag{6.3}$$

In summary the short circuit current density while heating ($j_{heating}$) in the temperature range 30 °C to 67 °C is composed of $j_{rel}$ and $j_{pyro}$, which are associated to imprinting and pyroelectricity, respectively. Besides, it was also shown in this section that imprinting speeds up vigorously with increasing temperature, which is further investigated in section 6.9. It is believed that $j_{heating}$ is basically the sum of $j_{rel}$ and $j_{pyro}$ also at cooler temperatures as 30 °C, since there is no evidence of anything obviously contradicting that. Note, the data presented in section 6.7 had already been discussed on the basis of these conclusions.

[37] The first point in FIG. 6.13 at $t_w = 240\,\mathrm{s}$, doesn't strictly lie on the straight line, which is probably a consequence of an inaccuracy in $t_w$ caused by the non constant heating rate in the beginning of the heating processes.

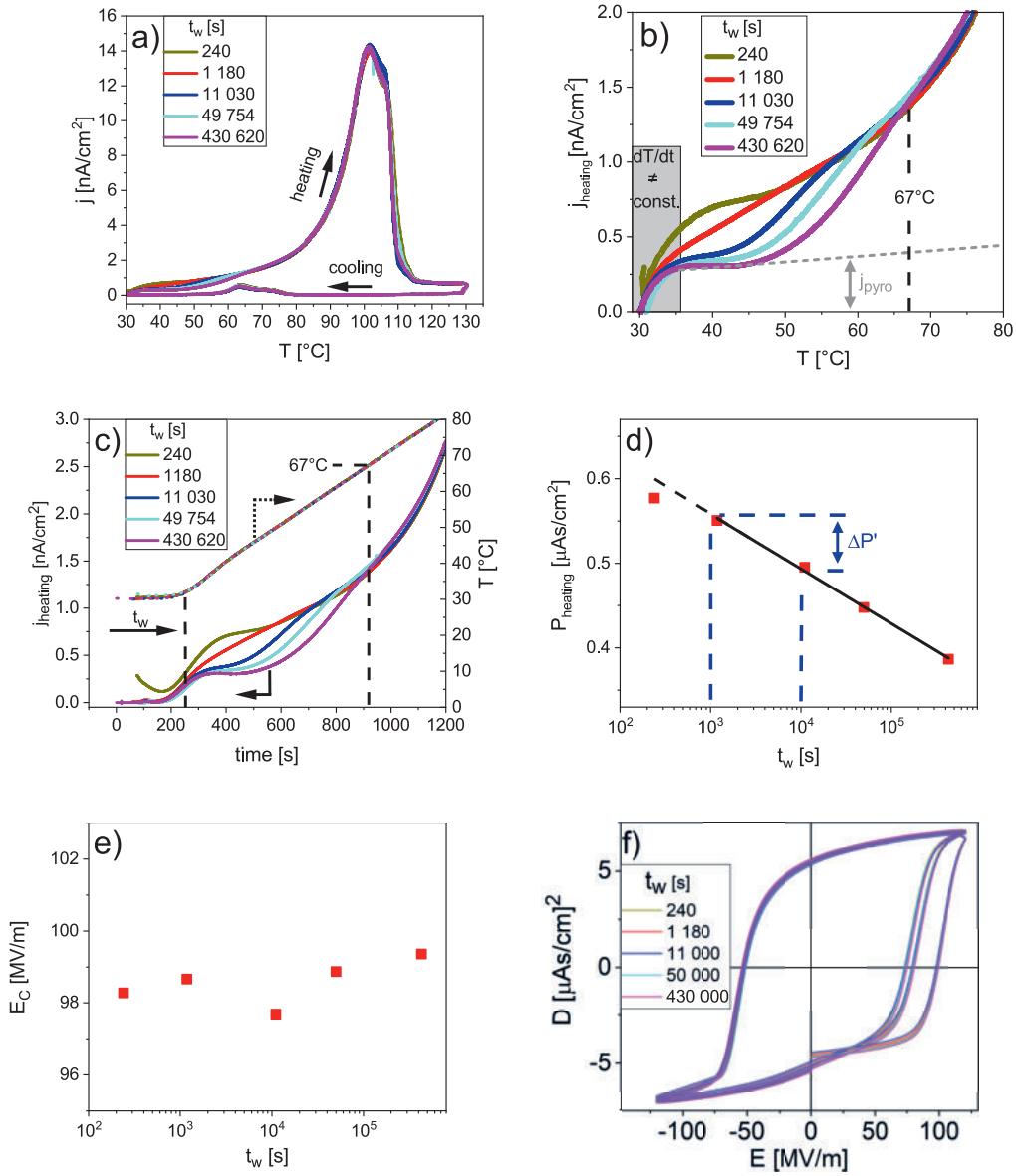


FIGURE 6.13: a) - c) Short circuit current densities measured in heating-cooling cycles. Before the cycles it is waited various time periods ($t_w$). d) Respective to time integrated current densities while heating in the limits: time at the start of the heating process, time when reaching 67 °C. e) Coercive field $E_c$ measured at 30 °C after heating to 67 °C. Ferroelectric polarization hysteresis loops measured at 30 °C after heating to 67 °C - $E_c$ values in e) are gained from these loops.

### 6.8.1 Detailed comparison with section 5.9

In FIG. 6.14 the remanent polarization $P_{rem}(t_w)$ from section 5.9 is plotted against $P_{heating}(t_w)$ from the previous section 6.8 at specific times $t_w$. $P_{rem}(t_w)$ decays during $t_w$ due to the build up of $P_{rel}(t_w)$, which is accompanied by the flow of $j_{rel}(t_w)$. The aim is here to show that, $P_{rel}(t_w)$ is that part of polarization that is missing in $P_{heating}(t_w)$ by waiting a time period $t_w$ at constant temperature of 30 °C before heating up.

FIG. 6.14 can be understood as follows. If the points lay on a 45° straight, then the polarizations on the x and y axis changed by the same amount by waiting a time period $t_w$. FIG. 6.14 b) shows the values of FIG. 6.14 a) with respect to the reference value found at $t_w$ =240 s. Since the points, in both graphs, lay approximately on the 45° straight it can be concluded, that $P_{heating}$ is reduced by $P_{rel}(t_w)$ when waiting $t_w$ before heating up. In principle that match-up was already demonstrated in the previous section by pointing out that $\Delta P \approx \Delta P'$. In the next section it will be shown that $j_{rel} \sim t_w^{-1}$ is not only found at 30 °C but also at other temperatures. That can be exploited to calculate $j_{heating}$ and finally to determine the factual temperature dependence of imprinting related dipole relaxation.

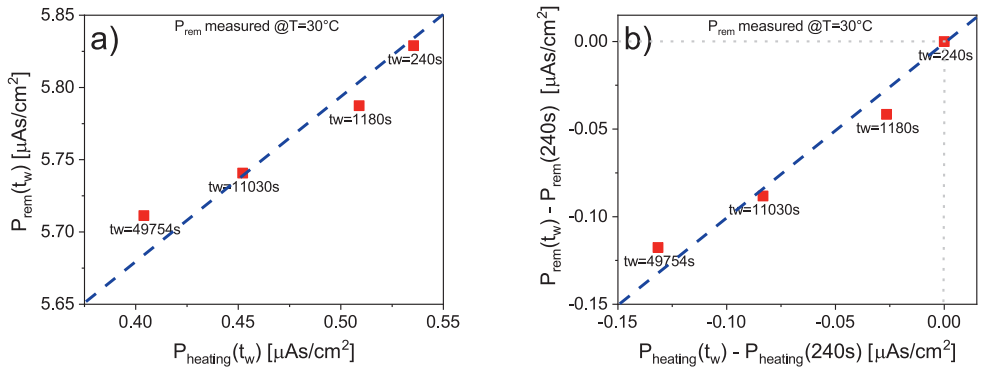


FIGURE 6.14: Comparing the polarization $P_{rem}(t_w)$ with the polarization $P_{heating}(t_w)$. Both polarizations change by $t_w$ due to the build up of $P_{rel}(t_w)$. The 45° straight symbolizes equality in change of $P_{rem}(t_w)$ and $P_{rem}(t_w)$ by waiting a time period $t_w$.

## 6.9 Calculation of the current associated to imprinting ($j_{rel}$) while heating

The aim in this section is to calculate $j_{heating}$. The model experimental result is presented in FIG. 6.13 b). As reasoned in section 6.8, $j_{heating}$ exhibits two contributions. These are the imprinting current density $j_{rel}$ and the pyroelectric current density $j_{pyro}$. The latter is estimated from the experimental pyroelectric coefficient. The calculation of the $j_{rel}$ is described in the following.

### 6.9.1 Simplifications in g(W) when calculating $j_{rel}$

The imprinting current density $j_{rel}$ is calculated based on relaxation kinetics. Based on the experimental observation that $j_{rel}$ follows experimentally approximately the law $j_{rel} = A \cdot t_w^{-\alpha}$, with $\alpha \approx 1$, at any constant temperature in the range $-20\,^{\circ}\mathrm{C}$ to $70\,^{\circ}\mathrm{C}$, see FIG. 6.15 a) [38], a distribution density $g(W)$ of energy barriers $W$ as depicted in FIG. 6.15 b) is assumed. In section 3.4 it is shown that a distribution of energy barriers such as $g(W,T) = g_0$ yields current densities $j_{rel} \sim t_w^{-1}$ across a limited temperature and time range . These temperature and time limits are known to be wide (see section 5.8) but their value is yet unknown. Thus, the limits $W_1$ and $W_n$ are chosen so wide, that a further increase in $W_n$ or a decrease in $W_1$ wouldn't noticeable change the result. In other words, there are ongoing relaxation processes for all temperatures and times investigated and the calculated $j_{rel}$ is at constant temperature proportional to $t_w^{-1}$. In the numerical calculation, neighboring values $W_i$ and $W_{i+1}$ differ by $\Delta W$ =0.01 eV. A further decrease in $\Delta W$ does not result in any noticeable difference in the calculated $j_{rel}$.

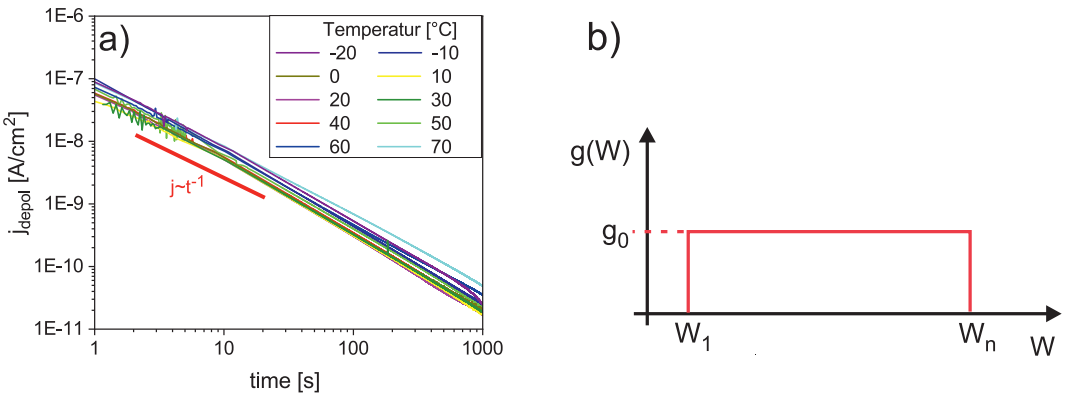


FIGURE 6.15: a) Current density ($j_{depol}$) at various constant temperatures. b) Energy barrier distribution function g(W) used in the calculation of $j_{rel}$. [39]

[38] For times exceeding the pulse duration of 10 s, it can be assumed that $j_{depol}$ and the time in FIG. 6.15 equal $j_{rel}$ and $t_w$, respectively, for details see section 5.13.

[39] $j_{depol}$ is measured after application of a ferroelectric switching pulse of 10 s duration and amplitude of 103 MV m$^{-1}$.

### 6.9.2 Calculation of $j_{rel}$

The starting point for the calculation of $j_{rel}$ are Debye-like relaxation processes. An individual polarization process $p_i$ relaxes with an individual relaxation time $\tau_i$. The $p_i$ are solutions of the differential equation [40]:

$$\tau_i(T(t))\frac{dp_i(t)}{dt} + p_i(t) = p_0 \tag{6.4}$$

For the used heating ramp, the temperature $T(t)$ changes linear in time. $p_0$ equals the polarization in the limit of infinite time. $p_0$ is assumed to be a constant in the considered temperature range [41]. The sum of all $p_i$ at any moment in time equals the calculated relaxational polarization $P_{rel}$. Differentiation of $P_{rel}$ respective to time yields the calculated $j_{rel}$.

Scaling the calculated $j_{rel}$ and $P_{rel}$: At constant temperature, the calculated $j_{rel}$ curves follow the law $j_{rel} = A(T) \cdot t_w^{-1}$ at all considered times and temperatures. Experimentally that is approximately found also (see FIG. 6.15). The experimental value of $A$ at 30 °C and $t_w$ =100 s (see FIG. 6.16) is taken as input for the calculation of $j_{rel}$ [42].

Numerical calculation method: The relaxation times $\tau_i$ are dependent on the temperature (see sections 6.9.3 and 6.9.4) and the temperature is dependent on time (due to the heating ramp). Besides, the heating process starts after waiting for a duration of $t_w$ at constant temperature. Consequently, the individual polarizations $p_i$ don't equal zero in the beginning of the heating process. To this end equation (6.4) is solved numerically, with the aid of a 4th order Runge Kutta algorithm.

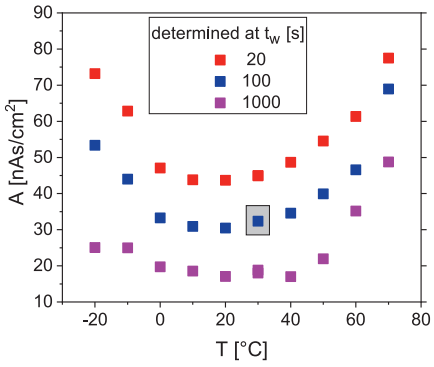


FIGURE 6.16: A(T) determined from $j_{depol}$, shown in FIG. 6.15, via $A(T) = j_{depol}(T, t_w) \cdot t_w$

.

[40] Equation (6.4) corresponds to equation (3.8), whereas $\tau_i$, $p_i$ and $p_0$ and are discrete in contrast to $\frac{1}{v}$, $dP_{rel}$ and $dP_{rel,0}$.

[41] A more elaborate calculation would consider that $p_0$ is dependent on temperature.

[42] $A$, $\Delta P$ (see section 5.9) and $\Delta P'$ (see section 6.8) are related. Using equation (5.14) and $j_{rel} = A \cdot t_w^{-1}$ yields for $\log(t_w/t_0)$ = 1 (waiting for one decade):

$$\Delta P' = \Delta P = A \cdot \underbrace{\log\left(\frac{t_w}{t_0}\right)}_{=1} \cdot (\log(e))^{-1} = 74.5\,\mathrm{nA\,s\,cm^{-2}} \tag{6.5}$$

where $A(t_w$ =100 s, $T$ = 30 °C) = 3.23 nA s cm$^{-2}$ and e is the Euler's number. $\Delta P'$ is also seen in FIG. 6.17 e).

### 6.9.3 Results using the compensation law

A good match between calculated and experimental $j_{heating}$ curves in the temperature range 30 °C to 80 °C is found if $\tau_i(T)$ obeys the compensation law, presented in equation (6.6).

$$\tau_i(T) = \tau_c \exp\left[\frac{W_i}{k_B}\left(\frac{1}{T} - \frac{1}{T'_C}\right)\right] \tag{6.6}$$

$\tau_c$ and $T'_C$ are a time constant and the Compensation Temperature [43], respectively [112]. Both, $\tau_c$ and $T'_C$ are used as fitting parameter. FIG. 6.17 a) depicts $j_{rel}$ calculated for the best fitting parameters $\tau_c$ =3 × 10$^{-4}$ s and $T'_C$ =381 K≈ 108 °C. The pyroelectric current density $j_{pyro}$ is determined from the straight dashed line shown in FIG. 6.10 f) via multiplication of a factor in order to adjust to the present heating rate. $j_{pyro}$ is depicted in FIG. 6.17 b). The sum of the calculated $j_{rel}$ and $j_{pyro}$ is depicted in FIG. 6.17 c) along with the experimental $j_{heating}$ curves taken from FIG. 6.13 b). The calculated curves fit well to the experimental curves up to temperatures as high as 90 °C (see inset in FIG. 6.17 c)). FIG. 6.17 d) depicts the calculated relaxational polarization that builds up while heating as function of the temperature relative to the value of $P_{rel}$ at $t_w$=240 s and 30 °C. As has experimentally already been deduced in section 6.8, at temperatures exceeding 67 °C the same $P_{rel}$ is present for different values of $t_w \leq$ 430 620 s. The linear dependence of $P_{heating}$ on $\log(t_w)$ originates from the fact that $P_{rel}$ exhibits a $\log(t_w)$ dependence at constant temperature. In conclusion, calculated and experimental $j_{heating}$ match quite well and the experimentally determined characteristics of imprinting while heating presented and discussed in section 6.8 could also be reproduced by the calculation. Note, only for temperatures in the range 30 °C to 71 °C (see section 6.7.1) it has been shown that pyroelectricity and imprinting are the only contributors to $j_{heating}$.

[43] The definition of the Curie Temperature $T'_C$ in the compensation law doesn't coincide with the definition of the Curie Temperature $T_C$ given in section 2.1

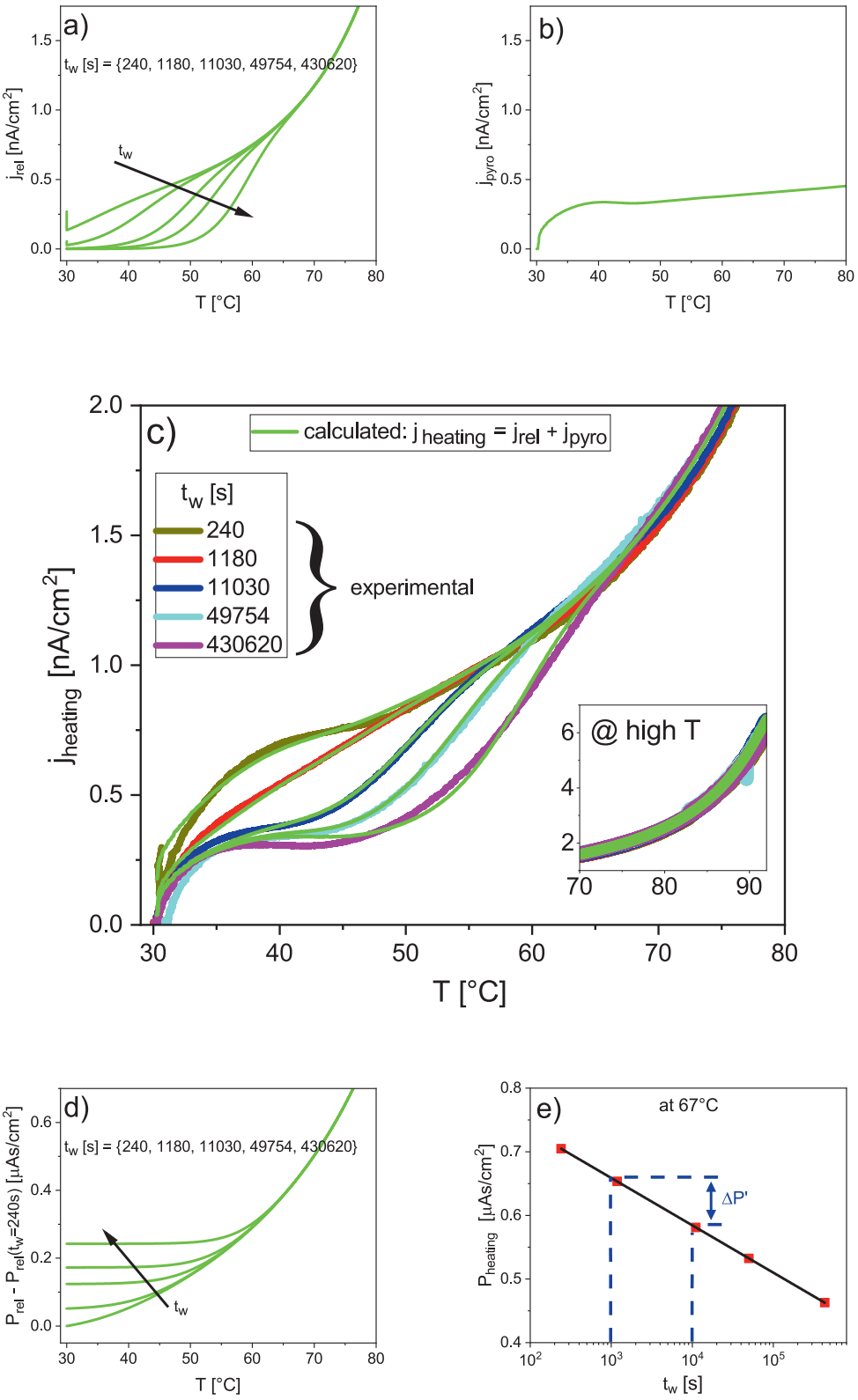


FIGURE 6.17: Calculation results using for $\tau_i$ the compensation law. a) Calculated $j_{rel}$ while heating. b) Pyroelectric current density. c) Comparison of experimental and calculated short circuit current density while heating. d) Built-up $P_{rel}$ respective to the value at $t_w$ =240 s. e) Integral of calculated $j_{heating}$ respective to time, in the limits time at the start of the heating process and time at 67 °C.

### 6.9.4 Results using the Vogel-Tammann-Fulcher (VTF) law and Arrhenius law

Again equation (6.4) is solved, but in contrast to section 6.9.3 $\tau_i$ follows here either the Arrhenius law (equation (6.7)) or the VTF law (equation (6.8)).

$$\tau_i = \tau_{0,Arrh} \cdot \exp\left[\frac{W_i}{k_B T}\right] \tag{6.7}$$

$$\tau_i = \tau_{0,VTF} \cdot \exp\left[\frac{W_i}{k_B (T - T_{VTF})}\right] \tag{6.8}$$

Here, $\tau_{0,Arrh}$, $\tau_{0,VTF}$ and $T_{VTF}$ are constants, which are used as fitting parameters. Best fit parameters are determined as such that the calculated $j_{rel}$ curves lift off from the zero line at that temperature at which the experimental $j_{heating}$ curves (see FIG. 6.13 b)) lift off from the pyroelectric current density base line. FIG. 6.18 a) and b) depict calculated $j_{rel}$ curves for best fitting parameters, whereas for $\tau_{0,Arrh}$ a parameter study is presented in a). Best fit parameters are $\tau_{0,VTF}$ =$1 \times 10^{-10}$ s, $T_{VTF}$ =215 K [44] and $\tau_{0,Arrh}$ =$1 \times 10^{-41}$ s [45]. The $j_{rel}$ curves for Arrhenius- and VTF law are very similar (see FIG. 6.18 b)), which is surprising because their individual polarization processes $p_i(t)$ differ (not shown). FIG. 6.18 c) and d) compares experimental and calculated $j_{heating}$ curves. Calculated $P_{rel}(T)$ curves are depicted in FIG. 6.18 e) and f). Again all curves of $P_{rel}(T)$ collapse above 67 °C to a single curve (see also section 6.9.3). Integration of the calculated $j_{heating}$ respective to time in the limits time in the beginning of the heating process and time at 67 °C yields $P_{heating}$ presented in FIG. 6.18 g) and h)). The experimentally observed linear dependence of $P_{heating}$ on the logarithm of $t_w$ is observed, as it is also observed when using for $\tau_i$ the compensation law.
In summary, it is unquestionable that the calculated $j_{heating}$ curves presented in section 6.9.3 fit better to the experimental $j_{heating}$ curves than those presented in this section in the temperature range 30 °C to 71 °C. Still, the calculated $j_{heating}$ curves presented here feature some to imprinting associated characteristics which were discussed in section 6.8. It is concluded that one could probably compose the calculated $j_{heating}$ curves of contributions which originate from relaxation processes governed by the Arrhenius-, VTF- and compensation law to achieve a good fit to the experimental $j_{heating}$ curves at temperatures below 50 °C. In the next section, the matter is further elucidated by investigating short circuit current densities over a wider temperature range.

[44] Note, similar values for these fitting parameteres are repoted in literature [5].

[45] A value of $\tau_0$ =$1 \times 10^{-41}$ s has no physical sense, but similar values for $\tau_0$ are observed also in other polymers [89, 114].

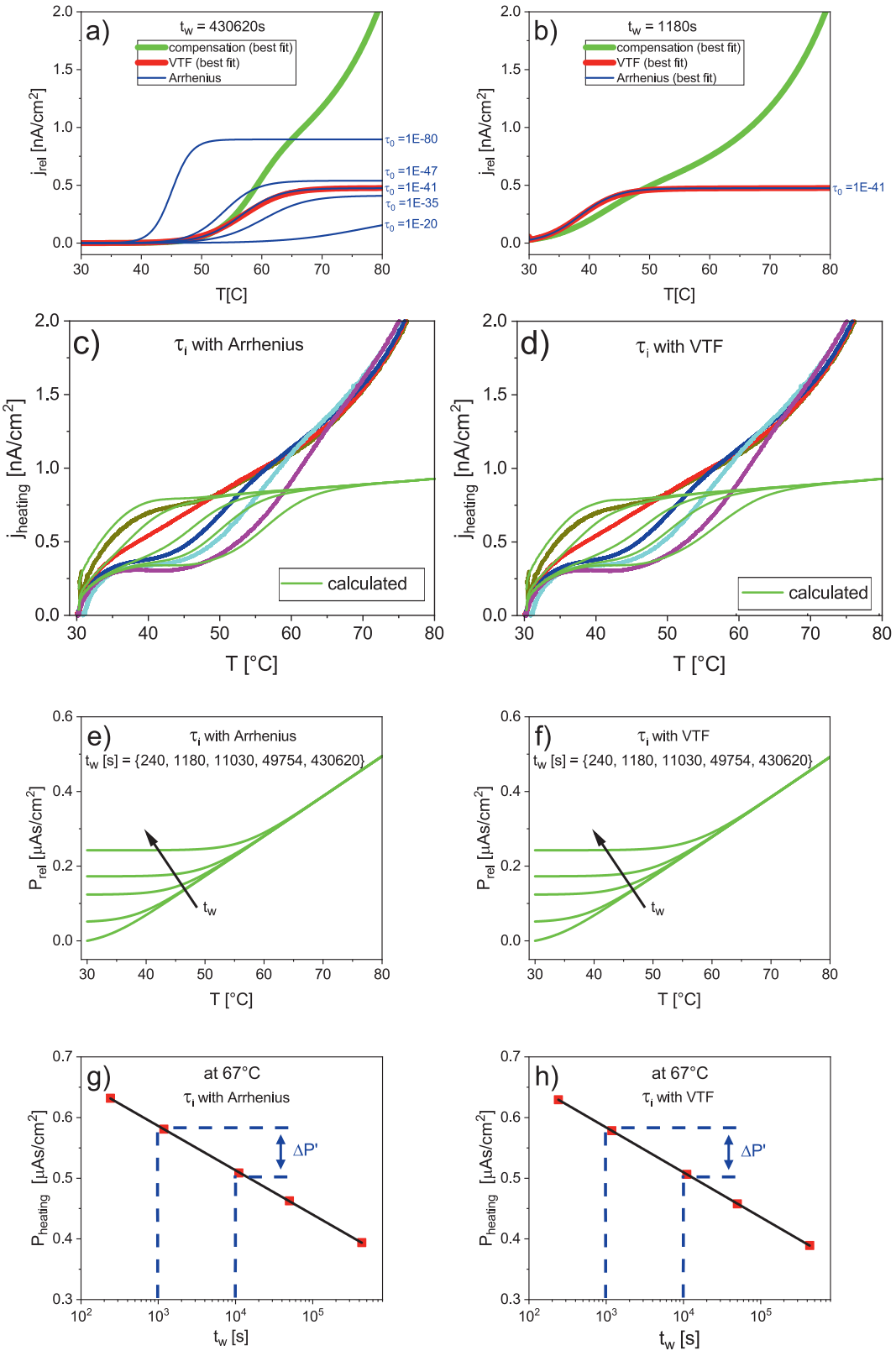


FIGURE 6.18: Calculation results using for $\tau_i$ Arrhenius- and VTF law. a) and b) Comparison of $j_{rel}$ calculated by using compensation- , VTF- , and Arrhenius law. c) and d) Comparison of the experimental (see also FIG.6.17 c) and FIG.6.13 b)) and calculated (with best fitting parameters) $j_{heating}$ curves. e) and f) Calculated built-up $P_{rel}$. e) and f) Respective to time integrated $j_{heating}$ in the limits: time at the beginning of the heating run and time when reaching 67 °C.

### 6.9.5 $j_{rel}$ while heating, for different start temperatures

Sample parameters and measurement (pre-)conditions: The co-polymer film is prepared with $T_{anneal} = 120\,°C$ and is 660 nm thick. The sample is initially de-aged above $T_C$ and then poled with a pulse of 10 s duration and amplitude of $75\,MV\,m^{-1}$ at various temperatures between $-10\,°C$ to $60\,°C$. After poling the sample is short circuited for a duration $t_w = 1180\,s$ at the poling temperature. Thereafter the sample is heated with a rate of $3\,°C\,min^{-1}$ and the short circuit current density $j_{heating}$ is measured.

FIG. 6.20 a) depicts the experimental $j_{heating}$ curves. In section 6.8 it is shown, that the calculated $j_{heating}$ matches well to experimental $j_{heating}$ in the temperature range 30 °C to 71 °C. The aim is here to calculate $j_{heating}$ additionally to cooler temperatures. For the calculation it is assumed that $j_{heating}$ is composed solely of $j_{pyro}$ and $j_{rel}$ also in the broader temperature range $-20\,°C$ to $80\,°C$, as indicated by the results presented section 6.7.
Details on the calculation of $j_{heating}$: $j_{pyro}$ is calculated from the polynomial fit to the pyroelectric coefficient given in FIG. 6.11 multiplied with the present heating rate. $j_{rel}$ is calculated as explained in section 6.9.3 and 6.9.4 using best fit parameters stated therein. Here, the experimental heating rate is used. and the input $\Delta P'$ equals $64\,nA\,s\,cm^{-2}$.
Discussion: The calculated $j_{heating}$ curves fit to the experimental $j_{heating}$ curves in the high temperature regime presented in FIG. 6.20 b), if $\tau_i$ follows the compensation law. Starting the experiment at lower temperatures and using the same calculation method, no good fit can be achieved as presented in FIG. 6.20 c). Changing the calculation method so that $\tau_i$ follows an Arrhenius - or a VTF temperature dependence than a good fit between calculated $j_{heating}$ and experimental $j_{heating}$ is found at low temperatures (see FIG. 6.20 d) and FIG. 6.20 e)), but no good fit can be achieved at high temperatures.
Conclusion: From the results of the calculation presented here, in section 6.9.3 and 6.9.4 it can be concluded that imprinting related polarization relaxation processes follow a VFT- (or an Arrhenius-) behavior at low temperatures, a compensation temperature dependence at high temperatures and at intermediate temperatures both laws can be applied.
A final note: In FIG. 6.20 a) in can be seen that $j_{heating}$ tends to be the more decreased at high temperatures the cooler the start temperature. The reason therefore is not well investigated but it is assumed that it is a consequence of the initial poling process, which is performed at different temperatures. Poling at a temperature as cool as $-20\,°C$ results in lower ferroelectricity than poling at a temperature as high as $60\,°C$ for a constant maximum amplitude of the applied poling field [70]. Consequently, the calculated $j_{heating}$ curves using the compensation law do not fit to the experimental curves in the high temperature region in FIG. 6.20 d) and FIG. 6.20 e).

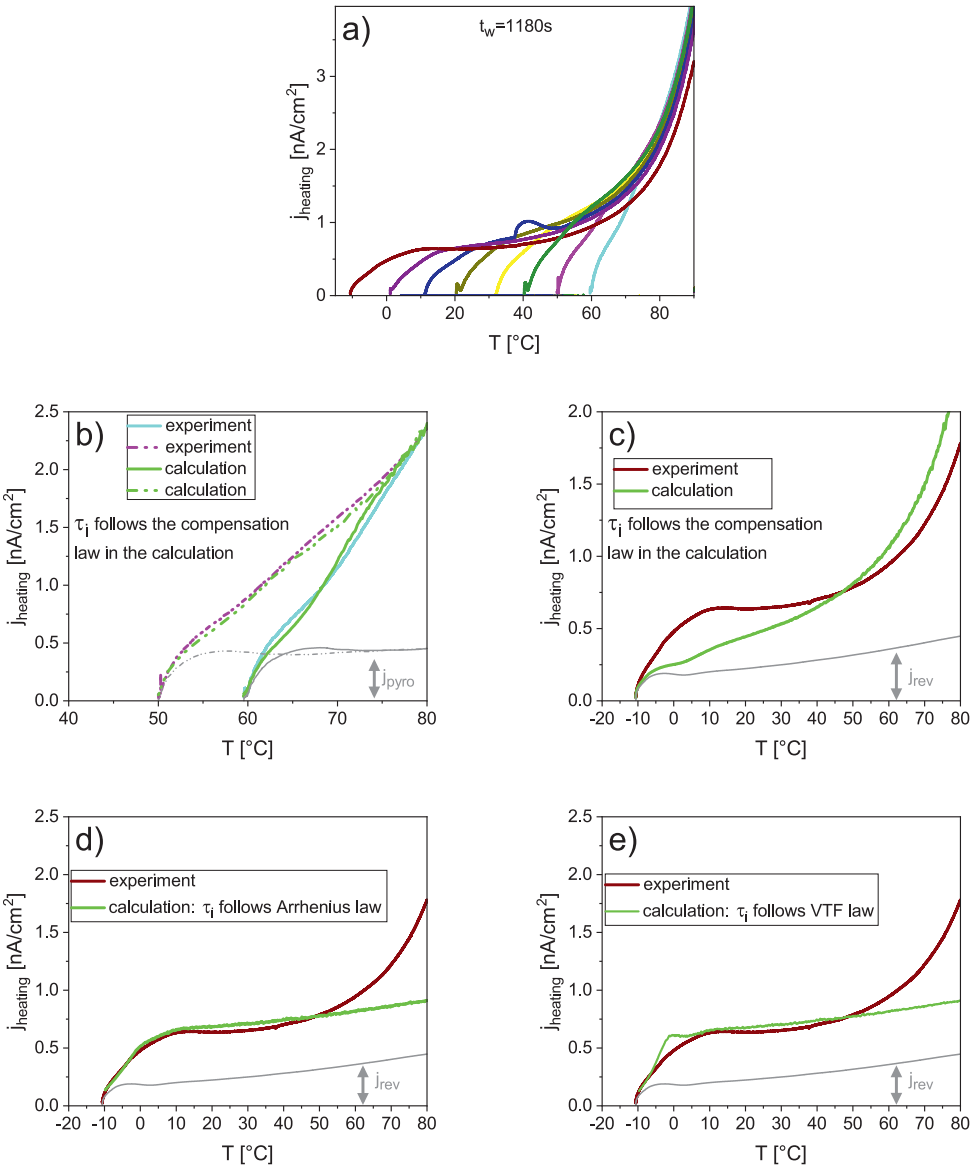


FIGURE 6.19: Short circuit current density ($j_{heating}$) while heating with constant rate. a) Experimental $j_{heating}$. b) and c) Comparison of experimental and calculated $j_{heating}$ curves, at high and low temperatures, respectively, using in the calculation the compensation law. d) and e) Comparison of experimental and calculated $j_{heating}$ curves in the low temperature range, using in the calculation the Arrhenius- and the VTF law, respectively.

## 6.10 Reviewing the temperature (in-)dependence of $E_c(t_w)$

FIG. 6.20 depicts the change in coercive fields at different temperatures. FIG. 6.20 a) shows experimental values and FIG. 6.20 b) shows values calculated with a Weiss Model approach (see section 5.12). Note, according to equation (5.17) and the discussion in section 5.12, the following proportionalities apply at constant temperature: $W_{imprint} \sim E_{imprint} \sim P_{rel} \sim \log(t_w/t_0)$. From FIG. 6.20 a) it could be falsely concluded, that imprinting is independent of temperature. In fact, in section 6.8 it was experimentally shown that and $j_{rel}$ depends on the temperature. Furthermore, in section 3.4 it was shown that $j_{rel}(t_w)|_T \sim T$, for relaxation times that follow a temperature dependence described by Arrhenius law. Similarly, relaxation times that follow the VFT- and compensation law result in $j_{rel}(t_w)|_T \sim (T - T_{VTF})$ and $j_{rel}(t_w)|_T \sim \left(\frac{T'_C T}{T'_C - T}\right)$, respectively. This dilemma can be resolved by reconsidering that the measurement of the experimental $E_c$ impacts on the imprint state. The external field applied while $E_c$ determination induces dipole reorientation (see de-aging, in section 5.2). Thus, it seems that imprinting and de-aging exhibit a similar temperature dependence. At cool temperatures like T$\leq$ 0 °C and −20 °C the slope $d(E_c(t_w) - E_c(20s)/dt_w$ decreases with decreasing temperature. This indicates a change in physics of imprinting, which is probably related to the glass-transitions (see section 2.3.11). The increase of $A$-values in FIG. 6.16 towards cooler temperatures, indicates also that something new is about to happen across the glass-transitions. In a future investigation, next to $j_{rel}$, $\varepsilon(t_w)$ could be measured at different temperatures to study the temperature dependent imprint rate. Both measurements, that of $\varepsilon(t_w)$ and that of $j_{depol}(t_w)$, do not de-age the sample while measuring.

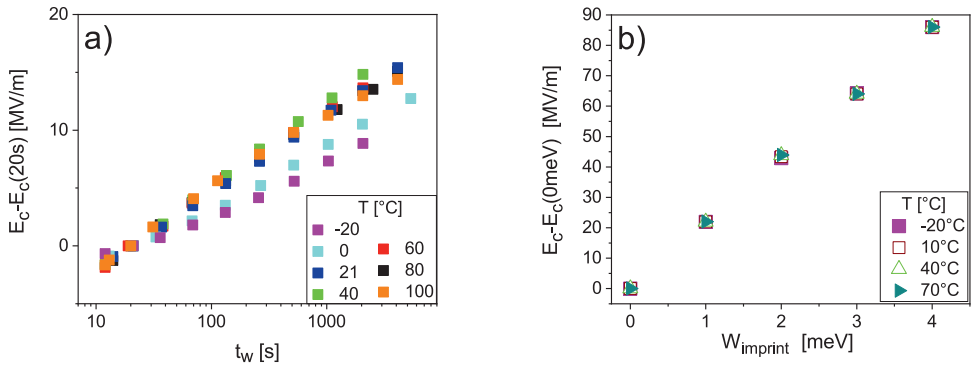


FIGURE 6.20: Comparison of experimental and computed normalized $E_c$. a) Experiment, the values of $E_c(t_w)$ are taken from FIG. 5.9. b) Computed by the Weiss model.

## 6.11 Reviewing the location of imprint related polarization processes

The following discussions in this chapter are of speculative nature and shell be seen mainly as a stimulus for future investigations. The results of the calculation described in section 6.9 indicate that the relaxation times $\tau_i$ of imprinting related polarization processes follow in the high temperature regime (30 °C to 71 °C, or even 30 °C to 90 °C) the compensation law and in the low temperature regime (−10 °C to 50 °C) the VFT-law (or the Arrhenius law).
The compensation law in detail: The compensation law exhibits an upper temperature limit, the Compensation Temperature, ($T'_C$) for its validity. This upper temperature limit coincides approximately with the phase transition temperature, which is here the Curie Temperature (see section 6.9.3 and [89, 112]). The compensation law is also applicable in the vicinity of other thermodynamical transitions, like the glass transition, where the critical compensation temperature is close to the glass transition temperature [111]. Attempts have been made to theoretically justify the compensation law [39, 55, 78, 89, 90, 97]: The deviation of the compensation law is either based on some kind of internal rearrangements in the system renewing the environment, the change in entropy that is neglected in the Arrhenius law and/or the existence of a multi-step relaxation or reaction process. The compensation temperature can be assigned to the point where a cooperative transition, takes place. On the other hand some authors pointed out that compensation of relaxation data has almost no physical meaning [78].
Lets just speculate: Based on the observations that,

- the validity of compensation law [109] and the increased linear thermal expansion (increase of the interplanar distance) of the DFE phase (see section 2.3.8.2) are restricted to about the same temperature regime of approximately 50 °C to 100 °C
- both, the compensation law and the DFE phase exhibit as critical temperature the Curie Temperature

it can be speculated that the relaxation processes which follow the temperature dependence described by the compensation law are also located in the DFE phase.

Location of the imprint mechanism: At cool temperatures ($T \leq 30$ °C) imprinting is connected to dipole relaxation processes in the amorphous phase. The temperature dependence of these processes follow the VTF law (or the Arrhenius-law). At high temperatures ($T \geq 50$ °C) imprinting is connected to dipole relaxation processes in the amorphous phase and the DFE phase, that follow the temperature dependence described by the compensation law. In the temperature range 30 °C to 50 °C both laws can be applied (see section 6.9.5) indicating a transition from pure amorphous rd relaxations to rd relaxations that take place in both amorphous phase and the DFE phase.

In future investigations further evidence regarding the location of the imprint mechanism could be collected by conducting the experiment from section 6.8 at various temperatures in the range 20 °C to 80 °C. Indeed, further studies on the irreversible current density ($j_{irrev}$ [46]) over a broader temperature range would be

[46] $j_{irrev}$ is discussed in the sections 6.6 - 6.8.

interesting, in order to study pyroelectric ageing and the impact of the glass transitions that take place at low temperatures (see section 2.3.11). It was shown in thermal stimulated discharge measurements that increased depolarization currents are recorded across the glass transitions [112]. Furthermore, it would be interesting to conduct imprint measurements in dependence of variously consecutively annealed samples [3, 49, 54]. By consecutive annealing the DFE phase is altered [3] as discussed in more detail in section 6.11.2.

### 6.11.1 Further Discussions: The $\alpha_c$- relaxation

In section 2.3.11.2 a literature review on the $\alpha_c$ relaxation is given, including its characteristic features. The $\alpha_c$ relaxation manifests in P(VDF-TrFE) in pyroelectric measurements as irreversible current contribution, which depends on the storage time [40, 82]. In two subsequently conducted pyroelectric measurements, a certain part doesn't contribute in the second run [112]. Since in such studies commonly non-deaged samples are used, these pattern seem random. In this work however, the short circuit current density while heating was found to be composed only of $j_{pyro}$ and $j_{rel}$ at least in the temperature range 30 °C to 71 °C. Whereas the imprinting current density $j_{rel}$, depends on the time ($t_w$) elapsed since poling, starting from a de-aged sample. There are some striking parallels in the behavior of the $\alpha_c$ relaxation and the imprinting current density $j_{rel}$. Both, $\alpha_c$ relaxation and $j_{rel}$ appear in pyroelectric measurements and for both a logarithmic dependence on the storage time (waiting time $t_w$) is observed.

The $\alpha_c$ relaxation appears also in other polycrystalline but non-ferroelectric materials, whereas imprinting is restricted to the existence of a ferroelectric phase. The logarithmic time dependence of the $\alpha_c$ relaxation might be a consequence of the broad distribution of relaxation times and its manifestation at different temperatures an expression of a meta-stable (DFE-like) phase nature.

### 6.11.2 Further Discussions: The effect of consecutive annealing

The co-polymer exhibits two ferroelectric phases, the defect ferroelectric phase (DFE) and the ferroelectric (FE) phase which transform at the Curie transition both to the paraelectric (PE) phase (see section 2.3.8.2). The Curie Temperature can be altered by a process denoted as consecutive annealing [3, 49, 54]. Consecutive annealing consists in waiting at temperatures close to the Curie transition, before starting a heating run from room temperature. After consecutive annealing two peaks appear in the Curie endotherm [3, 49, 54], whereas the peak at lower temperature can be assigned to the DFE to PE phase transition and the peak at the higher temperature to the FE to PE phase transition [3]. In both transitions a structural transformation from an orthorhombic to hexagonal crystal symmetry takes place [3]. The reason for the lower transition temperature of DFE to PE phase is the existence of a reasonable amount of defects in the crystal structure of the DFE phase [3], whereas the FE phase becomes more stable. That is confirmed by Kim et al. [49] who observed that the ferroelectric phase having the higher Curie transition point exhibits more trans sequences and less gauche defects, closer packing order, shorter intermolecular spacing, larger thickness of the crystallites along the chain axis and an increased transition enthalpy.
The New Imprint Model can provide an explanation for the increase of the FE to PE phase transition temperature which occurs after consecutive annealing. In this

context its worth mentioning that imprinting can explain a paraelectric to ferroelectric phase transition temperature shift as presented in section 6.3. The imprinting process speeds up with increasing temperature (see section 6.8) resulting in a high imprint field by waiting at elevated temperatures. A high imprint field not only stabilizes the ferroelectric polarization but can also induce healing of defects, since $E_{imprint}$ and $P_{fe-cryst}$ point into the same direction. Lets assume that some dipoles which generate $E_{imprint}$ are located in the DFE phase, as discussed in section 6.11. These dipoles reorient in the course of imprinting in anti-parallel fashion to the ferroelectric dipoles, acting effectively as defects [47]. These defects reduce the temperature stability of the phase. Consequently, while the FE phase becomes more temperature stable the DFE becomes less temperature stable by consecutive annealing, which effectively results in the (temperature) separation of the FE to PE and DFE to PE phase transition.

[47] The orientation of aligned rd is discussed in section 5.9

# Chapter 7

# In situ infrared spectroscopy

In the course of this work an IR-transparent aluminum top electrode (see section 4.1.4.1) is designed which allows in-situ IR characterization while simultaneously executing electrical measurements. This work was carried out in cooperation with the institute of "Adhäsion und Interphasen in Polymeren" headed by Prof. Wulff Possart from the University of Saarland. Christophe Nies was involved in all stages of this work, including planning and design, sample preparation, conduction of experiments, interpretation of results and preparing a publishable manuscript.

## 7.1 Introduction

Ultra-thin metal electrodes can provide an infrared (IR) transparent window to the ferroelectric while simultaneously an electric field can be applied and polarization measurements can be conducted. IR spectroscopy is sensitive to structural changes in P(VDF-TrFE). Structural changes can be reorientation processes of molecular dipole moments by application of an electric field [36, 42, 81, 94], phase transformations from a crystalline phase to another [44, 108] or a change in crystallinity [48, 91, 94]. Such investigations have been conducted in transmission mode using ultra-thin metal films as IR transparent frontside and backside electrodes and polymer film thicknesses in the micrometer range. In contrast, reflection absorption fourier transform infrared spectroscopy (RA-FTIR) with a high incidence angle features for thin ($< 1\,\mu m$) co-polymer films an increased signal-to-noise ratio [44, 58]. To investigate poled films or the effect of field application, RA-FTIR is used in combination with corona poling [44]. However, corona poling doesn't allow exact control of the applied field [8] neither its possible to measure simultaneously currents nor polarizations originating from the sample using such a measurement setup. In non-volatile memory devices ultra-thin polymer films are packed in (MFM) capacitor structures. Such samples are seriously effected by thin film effects [33], which slow down the ferroelectric polarization switching process. This slowing down deteriorates the writing performance of such devices. A structural investigation of such samples is pending. Additionally, imprinting is related to polarization processes ought to be visible in dynamic IR spectroscopic measurements.

## 7.2 Infrared measurement setup

IR-detection: In FIG. 7.1 a) the sample is fixed on a sample holder and electrically connected. FIG. 7.1 b) shows the sample and sample holder in the open IR spectrometer (Bruker IFS 66v/S IR spectrometer). During the IR measurement the sample chamber of the IR-spectrometer is purged with dry air (dew point = $-55\,^{\circ}C$),

absolute water concentration 13 µg ($H_2O$) \g(air)), one the on hand to decrease the spectroscopic absorption of water and on the other hand to preserve the samples integrity (see section 4.1.4.1). In this work reflection absorption fourier transform infrared spectroscopy (RA-FTIR) with incident angle of 80° and p-polarized IR irradiation is used. The IR beam illuminates an area of around 1.5 $cm^2$ (ellipse: $d_1$ = 1 cm, $d_2$ =2 cm). 500 IR scans are accumulated to one a IR spectrum, which takes 111.5 s . The IR spectra are recorded with a resolution of 4 $cm^{-1}$. Electrical and IR spectroscopic measurements are carried out in situ, in the sample chamber of the IR-spectrometer at 23 °C.

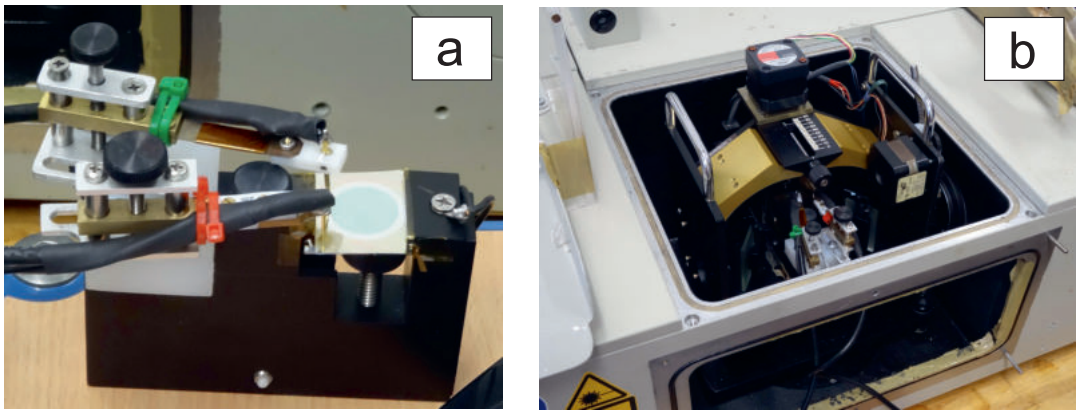


FIGURE 7.1: IR-measurement setup: a) Sample holder and electrically connected sample. b) Sample holder and electrically connected sample in the opened IR-spectrometer.

Electrical measurements during IR spectroscopy: The polarization measurements are carried out by a home made Sawyer Tower system (see section 4.2.3). The voltage drop across the reference capacitor of 10 µF is below $< 5\%$ of the total voltage applied. Thus, the voltage applied to the co-polymer film is $\geq 95\%$ of the stated total voltage.

## 7.3 Results and Discussion

FIG. 7.2 depicts a poling process detected electrically via the sawyer tower method in a) and via IR spectroscopy in b). The IR spectra are recorded at zero applied field. Poling affects specific bands in the IR spectrum. These bands are stated in FIG. 7.2 b). IR-spectra recorded in the poled states ($\pm P_{rem}$) and while application of an electric field ($\pm$ 78 MV $m^{-1}$) are depicted in FIG. 7.3 a). FIG. 7.3 b) and c) shows IR-spectra in the range of wavenumbers at which the IR spectra change the most. The IR-spectra differ if an electric field is applied compared to if no field is applied, but they are alike regarding the $+P_{rem}$ and $-P_{rem}$ states and regarding applying positive 78 MV $m^{-1}$ and negative 78 MV $m^{-1}$.

With this setup it might by possible in future investigations

- to investigate the role of interphases at the top and bottom electrode. Therefore, it seems feasible to simultaneously determine the change in the ferroelectric polarization switching properties with decreasing co-polymer film thickness electrically and structurally.

- to observe the structural changes taking place in the course of the imprinting process at constant temperature, with simultaneous monitoring of (electrical) imprinting effects. The effect of imprinting on $j_{rel}(t_w)$ and $\varepsilon(t_w)$ (see section 5.1) can be measured without disturbing the imprinting process.

- to observe the structural changes taking place in the imprinting process as a function of the temperature with simultaneous determination of the imprinting current $j_{rel}$ while heating. Here it might be of special interest to compare IR spectra before with those after a heating process. As shown in section 6.8 heating speeds up the imprinting process rigorously.

- heating the poled sample above the Curie Temperature, while measuring the short circuit current. This might elucidate the reason why the short circuit current while heating (see section 6.5) is so different if starting the heating process in $-P_{rem}$ compared to a start in $+P_{rem}$.

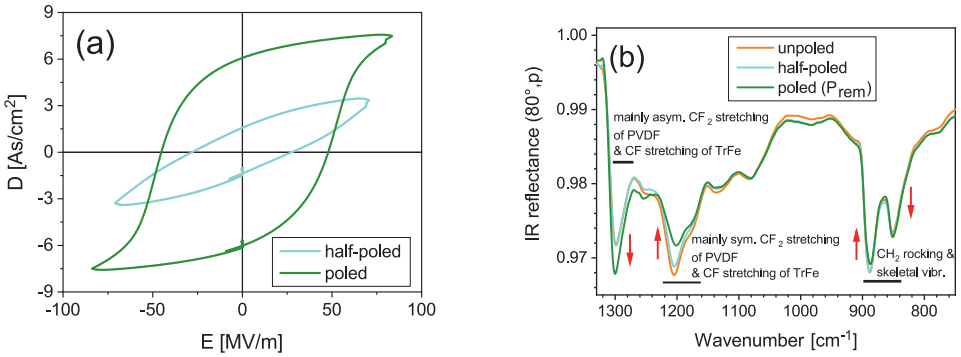


FIGURE 7.2: Poling process of an "as cast" sample. a) Ferroelectric polarization hysteresis. b) IR-spectra at zero applied field, at different stages of poling.

Furthermore, this methode is not restricted to Al electrodes, since also other materials such as ultra-thin Au, Cr, Ni and Cu films, as well as $In_2O_3$ (for near IR) and CNT are IR transparent and simultaneously electrically conducting [28, 29, 37, 68, 116, 119]. Thus, the role of the interface and interphase adjacent to the electrodes can also be investigated by using different electrode materials.

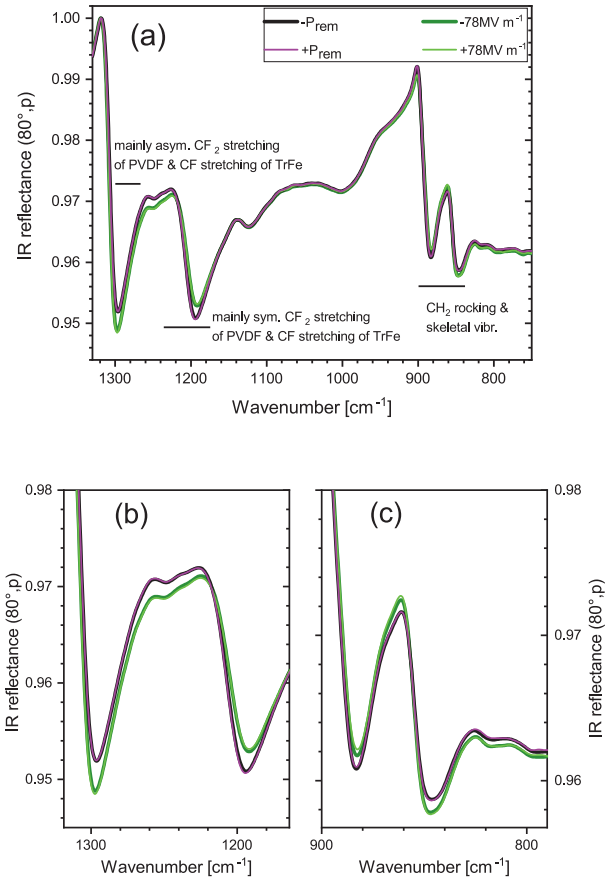


FIGURE 7.3: IR spectra of poled samples at zero applied field and during field application.

# Chapter 8

# Summary and Outlook

This work presents an integral investigation of the imprint process in P(VDF-TrFE). First, two procedures to delete imprint are investigated, denoted as "de-aging by switching" and "de-aging above $T_C$", which consist in repeated ferroelectric polarization switching and heating the sample above the Curie Temperature ($T_C$), respectively. It is found that de-aging by switching is faster but less effective than de-aging above $T_C$. Imprinting is always investigated after imprint has initially been deleted by either one of the two just mentioned de-aging procedures. Following changes in the material properties were found to be caused by imprinting, which are therefore called imprint effects: increase of the ferroelectric polarization switching time $\tau(t_w)$, increase of coercive field $E_c(t_w)$, decay of the remanent polarization $P_{rem}(t_w)$ and decay of the permittivity $\varepsilon(t_w)$. All imprint effects are in one way or another dependent on $\log(t_w)$, whereas the waiting time $t_w$ denotes the duration waiting in a poled state (e.g. a remanent polarization state).
Imprint models presented in literature are discussed in the light of (new) experimental findings. Based on success and fail predictions of these models, a new imprint model is designed, which can explain the following experimental findings: an increased co-polymer crystallinity reduces the building up of imprint, the imprint process is independent of the co-polymer film thickness, all imprint effects exhibit in one way or another a $\log(t_w)$ dependence and imprint evolves (with unvarying $\log(t_w)$ dependence of the imprint effects) over huge time span of at least 10 decades in time ($10^{-4}\,\mathrm{s} \leq t_w \leq 10^{6}\,\mathrm{s}$). The new imprint model is in its nature a feedback model, where the ferroelectric polarization present in the crystallites $P_{fe-cryst}$ and the polarization in the amorphous phase $P_{rel}$ act on each other via stray fields.
The new imprint model is now briefly outlined. The co-polymer material is assumed to exhibit (edge-on) ferroelectric crystallites which are embedded in a non-ferroelectric amorphous matrix. In this model, the polymer can be imagined as a "Raisin Bread": the crystallites are scattered in the amorphous phase, like the raisins in the bread. $P_{fe-cryst}$ generates a stray field which acts on the dipoles in the amorphous phase. The dipoles in the amorphous phase reorient in this stray field and thereby $P_{rel}$ is built-up. $P_{rel}$ increases as a function of $\log(t_w)$, due to a distribution of energy barriers for dipole reorientation. Now a feedback comes into play: The aligned dipoles in the amorphous phase generate themselves stray fields, which sum up to the imprint field $E_{imprint}(t_w)$ in the crystallites, thus at the location of $P_{fe-cryst}$. The vectors $\mathbf{E}_{imprint}$ and $\mathbf{P}_{fe-cryst}$ point into the same direction. Thus, $E_{imprint}$ stabilizes the ferroelectric polarization state and e.g. a ferroelectric polarization switching process is aggravated.
The impact of imprinting is calculated introducing $E_{imprint}(t_w)$ as local field contribution in a mean field model based on a Weiss field approach. Calculated and experimental imprint effects follow the same functional time ($t_w$) dependence, however the calculated absolute values of $\tau$, $E_c$, $P_{rem}$ and $\varepsilon$ don't match their experimental

counterparts. Nonetheless, quantitative reflections based on relative changes underline the validity of the calculation and likewise the quality of the new imprint model.

With the eventual aim to investigate the temperature dependence of imprinting, short circuit currents while heating and cooling with constant rate in the temperature range $-20\,^{\circ}\mathrm{C}$ to $140\,^{\circ}\mathrm{C}$ are recorded. Integration of these currents respective to time yield polarization versus temperature hysteresis loops, which are presented using un-poled (spontaneous polarization hysteresis) and poled samples. It is shown that the spontaneous ferroelectric polarization is much smaller than the field induced remanent polarization. A change in the Curie transition temperature is observed when varying the cooling rate or the strength of an externally applied field. These shifts in the Curie transition temperature are discussed qualitatively in the view of the New Imprint Model. Samples poled to positive and negative remanent polarization state ($\pm P_{rem}$) were found to exhibit short circuit currents which fundamentally differ from each other in the temperature range of the ferroelectric to paraelectric phase transition. It is speculated that an oxidized electrode layer at the samples bottom side, interphases between electrode and polymer at top and bottom side, the release of compensation charges and the decay of the polarization in the amorphous phase play a role in causing this asymmetry.
At temperatures below the ferroelectric to paraelectric phase transition temperature range the short circuit current density is found to be composed of the pyroelectric current density ($j_{pyro}$) and the imprinting current density ($j_{rel}$). The temperature dependent pyroelectric coefficient, which is calculated from $j_{pyro}$, is found to be stable under thermal cycling below $71\,^{\circ}\mathrm{C}$. Exceeding this temperature results in a decay of the pyroelectric coefficient, which is known in literature as pyroelectric aging. We gathered evidence that pyroelectric aging is connected to the decay of the ferroelectric polarization when entering the ferroelectric to paraelectric phase transition temperature range. Pyroelectric aging is on the other hand found to be independent on imprint, which is surprising, since $P_{rel}$ opposes $P_{fe}$.
The imprinting current while heating $j_{rel}$ is calculated. This is done via summation of Debye-like polarization processes which exhibit a broad distribution of relaxation times. The distribution of relaxation times is based on an uniform energy barrier distribution, which is reasoned by the experimentally observed $\log(t_w)$ dependence of imprint effects. Good fits to the experimental curves are found if the temperature dependence of relaxation times is governed by the Vogel-Tammann-Fulcher (or Arrhenius -) law at low temperatures ($-10\,^{\circ}\mathrm{C}$ to $50\,^{\circ}\mathrm{C}$) and a compensation law at high temperatures ($30\,^{\circ}\mathrm{C}$ to $71\,^{\circ}\mathrm{C}$). Based on these temperature dependencies and structural investigations done by other research groups it is speculated, that at high temperatures also dipoles in the so called defect ferroelectric (DFE) phase, next to those in the amorphous phase, reorient in the course of the imprinting process. The DFE phase is assumed to be an interphase at the boundary crystalline-amorphous. At the end of the work about imprinting, the $\alpha_c$ relaxation process and the effect of consecutive annealing are discussed in the light of new experimental findings.
In the last chapter a new experimental method is presented, which uses an ultrathin metal top electrode that provides an infrared (IR) transparent window to the ferroelectric co-polymer while simultaneously an electric field can be applied and polarization measurements can be conducted.

A future investigation could study the short circuit current density while heating and cooling for differently consecutively annealed samples. This might provide further insights into imprinting at high temperatures and the meta-stable states of/in

the crystalline-amorphous interphase. The crystalline-amorphous interphase is nowadays intensively discussed in the scientific community. The in-situ IR spectroscopic measurement method presented, might be a suitable tool to resolve simultaneous to the electrical investigation the structural changes taking place in these interphases. Imprinting across the glass transition ranges would also be an interesting spot to look at.

# Appendix A

# Publications

## A.1 Articles

- "Imprint in Poly(vinylidenfluoride-trifluoroethylene)", C. Peter and H. Kliem, IEEE International Conference on Dielectrics (ICD), Proc. IEEE, Vol. 2, pp. 1–4, Montpellier (2016)
- "Characteristic time dependence of imprint properties in P(VDF-TrFE)", C. Peter, A. Leschhorn and H. Kliem, J. Appl. Phys. 120, 124105 (2016)
- "Epitaxy of ferroelectric P(VDF-TrFE) films via removable PTFE templates and its application in semiconducting/ferroelectric blend resistivity memory", Wei Xia, Christian Peter, Junhui Weng, Jian Zhang, Herbert Kliem, Yulong Jiang and Guodong Zhu, ACS Applied Materials and Interfaces 9, 12130 (2017)
- "Feedback of the amorphous phase on the ferroelectric phase: Imprint effects in P(VDF-TrFE)", C. Peter and H. Kliem, IEEE 2nd International Conference on Dielectrics (ICD), pp. 1-4, Budapest, Hungary (2018)
- "Ferroelectric imprint and polarization in the amorphous phase in P(VDF-TrFE)", C. Peter and H. Kliem, J. Appl. Phys. 125, 174107 (2019)

## A.2 Conference contributions

- Poster contribution: "Dependence of the switching speed on the prepolarization in PVDF copolymers", C. Peter and H. Kliem, European Meeting on Ferroelectricity 13, P7_1 Porto, Portugal (2015)
- Poster contribution: "Imprint in Poly(vinylidenfluoride-trifluoroethylene)", C. Peter and H. Kliem, International Conferences on Dielectrics (ICD), P701, Montpellier, France (2016)
- "Dielectric relaxation and ferroelectric switching in PVDF copolymers" eingeladener Vortrag beim 3. Chinesisch-Deutschen Symposium über Ladungen und Electrete, C. Peter O. Elshehy, M. Mai, B. Martin, A. Leschhorn and H. Kliem, Shanghai, China (2018)
- Talk: "Feedback of the amorphous phase on the ferroelectric phase: imprint effects in PVDF-TrFE", C. Peter and H. Kliem, International Conferences on Dielectrics (ICD), oral session 5, 119, Budapest, Hungary (2018)
- "Ferroelectric imprint and dielectric relaxation in P(VDF-TrFE)", C. Peter and H. Kliem, IEEE EMF, page 315, Lausanne, Switzerland (2019)

- "A novel model for ferroelectric imprint in P(VDF-TrFE)" H. Kliem and C. Peter, Plenarvortrag bei: 2nd Int. Conf. on Nanomat. Sci. and Mech. Engineering, Book of Abstracts, S. 40, Aveiro, Portugal (2019)
- "Dielectric relaxation, ferroelectric switching and imprint in PVDF copolymers" C. Peter and H. Kliem, ISNPFDADM, Bonifacio, France (2019)
- Talk: "Reversible and irreversible pyroelectricity – thermal expansion and ferroelectric imprinting in P(VDF-TrFE)" C. Peter, H. Kliem, MRS Fall Meeting, EL02.01.02, Boston, USA (2019)

# Bibliography


[1] H. N. Al-Shareef et al. "Voltage offsets and imprint mechanism in SrBi2Ta2O9 thin films". In: *Journal of Applied Physics* 80.8 (1996), pp. 4573–4577. URL: https://doi.org/10.1063/1.363440.

[2] G. Arlt and H. Neumann. "Internal bias in ferroelectric ceramics: Origin and time dependence". In: *Ferroelectrics* 87.1 (1988), pp. 109–120. URL: http://dx.doi.org/10.1080/00150198808201374.

[3] François Bargain et al. "From solvent-cast to annealed and poled poly(VDF-co-TrFE) films: New insights on the defective ferroelectric phase". In: *Polymer* 105 (2016). Structure and Dynamics of Polymers studied by X-ray, Neutron and Muon Scattering, pp. 144 –156. ISSN: 0032-3861. URL: http://www.sciencedirect.com/science/article/pii/S0032386116309132.

[4] E Bellet-Amalric and J. Legrand. "Crystalline structures and phase transition of the ferroelectric P(VDF-TrFE) copolymers, a neutron diffraction study". In: *European Journal of Physics B* 3 (1998), p. 225.

[5] Jaroslavas Belovickis et al. "Dielectric, Ferroelectric, and Piezoelectric Investigation of Polymer-Based P(VDF-TrFE) Composites". In: *physica status solidi (b)* 255.3 (2018), p. 1700196. URL: https://onlinelibrary.wiley.com/doi/abs/10.1002/pssb.201700196.

[6] J. G. Bergman, J. H. McFee, and G. R. Crane. "Pyroelectricity and Optical Second Harmonic Generation in Polyvinylidene Fluoride Films". In: *Applied Physics Letters* 18.5 (1971), pp. 203–205. URL: https://doi.org/10.1063/1.1653624.

[7] Martin Bohlén and Kim Bolton. "Conformational studies of poly(vinylidene fluoride), poly(trifluoroethylene) and poly(vinylidene fluoride-co-trifluoroethylene) using density functional theory". In: *Phys. Chem. Chem. Phys.* 16 (2014), pp. 12929–12939. URL: http://dx.doi.org/10.1039/C4CP01012D.

[8] C. Bosshard et al. *Advances in Polymer Science 158, Polymer for Photonics Applications I*. p.43. Berlin: Springer, 2002.

[9] Jakob J. Brondijk et al. "Physics of organic ferroelectric field-effect transistors". In: *Journal of Polymer Science Part B: Polymer Physics* 50.1 (2012), pp. 47–54. URL: https://onlinelibrary.wiley.com/doi/abs/10.1002/polb.22363.

[10] A. V. Bune et al. "Piezoelectric and pyroelectric properties of ferroelectric Langmuir–Blodgett polymer films". In: *Journal of Applied Physics* 85.11 (1999), pp. 7869–7873. URL: https://doi.org/10.1063/1.370598.

[11] A. J. Bur, J. D. Barnes, and K. J. Wahlstrand. "A study of thermal depolarization of polyvinylidene fluoride using x-ray pole-figure observations". In: *Journal of Applied Physics* 59.7 (1986), pp. 2345–2354. URL: https://doi.org/10.1063/1.336332.

[12] J. C. Burfoot and G. W. Taylor. *Polar Dielectrics*. London: MacMillan Press, 1979.

[13] K. Carl and K. H. Hardtl. "Electrical after-effects in Pb(Ti, Zr)O3 ceramics". In: *Ferroelectrics* 17.1 (1977), pp. 473–486. URL: http://dx.doi.org/10.1080/00150197808236770.

[14] Yingxin Chen et al. "Low-temperature crystallization of P(VDF-TrFE-CFE) studied by Flash DSC". In: *Polymer* 84 (2016), pp. 319 –327. ISSN: 0032-3861. URL: http://www.sciencedirect.com/science/article/pii/S0032386116300039.

[15] G. Eberle, E. Bihler, and W. Eisenmenger. "Polarization Dynamics of P(VDF-TrFE) Copolymers". In: *IEEE Transactions on Electrical Insulation* 26.1 (1991), pp. 69–77. URL: https://elib.uni-stuttgart.de/bitstream/11682/4976/1/eis106.pdf.

[16] *Effective Field Approach to Phase Transitions an Some Applications to Ferroelectrics*. World Scientific Publishing Co.Pte. Ldt., 2006.

[17] W. Eisenmenger, H. Schmidt, and B. Dehlen. "Space charge and dipoles in polyvinylidenefluoride". In: *Brazilian Journal of Physics* 29 (June 1999), pp. 295 –305. ISSN: 0103-9733. URL: http://www.scielo.br/scielo.php?script=sci_arttext&pid=S0103-97331999000200011&nrm=iso.

[18] Leeya Engel et al. "A study toward the development of an electromechanical poly(vinylidene fluoride–trifluoroethylene–chlorofluoroethylene) buckling membrane actuator". In: *Journal of Micromechanics and Microengineering* 24.12 (2014), p. 125027. URL: https://doi.org/10.1088%2F0960-1317%2F24%2F12%2F125027.

[19] Huajing Fang et al. "Facile fabrication of highly ordered poly(vinylidene fluoride-trifluoroethylene) nanodot arrays for organic ferroelectric memory". In: *Journal of Applied Physics* 119.1 (2016), p. 014104. URL: https://doi.org/10.1063/1.4939601.

[20] S. N. Fedosov and H. von Seggern. "Pyroelectricity in polyvinylidene fluoride: Influence of polarization and charge". In: *Journal of Applied Physics* 103.1 (2008), p. 014105. URL: https://doi.org/10.1063/1.2824940.

[21] Sergei N. Fedosov and Heinz von Seggern. "Back-switching of ferroelectric polarization in two-component systems". In: *Journal of Applied Physics* 96.4 (2004), pp. 2173–2180. URL: https://doi.org/10.1063/1.1765867.

[22] *Ferroelectricity*. Wiley-VCH Verlag GmbH & Co. KGaA, Weinheim, 2005.

[23] T. Furukawa, M. Date, and G. E. Johnson. "Polarization reversal associated with rotation of chain molecules in $\beta$-phase polyvinylidene fluoride". In: *Journal of Applied Physics* 54.3 (1983), pp. 1540–1546. URL: https://doi.org/10.1063/1.332182.

[24] T. Furukawa, T. Nakajima, and Y. Takahashi. "Factors governing ferroelectric switching characteristics of thin VDF/TrFE copolymer films". In: *IEEE Transactions on Dielectrics and Electrical Insulation* 13.5 (2006), pp. 1120–1131. ISSN: 1070-9878. DOI: 10.1109/TDEI.2006.247840.

[25] Takeo Furukawa. "Ferroelectric properties of vinylidene fluoride copolymers". In: *Phase Transitions* 18.3-4 (1989), pp. 143–211. URL: https://doi.org/10.1080/01411598908206863.

[26] Takeo Furukawa. "Structure and functional properties of ferroelectric polymers". In: *Advances in Colloid and Interface Science* 71-72 (1997). The PRESTO Program: Structure and Functional Properties, pp. 183 –208. ISSN: 0001-8686. URL: http://www.sciencedirect.com/science/article/pii/S0001868697900178.

[27] A. Gerber et al. "Ferroelectric field effect transistors using very thin ferroelectric polyvinylidene fluoride copolymer films as gate dielectrics". In: *Journal of Applied Physics* 107.12 (2010), p. 124119. URL: https://doi.org/10.1063/1.3437638.

[28] D. S. Ghosh et al. "Widely transparent electrodes based on ultrathin metals". In: *Opt. Lett.* 34.3 (2009), pp. 325–327. URL: https://pubmed.ncbi.nlm.nih.gov/19183646/.

[29] Stefano Giurgola et al. "Ultra thin nickel transparent electrodes". In: *Journal of Materials Science: Materials in Electronics* 20.1 (2009), pp. 181–184. ISSN: 1573-482X. URL: http://dx.doi.org/10.1007/s10854-007-9519-7.

[30] M. Grossmann et al. "The interface screening model as origin of imprint in PbZrxTi1-xO3 thin films. I. Dopant, illumination, and bias dependence". In: *Journal of Applied Physics* 92.5 (2002), pp. 2680–2687. URL: http://scitation.aip.org/content/aip/journal/jap/92/5/10.1063/1.1498966.

[31] M. Grossmann et al. "The interface screening model as origin of imprint in PbZrxTi1-xO3 thin films. II. Numerical simulation and verification". In: *Journal of Applied Physics* 5 (2002), pp. 2688–2696. URL: http://scitation.aip.org/content/aip/journal/jap/92/5/10.1063/1.1498967.

[32] Dong Guo and Nava Setter. "Impact of Confinement-Induced Cooperative Molecular Orientation Change on the Ferroelectric Size Effect in Ultrathin P(VDF-TrFE) Films". In: *Macromolecules* 46.5 (2013), pp. 1883–1889. URL: http://dx.doi.org/10.1021/ma302377q.

[33] Roman Gysel et al. "Restricted domain growth and polarization reversal kinetics in ferroelectric polymer thin films". In: *Journal of Applied Physics* 103.8, 084120 (2008). URL: http://scitation.aip.org/content/aip/journal/jap/103/8/10.1063/1.2907990.

[34] W. Hau et al. "Wettability of organic ferroelectric material on metal substrate". In: *2012 13th International Thermal, Mechanical and Multi-Physics Simulation and Experiments in Microelectronics and Microsystems*. USA: IEEE, 2012, pp. 1/5–5/5. DOI: 10.1109/ESimE.2012.6191738.

[35] P. Hidnert. "Thermal Expansion of Five Selected Optical Glasses". In: *Journal of Research of the National Bureau of Standards* 52.6 (1954), pp. 311–312. URL: https://nvlpubs.nist.gov/nistpubs/jres/52/jresv52n6p311_A1b.pdf.

[36] S. L. Hsu et al. "Analysis of the crystalline phase transformation of poly(vinylidene fluoride)". In: *Macromolecules* 18.12 (1985), pp. 2583–2587. URL: http://dx.doi.org/10.1021/ma00154a038.

[37] Liangbing Hu, David S. Hecht, and George Grüner. "Infrared transparent carbon nanotube thin films". In: *Applied Physics Letters* 94.8 (2009), p. 081103. URL: http://dx.doi.org/10.1063/1.3075067.

[38] J. G. Huang et al. "Torsional frequency mixing and sensing in optomechanical resonators". In: *Applied Physics Letters* 111.11 (2017), p. 111102. URL: https://doi.org/10.1063/1.4986811.

[39] J. P. Ibar. "Application of compensation phenomena to the thermal analysis characterization of polymers: Introducing the degree of disorder (DOD) number:" in: *Polymer Engineering & Science* 31.20 (1991), pp. 1467–1475. URL: https://onlinelibrary.wiley.com/doi/abs/10.1002/pen.760312005.

[40] Laurent Ibos et al. "Thermal aging of pyroelectricity in PVDF and P(VDF-TrFE) copolymers". In: *Polymers and Liquid Crystals*. Ed. by Andrzej Wlochowicz. Vol. 4017. International Society for Optics and Photonics. Cardiff, Wales: SPIE, 1999, pp. 29 –36. URL: https://doi.org/10.1117/12.373716.

[41] Susumu Ikeda, Tomohiro Fukada, and Yasaku Wada. "Effect of space charge on polarization reversal in a copolymer of vinylidene fluoride and trifluoroethylene". In: *Journal of Applied Physics* 64.4 (1988), pp. 2026–2030. URL: https://doi.org/10.1063/1.341733.

[42] Fei Jei Lu, David Allen Waldman, and Shaw Ling Hsu. "A spectroscopic study to interpret the increased piezoelectric effect at high temperature in poly(vinylidene fluoride)". In: *Journal of Polymer Science: Polymer Physics Edition* 22.5 (1984), pp. 827–834. ISSN: 1542-9385. URL: http://dx.doi.org/10.1002/pol.1984.180220504.

[43] Samson A. Jenekhe. "Effects of solvent mass transfer on flow of polymer solutions on a flat rotating disk". In: *Industrial & Engineering Chemistry Fundamentals* 23.4 (1984), pp. 425–432. URL: https://doi.org/10.1021/i100016a008.

[44] Xing Yu Jin, Kap Jin Kim, and Han Sup Lee. "Grazing incidence reflection absorption Fourier transform infrared (GIRA-FTIR) spectroscopic studies on the ferroelectric behavior of poly(vinylidene fluoride–trifluoroethylene) ultrathin films". In: *Polymer* 46.26 (2005), pp. 12410 –12415. ISSN: 0032-3861. URL: http://www.sciencedirect.com/science/article/pii/S003238610501534X.

[45] Heiji Kawai. "The Piezoelectricity of Poly (vinylidene Fluoride)". In: *Japanese Journal of Applied Physics* 8.7 (1969), pp. 975–976. URL: https://doi.org/10.1143%2Fjjap.8.975.

[46] R. G. Kepler and R. A. Anderson. "Ferroelectricity in polyvinylidene fluoride". In: *Journal of Applied Physics* 49.3 (1978), pp. 1232–1235. URL: https://doi.org/10.1063/1.325011.

[47] R.G. Kepler and R.A. Anderson. "Ferroelectric polymers". In: *Advances in Physics* 41.1 (1992), pp. 1–57. URL: https://doi.org/10.1080/00018739200101463.

[48] Kap J. Kim, Nicholas M. Reynolds, and Shaw Ling Hsu. "Spectroscopic analysis of the crystalline and amorphous phases in a vinylidene fluoride/trifluoroethylene copolymer". In: *Macromolecules* 22.12 (1989), pp. 4395–4401. URL: http://dx.doi.org/10.1021/ma00202a001.

[49] Kap Jin Kim and Gwan Bum Kim. "Curie transition, ferroelectric crystal structure and ferroelectricity of a VDF/TrFE (7525) copolymer: 2. The effect of poling on Curie transition and ferroelectric crystal structure". In: *Polymer* 38.19 (1997), pp. 4881 –4889. ISSN: 0032-3861. URL: http://www.sciencedirect.com/science/article/pii/S0032386196000183.

[50] Kuniko Kimura et al. "Investigation of Molecular Chain Orientation Change of Polymer Crystals in Phase Transitions by Friction Anisotropy Measurement". In: *Langmuir* 23.9 (2007). PMID: 17388614, pp. 4740–4745. URL: https://doi.org/10.1021/la063270p.

[51] Kuniko Kimura et al. “Orientation control of ferroelectric polymer molecules using contact-mode AFM”. In: *European Polymer Journal* 40.5 (2004). Selected papers from the 3rd International Conference on Scanning Probe Microscopy of Polymers, pp. 933 –938. ISSN: 0014-3057. URL: http://www.sciencedirect.com/science/article/pii/S0014305704000291.

[52] Herbert Kliem. “Dielectric Relaxation and Ferroelectric Imprint”. In: *Annual Rep. IEEE CEIDP* (2018), pp. 1–8.

[53] Herbert Kliem and Markus Kühn. “Modeling the switching kinetics in ferroelectrics”. In: *Journal of Applied Physics* 110.11, 114106 (2011), p. 114106. URL: https://doi.org/10.1063/1.3660680.

[54] Keiko Koga and Hiroji Ohigashi. “Piezoelectricity and related properties of vinylidene fluoride and trifluoroethylene copolymers”. In: *Journal of Applied Physics* 59.6 (1986), pp. 2142–2150. URL: https://doi.org/10.1063/1.336351.

[55] Jan Kohout. “Modified Arrhenius Equation in Materials Science, Chemistry and Biology”. In: *Molecules* 26.23 (2021). ISSN: 1420-3049. URL: https://www.mdpi.com/1420-3049/26/23/7162.

[56] A. G. Kolbeck. “Aging of piezoelectricity in poly(vinylidene fluoride)”. In: *Journal of Polymer Science: Polymer Physics Edition* 20.11 (1982), pp. 1987–2001. URL: https://onlinelibrary.wiley.com/doi/abs/10.1002/pol.1982.180201102.

[57] I. Lazareva et al. “Interface screening and imprint in poly(vinylidene fluoride/trifluoroethylene) ferroelectric field effect transistors”. In: *Journal of Applied Physics* 105.5 (2009), p. 054110. URL: https://doi.org/10.1063/1.3088887.

[58] Jong Soon Lee, Arun Anand Prabu, and Kap Jin Kim. “Annealing effect upon chain orientation, crystalline morphology, and polarizability of ultra-thin P(VDF-TrFE) film for nonvolatile polymer memory device”. In: *Polymer* 51.26 (2010), pp. 6319 –6333. ISSN: 0032-3861. URL: http://www.sciencedirect.com/science/article/pii/S0032386110009572.

[59] Andreas Leschhorn, Stephane Djoumbou, and Herbert Kliem. “Microscopic model of domain wall motion”. In: *Journal of Applied Physics* 115.11 (2014), p. 114106. URL: https://doi.org/10.1063/1.4868901.

[60] Connie Lew and Michael O. Thompson. “Characterizing trapped charge dynamics in imprinted poly(vinylidene fluoride-trifluoroethylene) ferroelectric thin films using the fast ramp thermally stimulated current technique”. In: *Journal of Applied Physics* 105.5, 054112 (2009), p. 054112. URL: http://scitation.aip.org/content/aip/journal/jap/105/5/10.1063/1.3081639.

[61] Connie Lew and Michael O. Thompson. “Quantifying electronic charge trap states and the effect of imprint on ferroelectric poly(vinylidene fluoride-trifluoroethylene) thin films”. In: *Journal of Applied Physics* 107.10, 104110 (2010). URL: http://scitation.aip.org/content/aip/journal/jap/107/10/10.1063/1.3427559.

[62] Mengyuan Li et al. “Controlling the microstructure of poly(vinylidene-fluoride) (PVDF) thin films for microelectronics”. In: *J. Mater. Chem. C* 1 (46 2013), pp. 7695–7702. URL: http://dx.doi.org/10.1039/C3TC31774A.

[63] Mengyuan Li et al. "Revisiting the $\delta$-phase of poly(vinylidene fluoride) for solution-processed ferroelectric thin films". In: *Nature Materials* 12 (2013), p. 433. URL: https://www.nature.com/articles/nmat3577#supplementary-information.

[64] P F Liu et al. "Huge electrocaloric effect in Langmuir–Blodgett ferroelectric polymer thin films". In: *New Journal of Physics* 12.2 (2010), p. 023035. URL: https://doi.org/10.1088%2F1367-2630%2F12%2F2%2F023035.

[65] Kyriakos Loufakis and Bernhard Wunderlich. "Thermal analysis of the conformational disorder in semicrystalline poly(vinylidene fluoride) and poly(trifluoroethylene)". In: *Macromolecules* 20.10 (1987), pp. 2474–2478. URL: https://doi.org/10.1021/ma00176a026.

[66] Andrew J. Lovinger. "Ferroelectric Polymers". In: *Science* 220.4602 (1983), pp. 1115–1121. ISSN: 0036-8075. URL: http://science.sciencemag.org/content/220/4602/1115.

[67] S. G. Lu et al. "Electrocaloric Effect in Ferroelectric P(VDF-TrFE) Copolymers". In: *Integrated Ferroelectrics* 125.1 (2011), pp. 176–185. URL: https://doi.org/10.1080/10584587.2011.574491.

[68] Guoping Luo et al. "High-performance inverted polymer solar cells based on thin copper film". In: *Journal of Photonics for Energy* 5.1 (2014), p. 057206. URL: http://dx.doi.org/10.1117/1.JPE.5.057206.

[69] M. Mai. "Polarization Switching in Ferroelectric Films of P(VDF-TrFE) Copolymer". PhD thesis. Institue of Electrical Engineering Physics, Saarland University, 2013.

[70] Manfang Mai, Andreas Leschhorn, and Herbert Kliem. "The field and temperature dependence of hysteresis loops in P(VDF–TrFE) copolymer films". In: *Physica B: Condensed Matter* 456 (2015), pp. 306 –311. ISSN: 0921-4526. URL: http://www.sciencedirect.com/science/article/pii/S0921452614007352.

[71] Manfang Mai, Bjoern Martin, and Herbert Kliem. "Ferroelectric switching in Langmuir-Blodgett and spin-coated thin films of poly(vinylidene fluoride/trifluoroethylene) copolymers". In: *Journal of Applied Physics* 110.6 (2011), p. 064101. URL: http://dx.doi.org/10.1063/1.3636397.

[72] Manfang Mai, Bjoern Martin, and Herbert Kliem. "Polarization relaxation and charge injection in thin films of poly(vinylidene fluoride/trifluoroethylene) copolymer". In: *Journal of Applied Physics* 114.5 (2013), p. 054104. URL: https://doi.org/10.1063/1.4817508.

[73] Manfang Mai et al. "Ferroelectric Polymer Thin Films for Organic Electronics". In: *Journal of Nanomaterials* 2015 (2015), p. 812538. URL: http://dx.doi.org/10.1155/2015/812538.

[74] D. Mao et al. "Optimization of poly(vinylidene fluoride-trifluoroethylene) films as non-volatile memory for flexible electronics". In: *Organic Electronics* 11 (2010), pp. 925–932. DOI: 10.1016/j.orgel.2010.02.012.

[75] Bjoern Martin, Markus Kuehn, and Herbert Kliem. "Interacting and noninteracting dipole systems in ferroelectric poly(vinylidene fluoride-trifluoroethylene) copolymer". In: *Journal of Applied Physics* 108.8, 084109 (2010). URL: http://scitation.aip.org/content/aip/journal/jap/108/8/10.1063/1.3499614.

[76] Walter J. Merz. "Domain Formation and Domain Wall Motions in Ferroelectric $BaTiO_3$ Single Crystals". In: *Phys. Rev.* 95 (3 1954), pp. 690–698. URL: https://link.aps.org/doi/10.1103/PhysRev.95.690.

[77] Mohamad Hafiz Mohd Wahid et al. "Different Surface Morphology of Annealed PVDF-TrFE Thin Films and the Effect on its Ferroelectric Properties". In: *Nanoscience, Nanotechnology and Nanoengineering*. Vol. 832. Advanced Materials Research. Trans Tech Publications, Jan. 2014, pp. 724–727. DOI: 10.4028/www.scientific.net/AMR.832.724.

[78] Joaquim J. Moura Ramos, João F. Mano, and Bryan B. Sauer. "Some comments on the significance of the compensation effect observed in thermally stimulated current experiments". In: *Polymer* 38.5 (1997), pp. 1081–1089. ISSN: 0032-3861. URL: https://www.sciencedirect.com/science/article/pii/S0032386196006349.

[79] Horst E. Müser, Walter J. Kuhn, and Johann Albers. "Thermal hysteresis at the cubic/tetragonal phase transition in melt-grown BaTiO3 single crystals". In: *Ferroelectrics Letters Section* 15.3-4 (1993), pp. 101–107. URL: https://doi.org/10.1080/07315179308204245.

[80] Horst E. Müser and Hans-Günther Unruh. "Das dielektrische Verhalten der Ferroelektrika bei einer Umwandlung zweiter Ordnung". In: *Z. Naturforschg.* 21 a (1966), 783—792.

[81] D. Naegele and D. Y. Yoon. "Orientation of crystalline dipoles in poly(vinylidene fluoride) films under electric field". In: *Applied Physics Letters* 33.2 (1978), pp. 132–134. URL: http://dx.doi.org/10.1063/1.90281.

[82] M Neidhöfer et al. "Structural evolution of PVDF during storage or annealing". In: *Polymer* 45.5 (2004), pp. 1679 –1688. ISSN: 0032-3861. URL: http://www.sciencedirect.com/science/article/pii/S0032386103012278.

[83] Hiroji Ohigashi, Shuyo Akama, and Keiko Koga. "Lamellar and Bulk Single Crystals Grown in Annealed Films of Vinylidene Fluoride and Trifluoroethylene Copolymers". In: *Japanese Journal of Applied Physics* 27.11R (1988), p. 2144. URL: http://stacks.iop.org/1347-4065/27/i=11R/a=2144.

[84] Hiroji Ohigashi, Kenji Omote, and Teruhisa Gomyo. "Formation of "single crystalline films" of ferroelectric copolymers of vinylidene fluoride and trifluoroethylene". In: *Applied Physics Letters* 66.24 (1995), pp. 3281–3283. URL: https://doi.org/10.1063/1.113730.

[85] Sanghoon Park et al. "Energy harvesting efficiency of piezoelectric polymer film with graphene and metal electrodes". In: *Scientific Reports* 7.17290 (1 2017), pp. 2045–2322. URL: https://doi.org/10.1038/s41598-017-17791-3.

[86] Christian Peter and Herbert Kliem. "Feedback of the amorphous phase on the ferroelectric phase: Imprint effects in P(VDF-TrFE)". In: *IEEE 2nd International Conference on Dielectrics (ICD)*. Budapest: Hungary, 2018, pp. 1–4. DOI: 10.1109/ICD.2018.8514568.

[87] Christian Peter and Herbert Kliem. "Ferroelectric imprint and polarization in the amorphous phase in P(VDF-TrFE)". In: *Journal of Applied Physics* 125.17 (2019), p. 174107. URL: https://doi.org/10.1063/1.5091930.

[88] Christian Peter, Andreas Leschhorn, and Herbert Kliem. "Characteristic time dependence of imprint properties in P(VDF-TrFE)". In: *Journal of Applied Physics* 120.12 (2016), p. 124105. URL: https://doi.org/10.1063/1.4963356.

[89] Crine Jean Pierre. "A new analysis of the results of thermally stimulated measurements in polymers". In: *Journal of Applied Physics* 66.3 (1989), pp. 1308–1313. URL: https://doi.org/10.1063/1.344429.

[90] Andrzej Plonka. "Phenomenological interpretation of compensation law". In: *Journal of Molecular Structure* 479.2 (1999), pp. 177–182. ISSN: 0022-2860. URL: https://www.sciencedirect.com/science/article/pii/S0022286098008680.

[91] A. Anand Prabu et al. "Infrared spectroscopic studies on crystallization and Curie transition behavior of ultrathin films of P(VDF/TrFE) (72/28)". In: *Vibrational Spectroscopy* 41.1 (2006), pp. 1 –13. ISSN: 0924-2031. URL: http://www.sciencedirect.com/science/article/pii/S0924203105001463.

[92] T. Putzeys and M. Wübbenhorst. "Asymmetric polarization and hysteresis behaviour in ferroelectric P(VDF–TrFE) (76—24) copolymer thin films spatially resolved via LIMM". In: *Phys. Chem. Chem. Phys.* 17 (12 2015), pp. 7767–7774. DOI: 10.1039/C4CP06033D.

[93] T. Putzeys and M. Wübbenhorst. "Local polarization switching kinetics in thin-film P(VDF-TrFE) (76-24) studied by time-resolved LIMM". In: *IEEE Transactions on Dielectrics and Electrical Insulation* 25.3 (2018), pp. 835–839. ISSN: 1070-9878. DOI: 10.1109/TDEI.2018.007441.

[94] Nicholas M. Reynolds et al. "Spectroscopic analysis of the electric field induced structural changes in vinylidene fluoride/trifluoroethylene copolymers". In: *Macromolecules* 22.3 (1989), pp. 1092–1100. URL: http://dx.doi.org/10.1021/ma00193a016.

[95] Aurelien Roggero, Eric Dantras, and Colette Lacabanne. "Poling influence on the mechanical properties and molecular mobility of highly piezoelectric P(VDF-TrFE) copolymer". In: *Journal of Polymer Science Part B: Polymer Physics* 55.18 (2017), pp. 1414–1422. ISSN: 0887-6266.

[96] D. Rollik, S. Bauer, and R. Gerhard-Multhaupt. "Separate contributions to the pyroelectricity in poly(vinylidene fluoride) from the amorphous and crystalline phases, as well as from their interface". In: *Journal of Applied Physics* 85.6 (1999), pp. 3282–3288. URL: https://doi.org/10.1063/1.369672.

[97] John J. Rooney. "The extended Eyring kinetic equation and the compensation effect in catalysis". In: *Journal of Molecular Catalysis A: Chemical* 129.2 (1998), pp. 131–134. ISSN: 1381-1169. URL: https://www.sciencedirect.com/science/article/pii/S1381116997001945.

[98] M.T.A. Saif et al. "Effect of native Al2O3 on the elastic response of nanoscale Al films". In: *Acta Materialia* 50.11 (2002), pp. 2779 –2786. ISSN: 1359-6454. URL: http://www.sciencedirect.com/science/article/pii/S1359645402000897.

[99] C. B. Sawyer and C. H. Tower. "Rochelle Salt as a Dielectric". In: *Phys. Rev.* 35 (3 1930), pp. 269–273. URL: http://link.aps.org/doi/10.1103/PhysRev.35.269.

[100] D. Setiadi, P.P.L. Regtien, and P.M. Sarro. "Application of VDF/TrFE copolymer for pyroelectric image sensors". In: *Sensors and Actuators A: Physical* 42.1 (1994). Proceedings of Eurosensors VIII, pp. 585 –592. ISSN: 0924-4247. URL: http://www.sciencedirect.com/science/article/pii/0924424794800596.

[101] Pankaj Sharma et al. "Orientational imaging in polar polymers by piezoresponse force microscopy". In: *Journal of Applied Physics* 110.5 (2011), p. 052010. URL: https://doi.org/10.1063/1.3623765.

[102] Ari Sihvola. "Mixing Rules with Complex Dielectric Coefficients". In: *Subsurface Sensing Technologies and Applications* 1.4 (2000), pp. 393–415. ISSN: 1573-9317. URL: https://doi.org/10.1023/A:1026511515005.

[103] A. V. Sorokin, V. M. Fridkin, and Stephen Ducharme. "Pyroelectric study of polarization switching in Langmuir-Blodgett films of poly(vinylidene fluoride trifluoroethylene)". In: *Journal of Applied Physics* 98.4 (2005), p. 044107. URL: https://doi.org/10.1063/1.2006228.

[104] A. K. Tagantsev et al. "Identification of passive layer in ferroelectric thin films from their switching parameters". In: *Journal of Applied Physics* 78.4 (1995), pp. 2623–2630. URL: http://dx.doi.org/10.1063/1.360122.

[105] Alexander K. Tagantsev et al. "Nature of nonlinear imprint in ferroelectric films and long-term prediction of polarization loss in ferroelectric memories". In: *Journal of Applied Physics* 11 (2004), pp. 6616–6623. URL: http://scitation.aip.org/content/aip/journal/jap/96/11/10.1063/1.1805190.

[106] Yoshiro Tajitsu et al. "Investigation of Switching Characteristics of Vinylidene Fluoride/Trifluoroethylene Copolymers in Relation to Their Structures". In: *Japanese Journal of Applied Physics* 26.4R (1987), p. 554. URL: http://stacks.iop.org/1347-4065/26/i=4R/a=554.

[107] K. Tashiro et al. "Structural study on ferroelectric phase transition of vinylidene fluoride-trifluoroethylene copolymers (III) dependence of transitional behavior on VDF molar content". In: *Ferroelectrics* 57.1 (1984), pp. 297–326. URL: https://doi.org/10.1080/00150198408012770.

[108] Kohji Tashiro and Masamichi Kobayashi. "Structural phase transition in ferroelectric fluorine polymers: X-ray diffraction and infrared/Raman spectroscopic study". In: *Phase Transitions* 18.3-4 (1989), pp. 213–246. URL: http://dx.doi.org/10.1080/01411598908206864.

[109] G. Teyssèdre, A. Bernes, and C. Lacabanne. "DSC and TSC study of a VDF/TrFE copolymer". In: *Thermochimica Acta* 226 (1993), pp. 65 –75. ISSN: 0040-6031. URL: http://www.sciencedirect.com/science/article/pii/004060319380207Q.

[110] G. Teyssèdre, A. Bernes, and C. Lacabanne. "Temperature dependence of the pyroelectric coefficient in polyvinylidene fluoride". In: *Ferroelectrics* 160.1 (1994), pp. 67–80. URL: https://www.tandfonline.com/doi/abs/10.1080/00150199408007696.

[111] G. Teyssèdre, P. Demont, and C. Lacabanne. "Analysis of the experimental distribution of relaxation times around the liquid–glass transition of poly(vinylidene fluoride)". In: *Journal of Applied Physics* 79.12 (1996), pp. 9258–9267. URL: https://doi.org/10.1063/1.362601.

[112] G. Teyssèdre and C. Lacabanne. "Study of the thermal and dielectric behavior of P(VDF-TrFE) copolymers in relation with their electroactive properties". In: *Ferroelectrics* 171.1 (1995), pp. 125–144. URL: https://doi.org/10.1080/00150199508018427.

[113] G Teyssèdre et al. "Alpha-Relaxation/retardation mode in semicrystalline polymers with flexible chains". In: *Polymer* 35.20 (1994), pp. 4397 –4403. ISSN: 0032-3861. URL: http://www.sciencedirect.com/science/article/pii/0032386194900981.

[114] J. J. del Val, C. Lacabanne, and A. Hiltner. "A thermostimulated creep study of blends of poly(vinyl chloride) and chlorinated polyethylene". In: *Journal of Applied Physics* 63.11 (1988), pp. 5312–5319. URL: https://doi.org/10.1063/1.340395.

[115] J. Valasek. "Piezo-Electric and Allied Phenomena in Rochelle Salt". In: *Phys. Rev.* 17 (4 1921), pp. 475–481. URL: https://link.aps.org/doi/10.1103/PhysRev.17.475.

[116] Lian Wang et al. "Near-infrared transparent electrodes for precision Teng-Man electro-optic measurements: In 2 O 3 thin-film electrodes with tunable near-infrared transparency". In: *Applied Physics Letters* 87.16 (Oct. 2005), pp. 1–3. ISSN: 0003-6951. DOI: 10.1063/1.2089184.

[117] Wei Xia et al. "Epitaxy of Ferroelectric P(VDF-TrFE) Films via Removable PTFE Templates and Its Application in Semiconducting/Ferroelectric Blend Resistive Memory". In: *ACS Applied Materials & Interfaces* 9.13 (2017). PMID: 28290661, pp. 12130–12137. URL: http://dx.doi.org/10.1021/acsami.7b01571.

[118] Zhengguo Xiao et al. "Synthesis and Application of Ferroelectric P(VDF-TrFE) Nanoparticles in Organic Photovoltaic Devices for High Efficiency". In: *Advanced Energy Materials* 3.12 (2013), pp. 1581–1588. URL: https://onlinelibrary.wiley.com/doi/abs/10.1002/aenm.201300396.

[119] Y. Yagil and G. Deutscher. "Transmittance of thin metal films near the percolation threshold". In: *Thin Solid Films* 152.3 (1987), pp. 465 –471. ISSN: 0040-6090. URL: http://www.sciencedirect.com/science/article/pii/0040609087902628.

[120] Takeshi Yamada and Toyoki Kitayama. "Ferroelectric properties of vinylidene fluoride-trifluoroethylene copolymers". In: *Journal of Applied Physics* 52.11 (1981), pp. 6859–6863. URL: https://doi.org/10.1063/1.328679.

[121] Z. Ye et al. "Modeling of imprint in hysteresis loop of ferroelectric thin films with top and bottom interface layers". In: *Applied Physics Letters* 90.4 (2007), p. 042902. URL: https://doi.org/10.1063/1.2433026.

[122] Ying-Ju Yu and Alan J. H. McGaughey. "Energy barriers for dipole moment flipping in PVDF-related ferroelectric polymers". In: *The Journal of Chemical Physics* 144.1 (2016), p. 014901. URL: https://doi.org/10.1063/1.4939152.

[123] Xiuli Zhang, Haisheng Xu, and Yanni Zhang. "Temperature dependence of coercive field and fatigue in poly(vinylidene fluoride-trifluoroethylene) copolymer ultra-thin films". In: *Journal of Physics D: Applied Physics* 44.15 (2011), p. 155501. URL: https://doi.org/10.1088%2F0022-3727%2F44%2F15%2F155501.

[124] Xiuli Zhang et al. "Temperature dependence of imprint mechanism in poly(vinylidene fluoride-trifluoroethylene) copolymer ultrathin films". In: *Applied Physics Letters* 104.10, 103505 (2014), p. 103505. URL: http://scitation.aip.org/content/aip/journal/apl/104/10/10.1063/1.4868413.

[125] GuoDong Zhu et al. "Imprint effect in ferroelectric poly(vinylidene fluoride-trifluoroethylene) thin films". In: *Journal of Applied Physics* 106.7, 074113 (2009). URL: http://scitation.aip.org/content/aip/journal/jap/106/7/10.1063/1.3240200.